NASA TECHNICAL MEMORANDUM

NASA TM X-53462

APRIL 1, 1966

NASA TM X-53462

AERO-ASTRODYNAMICS RESEARCH REVIEW NO. 4

AERO-ASTRODYNAMICS LABORATORY

RESEARCH AND DEVELOPMENT OPERATIONS

GEORGE C. MARSHALL SPACE FLIGHT CENTER

HUNTSVILLE, ALABAMA

NASA-GEORGE C. MARSHALL SPACE FLIGHT CENTER

TECHNICAL MEMORANDUM X-53462

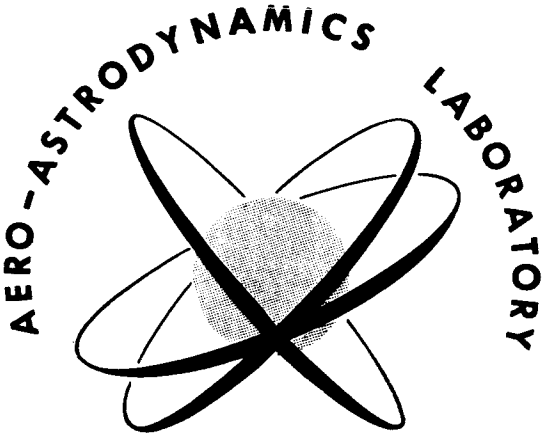

RESEARCH REVIEW NUMBER FOUR
July 1, 1965 - December 31, 1965

William D. Murphree - Editor

RESEARCH AND DEVELOPMENT OPERATIONS
AERO-ASTRODYNAMICS LABORATORY

April 1, 1966

PREFACE

The topics discussed in this fourth Aero-Astrodynamics Research Review cover a variety of subjects. Included are Fluid Mechanics, Aerothermodynamics, Structural Dynamics, Instrumentation, Selenography, Space Environment, and Orbit Theory and Prediction. It should be noted that no single review treats all subject areas being investigated by the Laboratory. Further, these reviews are not progress reports; rather it is attempted here to publish works of a research nature which have reached a milestone worthy of note. Other subjects will be discussed in forthcoming reviews.

It is hoped that these reviews will be interesting and helpful to other organizations engaged in space flight research and related efforts. Criticisms of this review and discussions concerning individual papers with respective authors are invited.

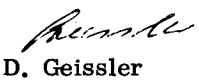

E. D. Geissler
Director, Aero-Astrodynamics Laboratory

CONTENTS. . .

Page

Page

VIII. PUBLICATIONS AND PRESENTATIONS

I. AEROTHERMODYNAMICS

CONVECTIVE HEAT TRANSFER IN TURBULENT, SUPERSONIC BASE FLOW

By

F. R. Krause, W. K. Dahm, R. E. Larson*, and A. R. Hanson*

SUMMARY

Turbulent, convective base heating has been studied in a Mach 3 wind tunnel utilizing a two-dimensional model with a blunt trailing edge. Measurements of heat transfer and base pressure, along with probings of total pressure, total temperature, mean and fluctuating velocities, and flow directions were performed inside the recirculation area behind the base. The results show that the base approaching recirculated flow establishes a "base boundary layer" which provides 86 percent of the heat flow resistance and therefore dominates convective base heating. Furthermore, the plumes between clustered rocket exhausts produce extremely high fluctuations through impingement shock and free shear layer interaction. These fluctuations are then convected or radiated backwards towards the vehicle subjecting the base boundary layer to turbulence levels exceeding 100 percent. These levels suggest that worse problems may be on the upper stages and that turbulence parameters may have to be considered when scaling base heating results to full scale conditions.

LIST OF SYMBOLS

Symbol	Definition
A	Amplitude parameter or ordinate intercept in King's law
a	Local sound speed
c_p	Specific heat
dA	Differential area
dV	Differential volume
$\bar{E}_b$	Mean hot-wire bridge voltage
e_b'	Fluctuating hot-wire bridge voltage
e_{RMS}	RMS of fluctuating voltage, $\overline{(e_b'^2)}^{1/2}$
E_b	Total hot-wire bridge voltage, $\bar{E}_b + e_b'$
f	Frequency
H	One-half model base height
H(f)	Transfer function
h	Heat transfer coefficient or probe face height
k	Thermal conductivity
M	Mach number, $\bar{U}/a$
p	Pressure
$\dot{Q}$	Total heat flow rate
$\dot{q}$	Heat flow rate per unit area
Re	Reynolds number
St	Stanton number, $h/c_p \rho \bar{U}$
S	Model length
T	Temperature
ΔT	Temperature difference; e.g., $\Delta T_{H.W.} = T_w - T_e$
t	Time
$\bar{U}$	Mean total velocity
U'	Fluctuating component of total velocity
U_{RMS}	RMS of fluctuating velocity, $U_{RMS} = \overline{(U'^2)}^{1/2}$
U	Total velocity, $U = \bar{U} + U' = (u^2 + v^2)^{1/2}$
$\bar{u}$, $\bar{v}$	Mean velocity components in x, y directions

* Litton Systems, Inc., Applied Science Division, St. Paul, Minnesota

LIST OF SYMBOLS (Concluded)

Symbol	Definition
u', v'	Fluctuating velocity components
u, v	Total velocity components, $u = \bar{u} + u'$, $v = \bar{v} + v'$
x, y, z	Coordinates
δ	Boundary layer or shear layer thickness
μ	Dynamic viscosity
ν	Kinematic viscosity
ρ	Density
σ	Spreading factor
ω	Specific weight

SUBSCRIPTS

A	Area-averaged value
B	Recirculation zone value
b	Base value (usually at center of base plate)
e	Equilibrium (recovery) temperature of hot-wire
H.W.	Hot-wire value
i	Uncorrected value
r	Recovery value
s	Wetted length, shoulder value
t	Tunnel total (stagnation) value
u	Upper frequency limit
w	Average hot-wire heated temperature or wall value
1	Outer edge of forebody boundary layer
2	Outer edge of free shear layer

I. INTRODUCTION

The bases of launch vehicles and reentry bodies are exposed to hot gases recirculated from the boundaries of adjacent burning or ablating flows. The attendant high base heating rates have been the cause of mission failures. Accordingly, during the last five years we have conducted some simple base heating experiments designed to afford direct insight into the convective transport processes.

The need for a simplified physical model of base heat transport was established in early attempts to scale the results from tests of small models to flight conditions. Today base heating predictions still utilize small scale tests since neither the high flow enthalpies nor the low pressures that cause recirculation through plume impingement shocks can be realized on a large scale.

Any analysis of convective transport in recirculation zones, such as base heating, requires a knowledge of the flow properties inside the recirculation region. Most published experimental results concentrate on the adjacent jet boundary areas instead of the base approach flow, since this is sufficient for the accepted base pressure theories in which the recirculation zone is replaced with a "dead air" region. Our experiments are an attempt to elucidate features of the flow within the recirculation region. The flow toward the base is compared with a two-dimensional stagnation point flow. In analysis of possible effects of the high turbulence levels, the Hiemenz-Sutera [1-3] solutions of the Navier-Stokes equations were used as a laminar reference.

Mean velocities, root-mean-square velocity fluctuations, total temperatures, base pressure distributions, and heating rates have been measured in the recirculation zone downstream of the blunt trailing edge of a two-dimensional model in a Mach 3 airstream (Fig. 1).

The measurements proved to be extremely difficult because of the low densities (0.01 of atmospheric) and high turbulence levels (in excess of 100 percent). Moreover, the geometry is different from that of actual engine clusters or reentry bodies. Therefore, the results cannot be used quantitatively. However, they do allow interesting qualitative conclusions about heat transfer characteristics of the base boundary layer and the occurrence of heat

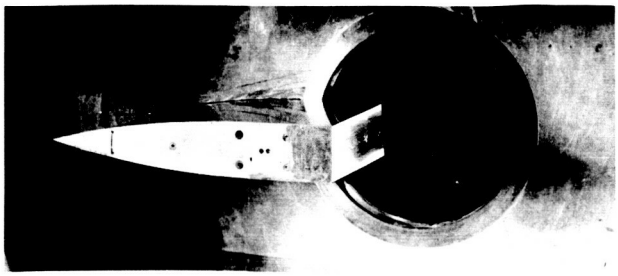

a) Model Installation in Wind Tunnel

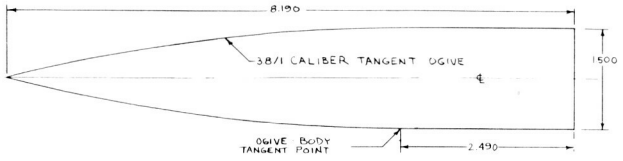

b) Forebody Side View

c) Schlieren Photograph of Flow Field

FIGURE 1. WIND TUNNEL MODEL AND FLOW FIELD

transfer effects arising from intense turbulence. In addition, the flow field is a special case of supersonic flow separation and reattachment, and our results might therefore be utilized in other fundamental studies of supersonic separation bubbles, flow over protuberances, wake flows, and cavity flows.

II. EXPERIMENTAL EQUIPMENT AND TECHNIQUES

A. TEST FACILITY

The two-dimensional base flow experiments were conducted at the University of Minnesota Aero-Hypersonic Laboratory in a continuous-flow wind tunnel [4, 5]. Air at room temperature (T_t = 509° R) can be delivered at a maximum continuous rate of 23.2 lb/sec at stagnation pressures up to 100 psig. The test channel in which the experiments were carried out consists of a 54-inch diameter stagnation chamber with provisions for flow straightening and reduction of turbulent velocity fluctuations. Mach 3 steel nozzle blocks produced uniform flow within a 6 × 9-inch test section.

B. WIND TUNNEL MODEL

Figure 1a shows the model installed in the wind tunnel. The model is two-dimensional, spans the test section, has a forward portion whose cross section is a tangent ogive, and has an 8.19-inch chord (Fig. 1b). Separate bases and afterbody components were used for the pressure, heat transfer, and probing runs. The base plates for all configurations have dimensions of 1.5 × 6 inches.

The base of the pressure model is a polished nickel plate, 0.018 inch thick, instrumented with eleven pressure taps and thirteen thermocouples (Fig. 2a).

The heat transfer base is made of pure nickel 0.018 inch thick. Copper-constantan thermocouples and pressure taps are imbedded in the base at selected locations. Figure 2b illustrates the complete instrumentation on the base. The base and coolant passages are housed in a micarta afterbody to isolate the base thermally from the model and improve the accuracy of the heat transfer data.

Although the micarta afterbody effectively isolates the base from the forebody, the possibility of conduction effects on the base itself had to be considered. Bench tests with a small replica of the base plate showed that slots 14 mils wide, filled with Armstrong cement, formed an effective barrier to conduction heat transfer. Following these tests, the thermocouples on the base plate were insulated by

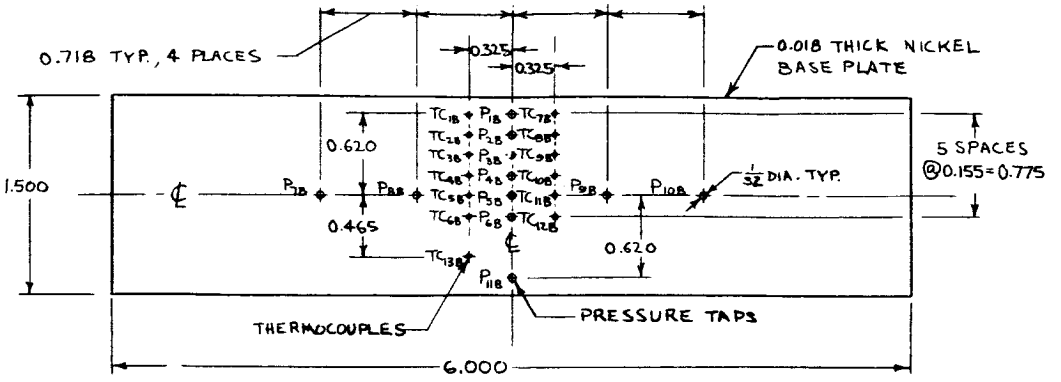

a) PRESSURE BASE PLATE

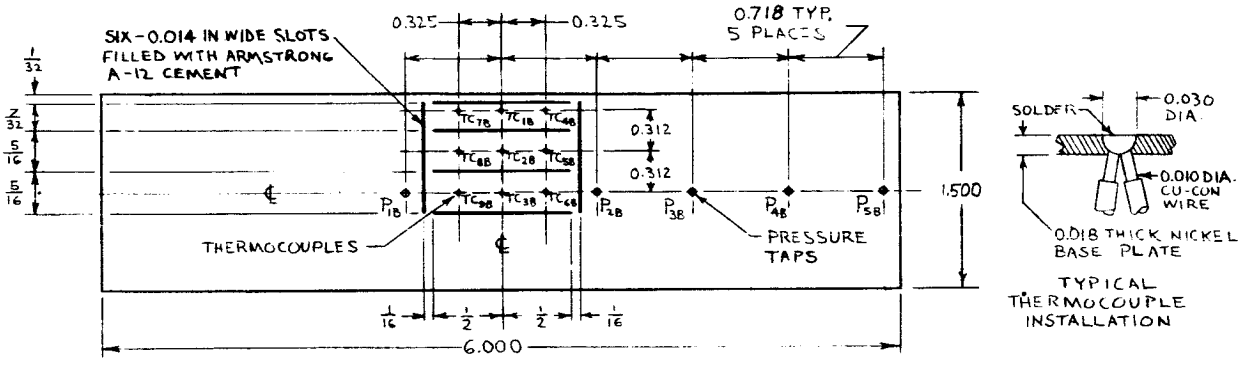

b) HEAT TRANSFER BASE PLATE

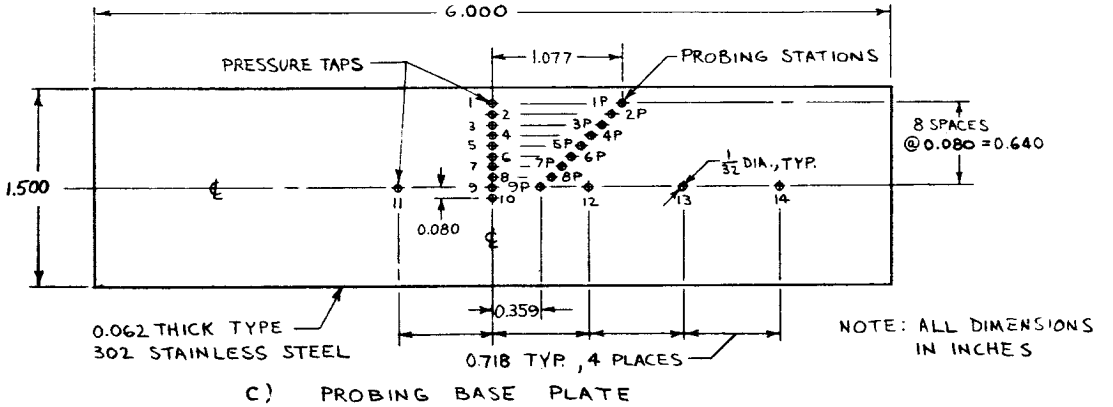

C) PROBING BASE PLATE

FIGURE 2. BASE PLATE CONFIGURATIONS

means of the cement-filled slots shown in the figure. The vertical slots were added to minimize horizontal transfer of heat across the base plate by conduction through the brass pressure-tap extensions.

The base of the probing model is of highly polished stainless steel, 0.062 inch thick (Fig. 2c). In addition to the nine probing openings there are fourteen static pressure taps. These consist of a vertical centerline array of ten taps, with four additional taps on the horizontal centerline. Included also are several thermocouples attached to the inner surface of the plate.

C. HEAT TRANSFER TECHNIQUE

The transient technique was used to obtain base heat transfer values. In this method the model is initially cooled below the equilibrium wall temperature to rise toward the equilibrium value.

Cooling lines were installed inside the model to bring the base down to 140°R at the start of a run. A shield was placed behind the model to retard aerodynamic heating until proper flow had been established in the tunnel.

If heat conduction through the model skin and radiation effects are neglected, the rate at which heat is transferred from the boundary layer at any point on the model surface may be equated to the rate at which heat is stored at the same location, or

$$\dot{q}\, dA = \omega\, c_p\, dV\, \frac{\partial T_b}{\partial t} \qquad (1)$$

where the notation is the following:

$\dot{q}$ = Rate of heat flow (Btu/ft^2 hr)

dA = Differential area element of base (ft^2)

ω = Specific weight of base material (lb/ft^3)

c_p = Specific heat of base material (Btu/lb°F)

dV = Differential volume element of base material (ft^3)

T_b = Base temperature (°R).

The Newtonian heat flow equation

$$\dot{q} = h(T_r - T_b) \qquad (2)$$

combined with Equation (1) gives

$$h = \frac{\omega\, c_p \frac{dV}{dA} \frac{\partial T_b}{\partial t}}{T_r - T_b} \,. \qquad (3)$$

The heat transfer coefficient h can then be obtained by measuring the instantaneous wall temperature and its rate of change. The wall recovery temperature T_r can either be calculated or measured as a function of the tunnel total temperature.

D. HOT-WIRE EQUIPMENT

Probe calibrations and mean velocity measurements in the base recirculation zone were initially performed with a constant-temperature hot-wire anemometer [6] which was manually balanced.

Fluctuating velocities were measured with a DISA type 55A01 constant-temperature anemometer without linearizer. A simplified circuit diagram of this anemometer and associated apparatus is shown in Figure 3a.

The sensing elements were made either of 0.00025-inch diameter platinum-iridium (80 Pt. 20Ir) or of platinum plated tungsten wire with a 0.0002-inch diameter (Fig. 3b). They were always aligned in the spanwise flow direction; that is, parallel to the z axis.

The use of hot-wire anemometry proved to be difficult because of the low density (0.01 of atmospheric) and the very high turbulence levels ($\approx$ 100 percent). For our flow conditions the calibration results are believed to be representative of what can be obtained with commercial constant-temperature hot-wire sets at the present time.

The presence of a wall increases the heat loss from the wire through conductive and other transport phenomena. Close to the wall the corrections are very large, as the heat loss to the wall overpowers the convective loss to the air. Furthermore, the usual procedure of measuring the wall effect in still air as the difference between the readings, $[E_b(x)]^2$ (close to the wall) and $[E_b(x \to \infty)]^2$ (far from the wall), yielded inconsistent results. Therefore, we estimated the wall effect from the difference between the indicated mean velocity profile and an extrapolated mean velocity profile. Figure 4 illustrates the procedure and shows typical results. The following adjustment

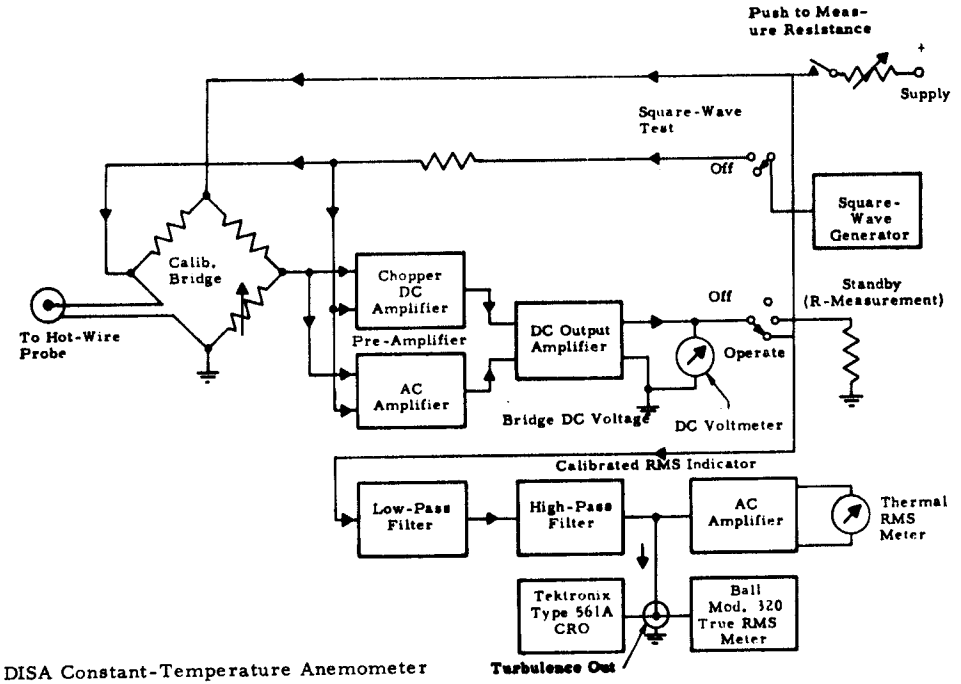

a) DISA Constant-Temperature Anemometer and Accessory Equipment

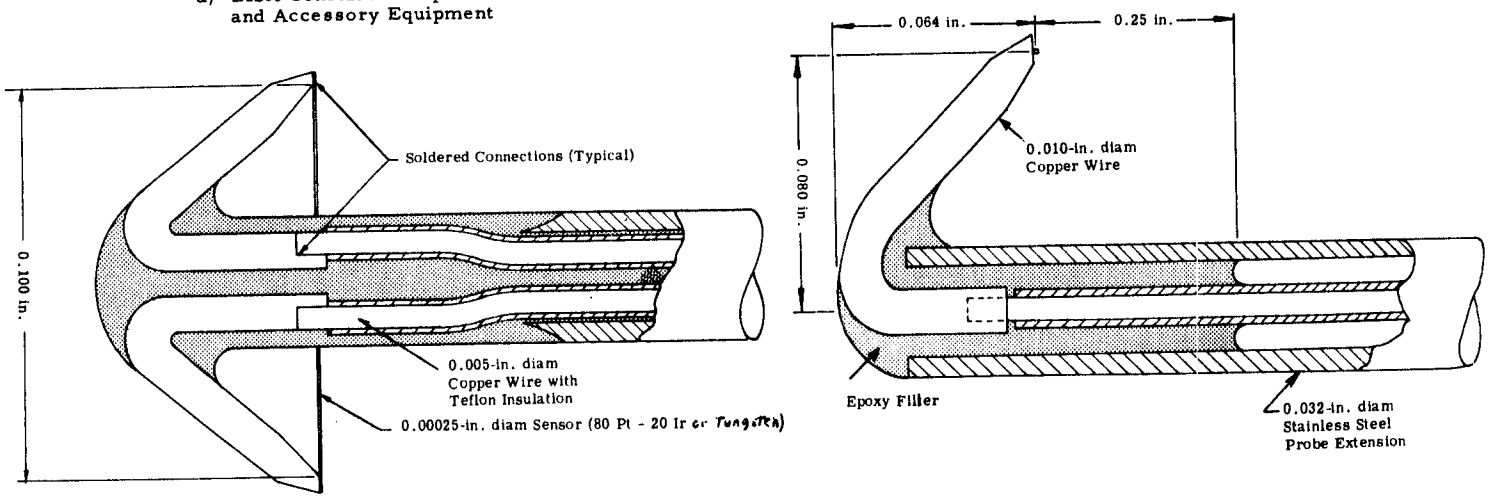

(Top View) b) Hot-Wire Probe (Side View)

FIGURE 3. HOT-WIRE CIRCUIT AND PROBE

(parallel shift) was used for all static hot-wire calibration curves:

$$\Delta A = [\bar{E}_b(x)]^2 - [\bar{E}_b(x \to \infty)]^2$$

$$= 1.3 \times 10^{-4} \ (V^2\text{-in.})/x \ (\text{in.}) \qquad (4)$$

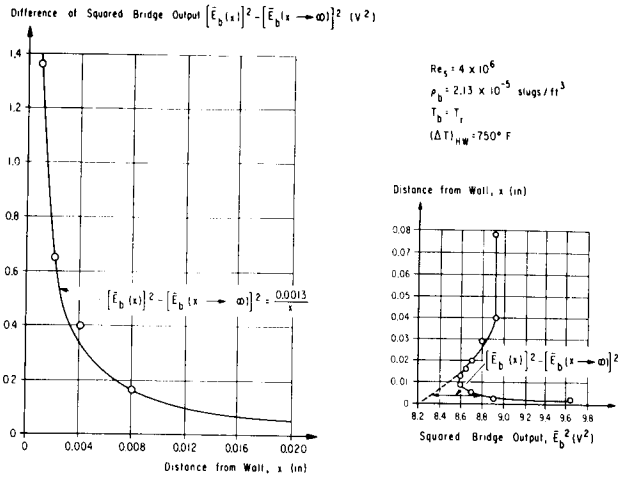

FIGURE 4. WALL EFFECT CORRECTION PROCEDURE

The wall effect correction was applied at all probing stations; it was also used to correct the RMS fluctuation readings, even though the wall effect had been obtained from mean values.

The low density in our tests not only produced an unusually large wall effect, but it also limited the frequency response severely. This was revealed by dynamic calibration tests. The hot-wire was placed in the smooth flow of a calibration duct and excited by a square or sine wave of heating current to simulate fluctuating velocity effects in the anemometer circuit. The hot-wire voltage transfer function was obtained over a frequency range utilizing the circuit and equations described by Janssen, et al [7] and Fingerson [8] for the sine wave method. The circuit and equation employed are shown in Figure 5b (See following page). The voltage transfer function was measured over a range of densities, mean velocities, and wire overheats. The best estimate for the reference density of $\rho_b \approx 0.01$ atmospheric and zero velocity is given in Figure 5a, which shows the sine and square wave results for a platinum-iridium probe. Included also are square wave and estimate sine wave responses for a tungsten probe. Additional sine wave measurements for tungsten probes are now in progress.

A detailed square wave response over a density range of zero velocity for a tungsten probe is shown in Figure 6a, and Figure 6b describes the measurement procedure.

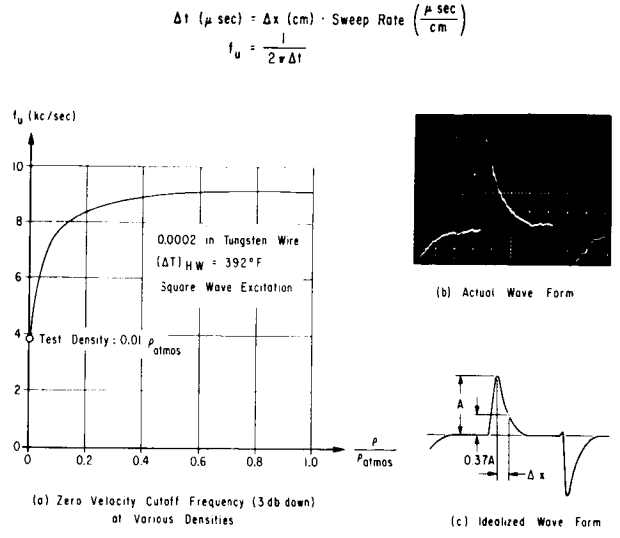

FIGURE 6. SQUARE WAVE TEST

Tests performed over a wide velocity range (up to 800 ft/sec) show little improvement in frequency response at our low test density. This is in contrast to the marked improvement obtained at ambient densities.

The differences (up to 100 percent) between the sine and square wave tests indicate that the measured power transfer function may be correct in order of magnitude only. Further comparisons of these two methods are required. However, it indicates clearly that the range of usable frequencies extends only to approximately 4 kc/sec, whereas the wind tunnel test data show fluctuations above 30 kc/sec. This indicates that caution must be shown in interpreting low-density hot-wire measurements of velocity fluctuations containing frequencies beyond 4 kc/sec.

III. BASE APPROACH FLOW

The base approach flow has been studied with and without base cooling over a range of forebody

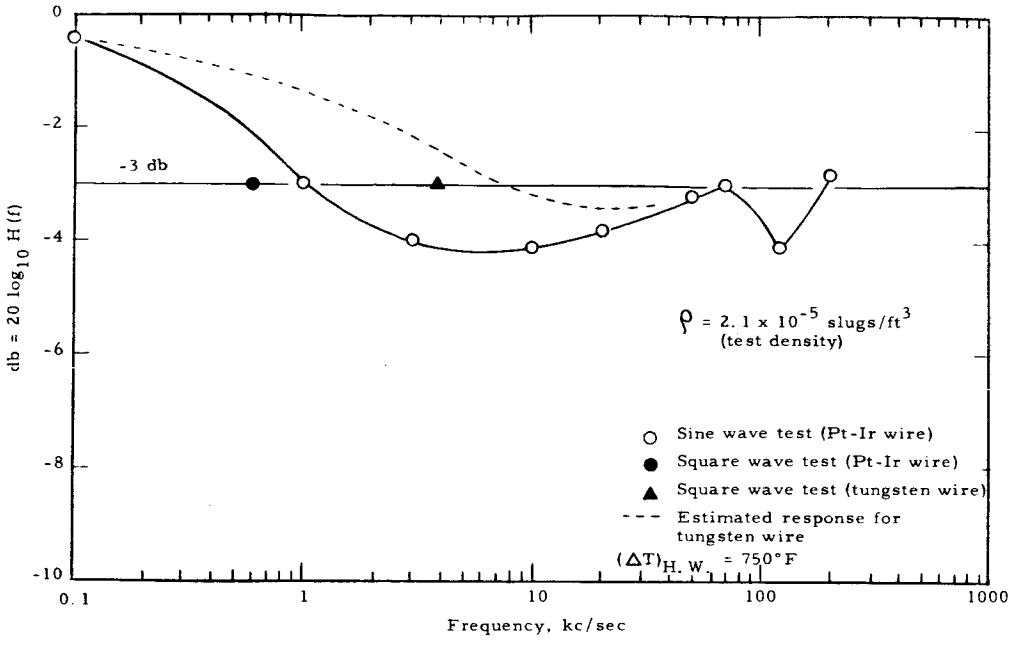

a) Frequency Response

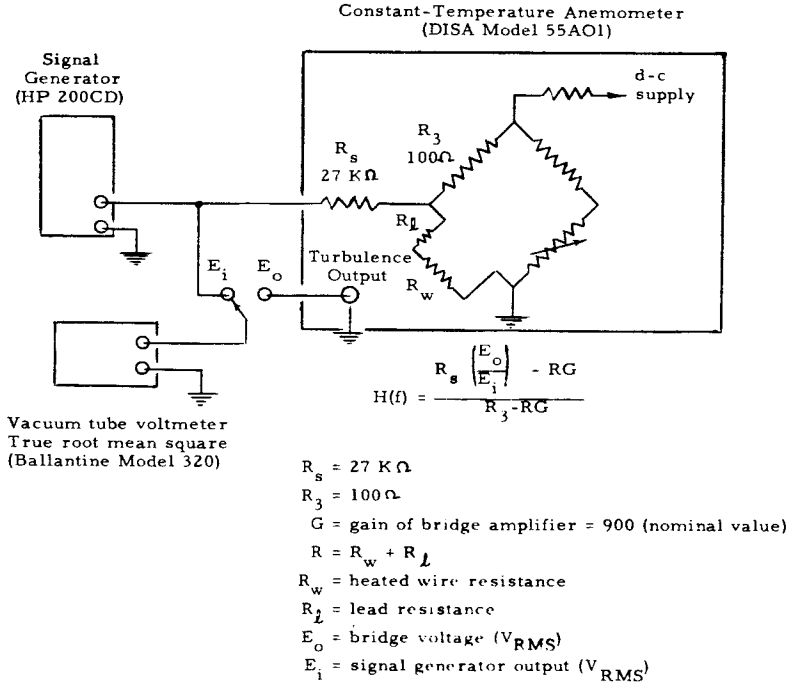

b) Sine Wave Circuit Diagram

FIGURE 5. HOT-WIRE FREQUENCY RESPONSE FROM SINE WAVE METHOD

Reynolds numbers. Hot-wire, pressure, and temperature measurements were performed at various locations in the shear layers and recirculation zone. The location of these various probings are shown in Figure 7. The early measurements were performed by insertion of probes either through the wake throat or across the shear layers. However, this method disturbs the flow field; therefore, later measurements were performed by insertion from the base plate. Some probings extended deep into the jet shear layers and the "subsonic hole" between the plume impingement shocks. All hot-wire traverses have been restricted to our reference "test conditions"; that is, to the uncooled base at $Re_s = 4 \times 10^6$.

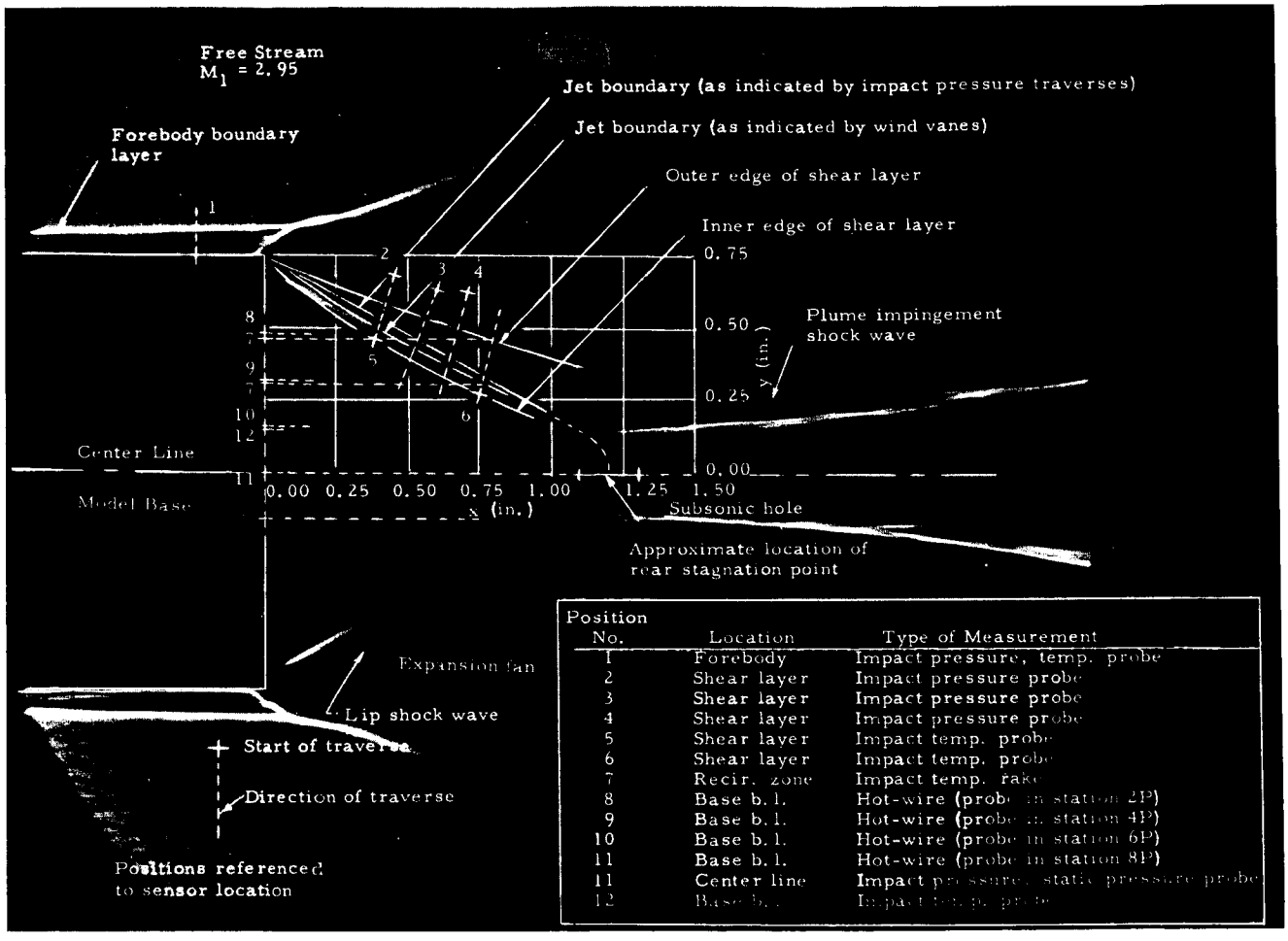

Position No.	Location	Type of Measurement
1	Forebody	Impact pressure, temp. probe
2	Shear layer	Impact pressure probe
3	Shear layer	Impact pressure probe
4	Shear layer	Impact pressure probe
5	Shear layer	Impact temp. probe
6	Shear layer	Impact temp. probe
7	Recir. zone	Impact temp. rake
8	Base b. l.	Hot-wire (probe in station 2P)
9	Base b. l.	Hot-wire (probe in station 4P)
10	Base b. l.	Hot-wire (probe in station 6P)
11	Base b. l.	Hot-wire (probe in station 8P)
11	Center line	Impact pressure, static pressure probe
12	Base b. l.	Impact temp. probe

FIGURE 7. LOCATIONS OF PROBING MEASUREMENTS

A. HOT-WIRE MEASUREMENTS

Mean velocities and RMS velocity fluctuations along the centerline are shown in Figure 8. Contrary to a two-dimensional stagnation point flow, the mean velocities are not constant outside the boundary layer but show a broad maximum at about 0.35 in. from the base plate. The RMS velocities are comparable to the mean velocities; thus, we have an extremely high local turbulence level, which makes the hot-wire measurements questionable. However, the absolute magnitude of the velocity fluctuations along the centerline are still considerably smaller than the velocity fluctuations in the free shear layers, which are estimated at 20 percent of the free stream velocity, or 420 ft/sec.

Oscilloscope traces of typical hot-wire output voltages e_b' are shown in Figure 9, where narrow band components are evident. The amplitudes of the peaks are of the same order as the mean bridge voltages, indicating the possibility of flow reversal or negative velocity across the hot-wire, although

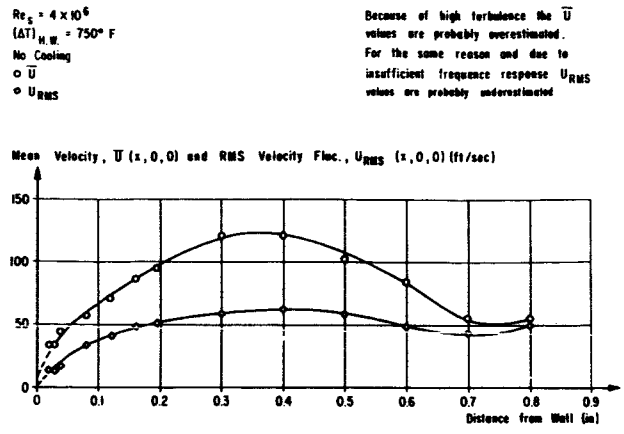

FIGURE 8. VELOCITY VARIATION ALONG CENTER LINE

the anemometer cannot discriminate between velocity directions. Consequently, all mean velocities are probably overestimated while RMS velocities are underestimated, even if one would correct for frequency response.

In spite of these difficulties, we attempted a spectral analysis of the hot-wire output fluctuations e_b' to obtain a confirmation of the narrow band components shown by the oscilloscope traces. To obtain longer records of the fluctuations and allow accurate calculations of power spectra, a traverse through the approach flow region and base boundary layer was recorded on a Hewlett-Packard/Sanborn Model 3900 magnetic tape data recording system. The data were analyzed with a third octave filter and yielded the power spectra shown in Figure 10. An approximate correction of the amplitudes for the limited frequency response was performed utilizing Figure 5a. The power spectrum reveals five distinct peaks at f = 0.2, 0.4, 1, 6, and 30 kc/sec. The higher frequency peaks do not normally occur in low velocity recirculation areas. We surmise, therefore, that they reflect acoustic transport of high frequency phenomena from the adjacent high speed points.

Although somewhat speculative, there appear to be two possible sound radiation phenomena which could account for the narrow band frequencies observed. The first is connected with reverberating waves. Subsonic velocities have been indicated by pressure probings, interferometer evaluations, and wind vanes between the roots of the two plume impingement shocks. The associated region of subsonic flow extends downstream of the stagnation point that terminates the dividing streamlines and provides a "subsonic hole." Sound may be radiated backwards through this hole toward the base. These sound waves will then be reflected at the base and might support waves reverberating between the base and the "subsonic hole." The occurrence of standing acoustic waves would then lead to isolated peaks of the pressure power spectrum which should be centered approximately at the resonant frequencies of the corresponding "open pipe,"

$$f_n \approx \frac{a_b}{4L} (2n + 1) \qquad (5)$$

where n = 0, 1, 2 . . . denotes the fundamental and higher harmonic frequencies, L is the distance between the base and downstream stagnation point, and a_b is the speed of sound in the base region. Substituting the experimental values

$L = 1.3$ in.

$a_b = 1070$ ft/sec

we obtain

$f_0 = 2.5$ kc/sec

$f_1 = 7.4$ kc/sec.

The second harmonic f_1 is fairly close to the middle peak which was observed at 6 kc/sec. This frequency was found throughout the recirculation zone, which also substantiates the speculation of standing sound waves.

The second type of sound radiation would originate in the free shear layer. For example, Ffowcs-Williams and Maidanik's description of Mach wave sound emission [9] might indicate a mechanism by which the high frequency fluctuations of the free shear layer could propagate into the recirculation zone. In free shear layers a broad maximum in the power spectrum is centered around a Strouhal number of 0.2. This would lead to a frequency of

$$f \approx 0.2 \frac{\bar{U}_2}{\delta_2} \qquad (6)$$

where $\bar{U}_2$ is the velocity at the outer edge of the free shear layer and δ_2 is the average geometrical shear layer thickness. Substituting the measured free stream velocity, $\bar{U}_2 = 2100$ ft/sec, and the streamwise average of the geometrical jet shear layer thickness, $\delta_2 = 0.2$ in., one obtains $f \approx 25$ kc/sec. This agrees roughly with the highest observed peak in the spectrum of f = 30 kc/sec.

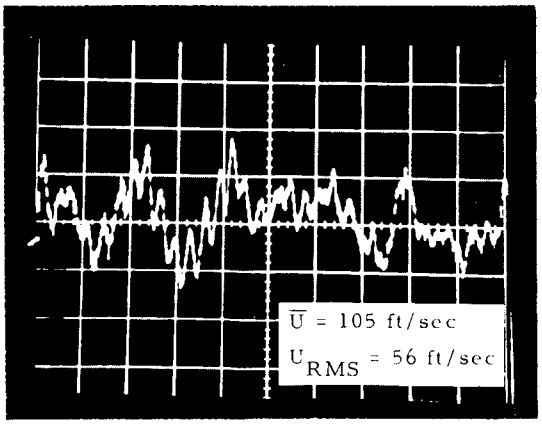

a) x = 0.155 in.

$Re_s = 4 \times 10^6$
$T_b = T_r$
$(\Delta T)_{H.W} = 750°F$

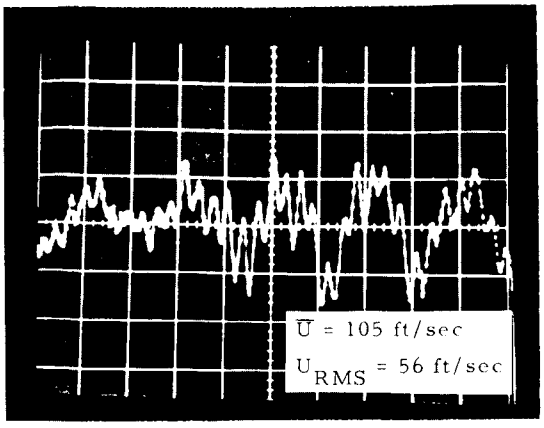

b) x = 0.078 in. Probing Base Plate at Position 9. See Figure 2c and Figure 7.

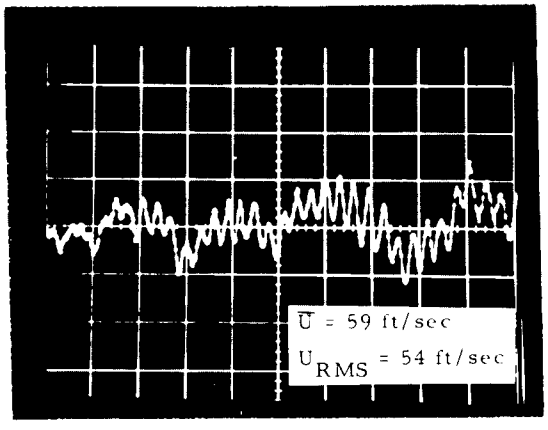

c) x = 0.019 in.

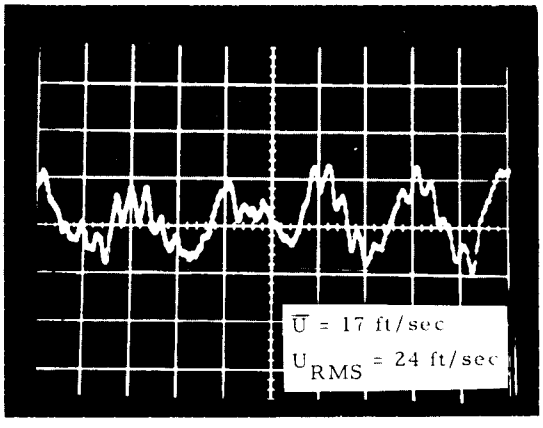

d) x = 0.004 in.

Vertical Sensitivity, 0.05 V/cm
Sweep Speed, 5×10^{-4} sec/cm

FIGURE 9. OSCILLOSCOPE DISPLAYS OF NARROW BAND VELOCITY FLUCTUATIONS

If these speculations are borne out by future experiments, we may have serious noise problems on the upper stages, partially produced by plume impingement effects (subsonic hole) such that they can not be studied by full-scale static firings or single jet experiments.

The low-frequency peaks cannot be explained by the sound radiation sources just discussed. Other simple or plausible explanations, such as the recirculation of a "frozen" flow pattern, were not fruitful.

B. TOTAL TEMPERATURE MEASUREMENTS

The total temperature in the approach flow was measured with a thermocouple rake inserted from the tunnel side wall. The wires were aligned in the spanwise direction (z) to minimize conduction errors.

The total temperature distribution in the approach flow was measured for several base cooling rates, and shown in Figure 11. Even for large amounts of cooling the base thermal boundary layer thickness is less

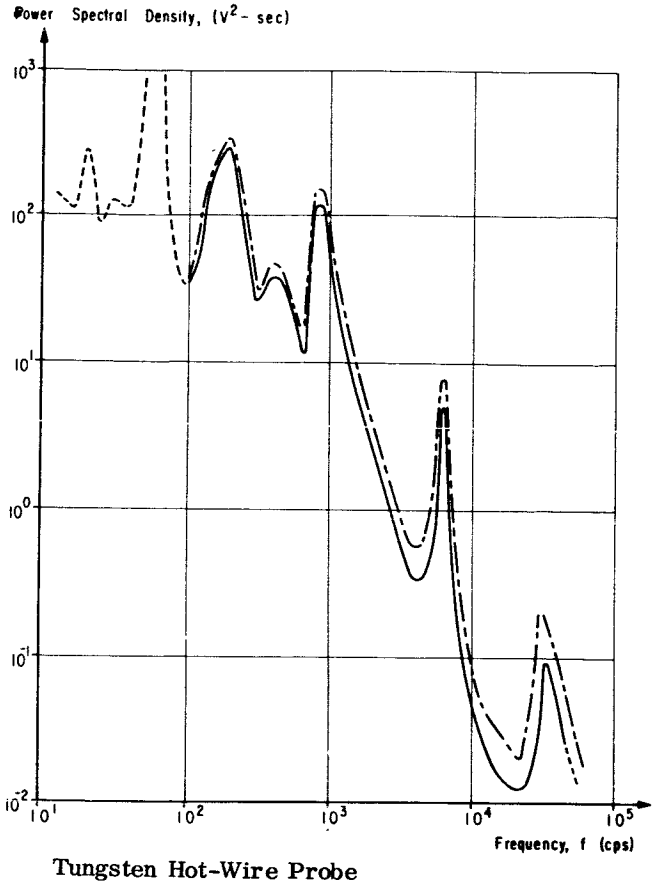

Tungsten Hot-Wire Probe

$(\Delta T)_{H.W.} = 392°F$

$Re_s = 4 \times 10^6$

x = 0.0194 in.

_____ Uncorrected

- —— - Corrected for frequency response (Fig. 5)

------ Data affected by filter settings of anemometer and tape recorder response

FIGURE 10. VARIATION OF POWER SPECTRAL DENSITY WITH FREQUENCY

than 0.10 in. In spite of this, the approach flow senses the depression in base temperature to some extent, resulting in the creation of an approach flow which has a constant temperature below the free stream recovery value ($\approx 0.90\ T_t$). This is due partially to the recirculating flow motion which transfers cool fluid particles from the immediate vicinity of the base plate to other portions of the recirculation zone. We have, thus, the unusual situation that the effects of wall temperature are felt outside the thermal boundary layer. This is not a heat conduction effect, since the temperature gradients are zero outside the base boundary layer. Rather, it must result from a turbulent convection process that mixes the "cooled" particles homogeneously within the recirculation zone, thereby creating a region of constant total temperature.

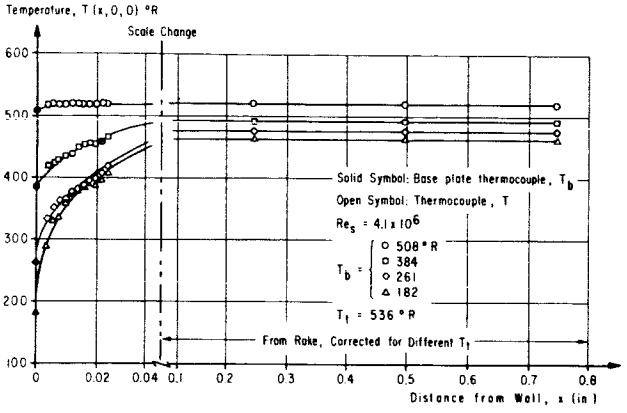

FIGURE 11. TEMPERATURE IN APPROACH FLOW AND BASE BOUNDARY LAYER

To show the interdependence of base plate temperature T_b and recirculation temperature $T_B = T_B(x,y,z)$ more clearly, the latter has been replotted as a function of the base temperature (cooling rate). Three curves are shown in Figure 12, with position as a parameter. The data which average out to the upper curve were measured throughout the recirculation zone. The fact that they fall on one curve demonstrates once again that the total temperature is constant throughout the base approach flow. The second curve shows a location close to the wall and here the scatter of the points is probably caused by a slight misalignment of the total temperature rake. The point of intersection at the three curves indicates the recirculation zone and base recovery temperature, which is approximately 95 percent of the free stream stagnation temperature T_t.

The coupling between the base temperature and the "remote" approach flow is one effect which cannot be treated by a stagnation point analysis where the upstream conditions are unaffected by wall cooling. Furthermore, the "base boundary layer" is affected at the shoulders, since the cooled particles must be turned back to be recirculated. However, the hot-wire and total temperature traverses show that both a velocity and a thermal boundary layer exist at all probing stations.

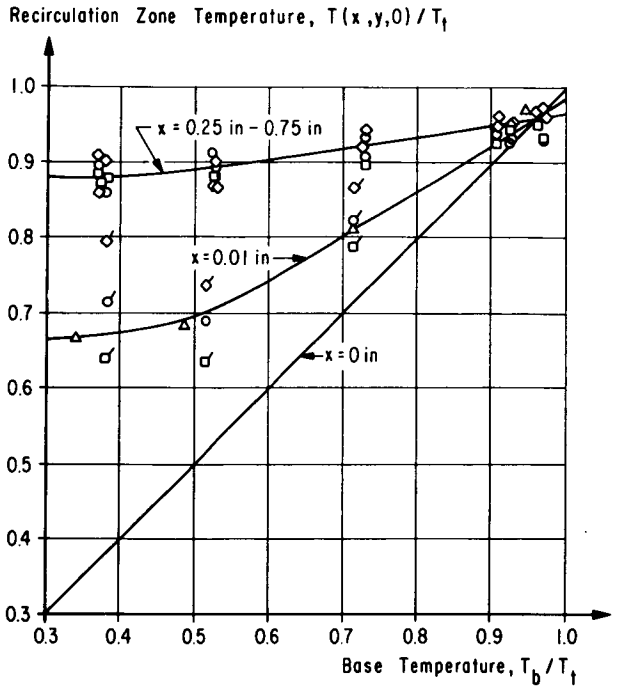

$Re_s = 4.5 \times 10^6$

$M_1 = 2.95$

$T_t = 500°R$

Rake Measurements

x = 0.01 in.	x = 0.25 in. - 0.75 in.
○	y = 0.465 in.
□	y = 0.310 in.
◇	y = -0.155 in.

△ Temperature probe

FIGURE 12. TEMPERATURE DISTRIBUTION IN APPROACH FLOW

IV. THE BASE BOUNDARY LAYER

A. VELOCITY BOUNDARY LAYER

The measured wall pressures are summarized in Figure 13. The existence of a stagnation point is shown by the pressure maximum around the centerline. However, the pressure also varies in the horizontal z direction. Accordingly, we observe deviations from a two-dimensional behavior. The decrease of the wall pressures along the two-dimensional "stagnation point line" y = 0, x = 0 indicates that the deceleration of the base approach flow resembles that of an axisymmetric flow instead of a two-dimensional flow. The following discussion of the pressure measurements is limited to the plane of symmetry z = 0.

Falkner and Skan [10] have shown that in boundary layer theory, the existence of an outer "potential" flow, which follows from the wall pressures, can be extended to stagnation point flows if one compares the calculated velocities with the tangential velocity component. The wedge solutions of Falkner and Skan for stagnation flow coincide with Hiemenz' exact solution of the Navier-Stokes equations. In laminar stagnation point flows, the wall pressure distributions can thus be used to calculate the tangential velocity components at the outer edge of the base boundary layer. This has been done assuming the following:

a) The stagnation pressure along the edge is constant and equal to the wall pressure at y = 0.

b) The Bernoulli equation may be used along the outer edge in spite of the high local turbulence levels.

Within these assumptions the mean tangential (vertical) velocity component at the outer edge follows from

$$\bar{v}(0,y,0) = \frac{2}{\rho_b(0,0,0)} [p(0,0,0) - p(0,y,0)]^{\frac{1}{2}} \quad (7)$$

The results of this calculation over a Reynolds number range are shown in Figure 14. For Reynolds numbers of 2.78×10^6 and larger a linear velocity variation exists up to y = 0.3 in. This is slightly below position number 9 (probing station 4P) shown in Figure 7. The scatter at the lower Reynolds numbers is attributed to pressure measuring errors and transitional flow conditions.

The consistent trend of increase in the stagnation-point velocity gradient with Reynolds number is also shown in Figure 14. A comparison can be made between these data and values obtained from centerline hot-wire probings, utilizing the continuity equation. From Figure 8, at $Re_s = 4 \times 10^6$ the centerline velocity gradient $\partial\bar{U}/\partial x$ is approximately equal to 6×10^3 sec $^{-1}$, which compares with 7.4×10^3 sec $^{-1}$ shown in Figure 14.

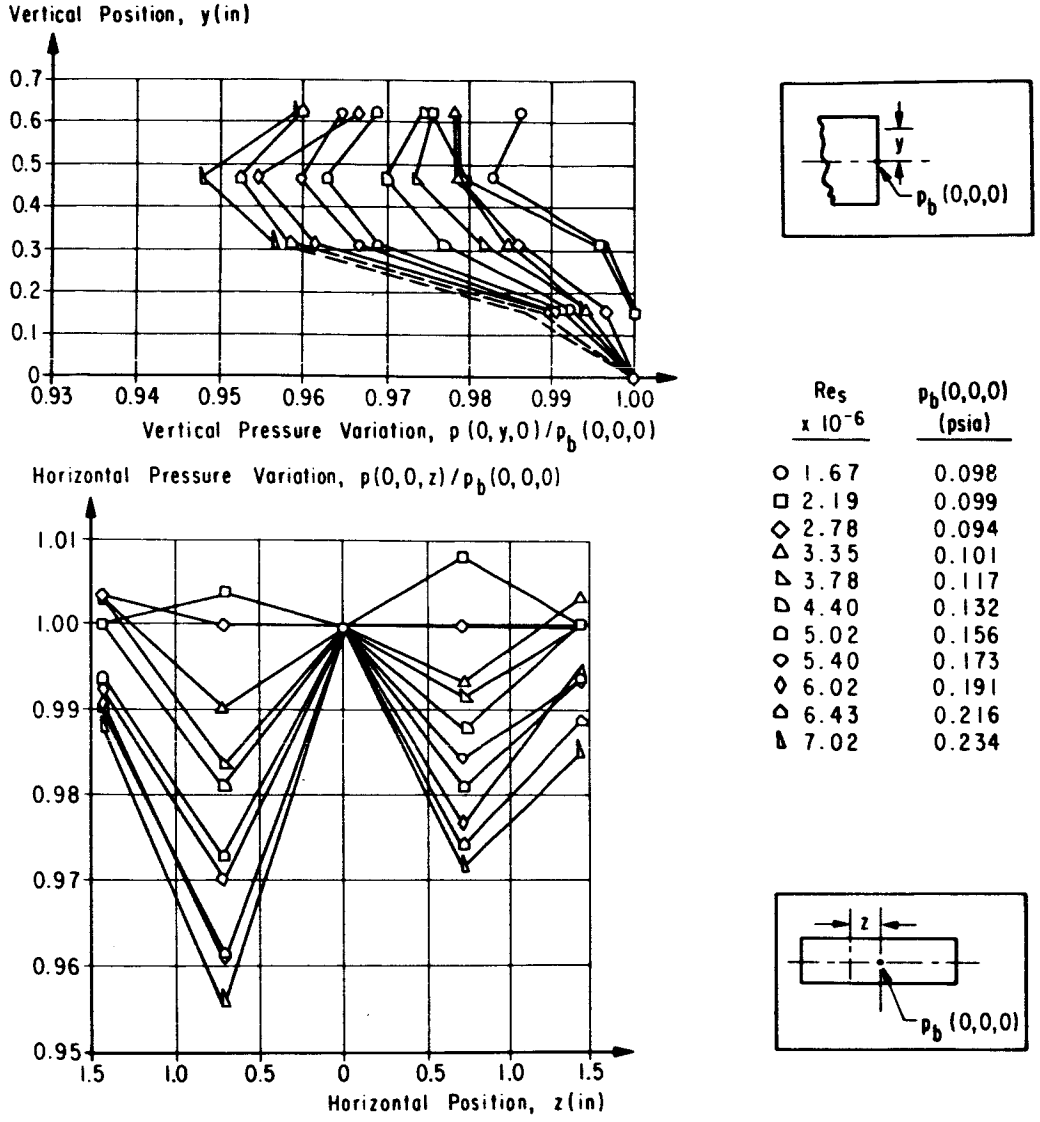

FIGURE 13. BASE PLATE PRESSURE DISTRIBUTION

$\partial\bar{U}/\partial x$ is approximately equal to 6×10^3 sec $^{-1}$, which compares with 7.4×10^3 sec^{-1} shown in Figure 14.

Comparing the "outer edge" velocities determined from the wall pressure distribution with mean velocities measured by the hot-wire, one apparently finds little agreement. However, if one interprets the non-zero value at y = 0 as resulting from the axial velocity component $\bar{u}$, reasonable agreement exists up to y = 0.160 in. Consequently, the usual boundary layer assumptions seem approximately justified up to this position. The strong disagreement at higher stations cannot be presently explained. However, because of the extremely high local turbulence levels on the base approach flow, one might expect the base boundary layer to exhibit some new or unexpected characteristics.

Some qualitative features of the adjustment of this boundary layer to the high turbulence levees of the base approach flow can be inferred from hot-wire traverses. RMS velocity profiles are shown in Figure 15. The absolute values show the usual "hump" attributed to turbulence amplification near a solid wall. Sternberg [11] has analyzed this amplification in terms of "image" vortices which replace the wall in potential flow theory; whereas Sutera, et al. [2,3], have studied the growth of vorticity which attends the selective stretching of vortex lines in a two-dimensional stagnation point flow. This vortex stretching hypothesis is supported by the measure-

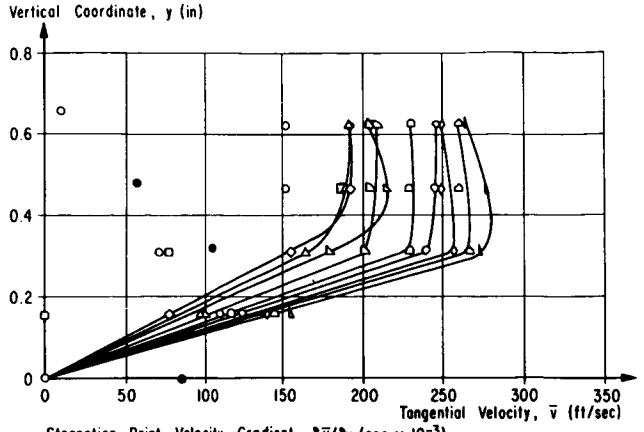

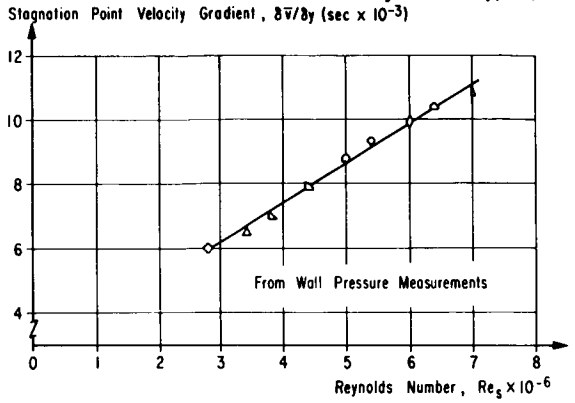

○ = Wall Pressure Measurements

● = $Re_s = 4 \times 10^6$ Hot-Wire Measurements

$Re_s \times 10^{-6}$	
○ 1.67	◇ 5.02
□ 2.19	⌂ 5.40
◇ 2.78	◊ 6.02
△ 3.35	⌂ 6.43
◺ 3.78	◺ 7.02
⌂ 4.40	No Cooling

FIGURE 14. BASE PLATE TANGENTIAL VELOCITY COMPONENT AND STAGNATION POINT VELOCITY GRADIENT

ments of Kuethe, et al. [12], in the stagnation region of a sphere, and also by traverses of the flat plate boundary layer (Townsend [13] and Sternberg [11]). However, the turbulence levels in the base boundary layer are much higher. In flat plate boundary layers they reach about 60 percent, whereas our measured values go up to 200 percent. The actual levels are probably even higher owing to insufficient frequency response and the hot-wire's inability to distinguish flow direction.

We have tried to assess the possible effects of turbulence by comparing hot-wire and total temperature traverses with the laminar stagnation point solutions [1-3]. These solutions depend on an empirical parameter, the velocity gradient $\partial\bar{u}/\partial y$ at the outer edge of the stagnation point boundary layer. This gradient was obtained from the wall pressure measurements as shown in Figure 13. A strong Reynolds number dependence is evident, leading to the suspicion that it is also dependent on the turbulence level.

The chosen velocity gradients therefore reflect the turbulence of the actual flow such that the laminar stagnation point solutions are automatically adjusted to give the full turbulent shear stress.

The "adjusted" laminar mean velocity profiles were calculated for these traverses where the measured streamwise gradient of the outer edge velocity remains approximately constant (Fig. 14). Figure 16 shows a comparison between these calculated mean velocity profiles and hot-wire results. Included at positions 9 and 10 (see Figure 7, probing stations 4P and 6P) are calculations based on Sutera's solution for various values of the amplification parameter A. The agreement is rather poor.

One may tentatively conclude, therefore, that turbulence can appreciably change the shape of the non-dimensional mean velocity profiles.

B. THERMAL BOUNDARY LAYER

Total temperatures were measured with a miniature thermocouple probe (0.004-in. face height). The results are shown in Figure 17, which includes the adjusted two-dimensional stagnation point solutions from the theory of Livingood and Donoughe [14].

The theoretical profiles assume laminar flow and apply the same empirical velocity gradient already used in the calculations for Figure 16. The wall gradients are less than the measured profiles, indicating that the high turbulence level changes the shape of the non-dimensional temperature profile. The dashed curves were obtained from measured heat transfer values, showing good agreement with the experimental points. The temperature gradients at the wall are higher than those predicted by the "adjusted" laminar stagnation-point analysis, even though the full velocity gradient (and shear stress) of the turbulent flow was taken into account.

The theoretical and experimental temperature gradients are replotted in Figure 18 as a function of the temperature difference between the base approach flow and the base. Both gradients increase faster than linearly with this temperature difference; however, the measured gradients exceed the estimated ones by a factor of 2. The same is true for the heat transfer rates which are shown in the lower part of Figure 18. They were obtained from the temperature gradients by multiplication with the thermal conductivity k of air. The difference in shape of the heat transfer and temperature gradient curves is caused by the temperature dependence of k which was evaluated at the base plate temperature.

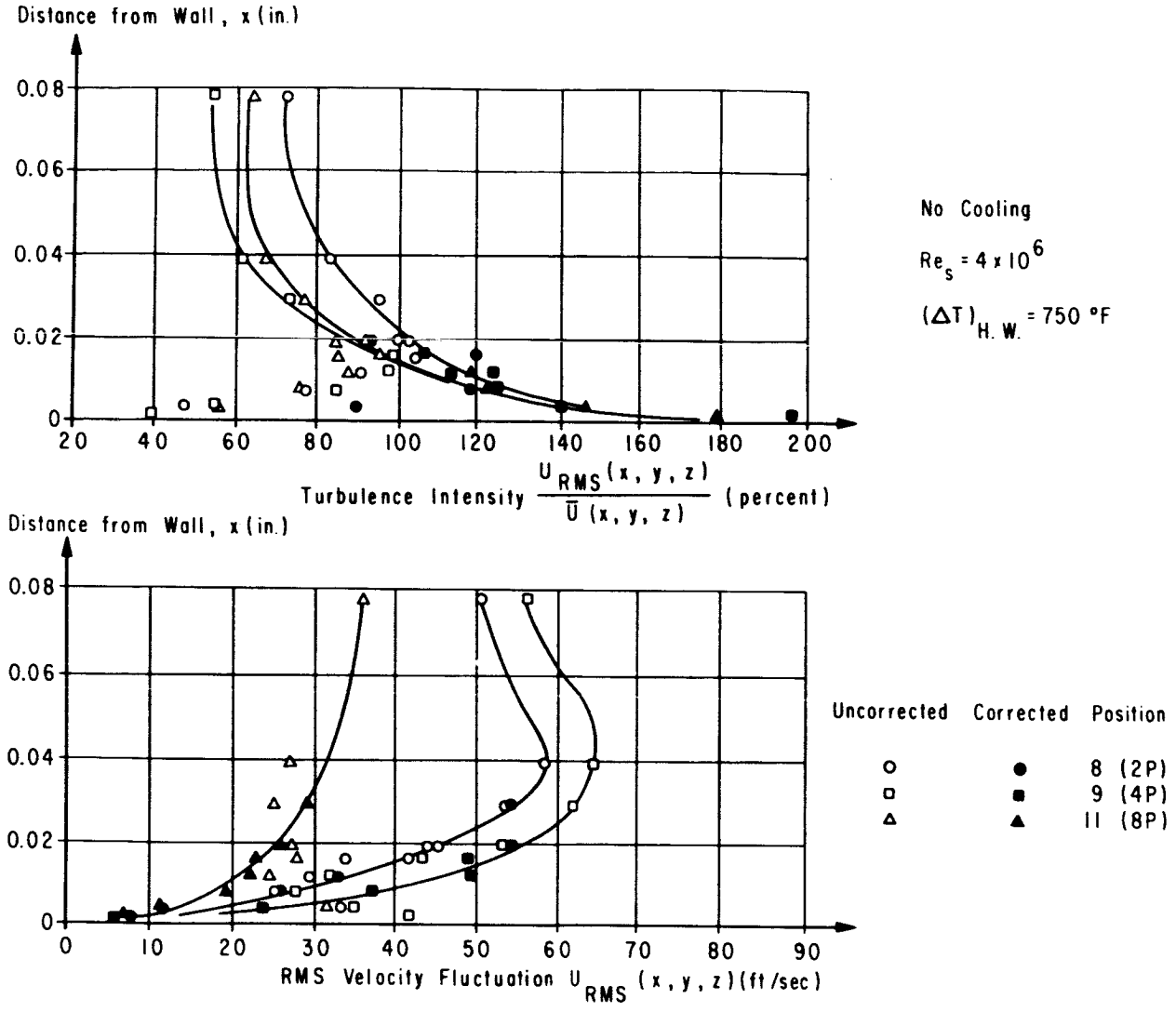

FIGURE 15. RMS VELOCITY PROFILES IN TWO-DIMENSIONAL BASE FLOW INCLUDING CORRECTION FOR WALL EFFECT

VI. HEAT TRANSFER

Heat transfer rates were measured as a function of location (coordinates 0,y,z), the base plate temperature T_b, and the forebody Reynolds number Re_s. All measurements utilized the transient technique discussed in Section II C.

A typical area distribution of the heat transfer rate is shown in Figure 19. The measured values vary between 1900 and 2400 Btu/ft^2 hr, or within ±12 percent of the mean. The heat transfer rates reach a maximum at the stagnation point (thermocouple 3), and fall off in both the y and z directions, except for the vertical traverse through thermocouple positions 7 and 9. This behavior is to be expected because of the deviations from two-dimensional stagnation point flow, although the adjusted laminar stagnation-point calculations predict a constant heat transfer rate if a linear velocity variation exists.

The total heat transfer coefficient

$$h_{tot} = \frac{\dot{q}_A}{T_r - T_b} \qquad (8)$$

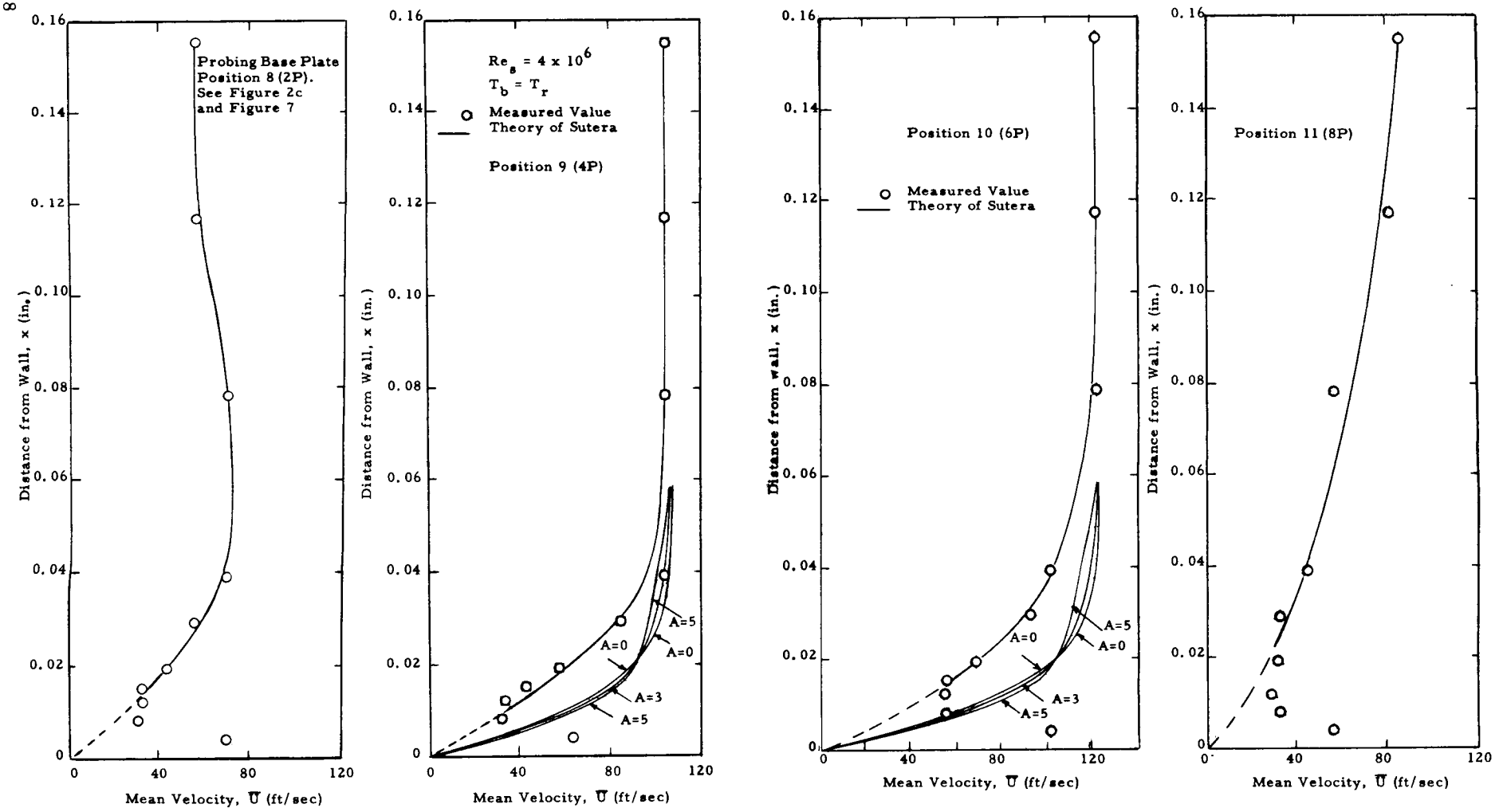

Figure 16. Mean Velocity Profiles

FIGURE 16. MEAN VELOCITY PROFILES

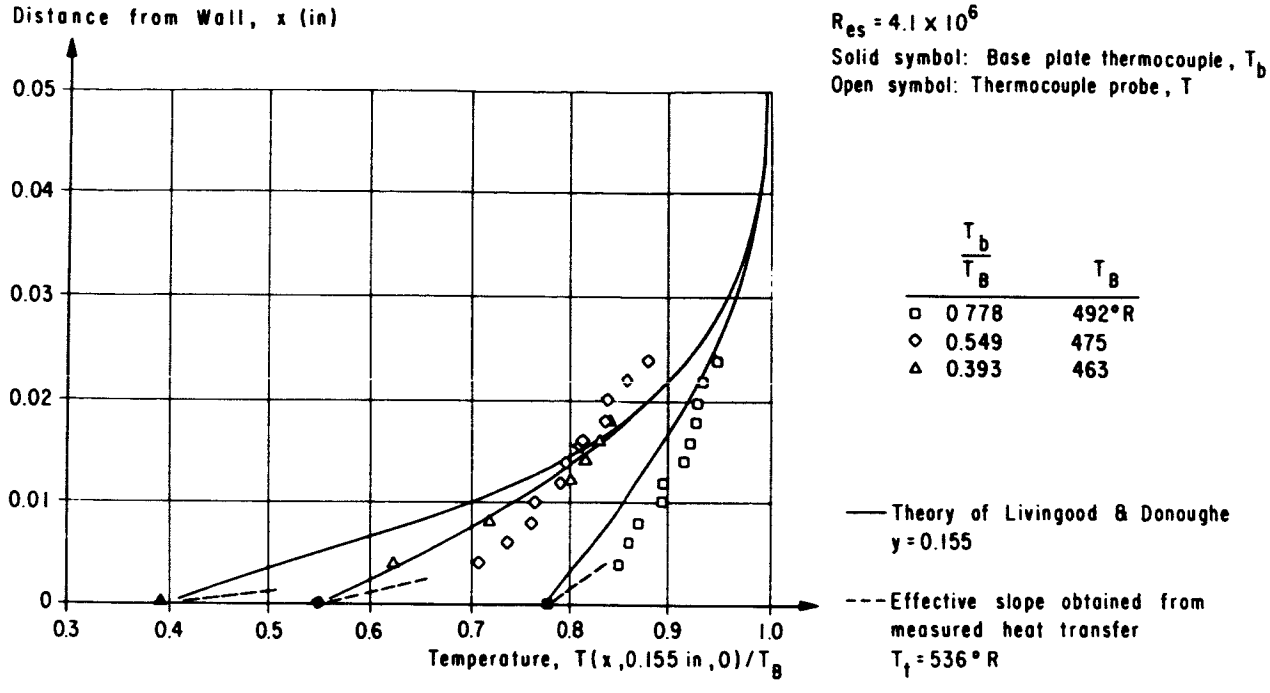

FIGURE 17. BOUNDARY LAYER PROFILES OF STAGNATION TEMPERATURE FOR DIFFERENT COOLING RATES

$Re_s = 4.1 \times 10^6$
$T_f = 528°$ R

○ From Heat Transfer Data (Heat Trans. Base Plate)
□ From Temperature Profiles (Probing Base Plate)

$182° R \leq T_b \leq 509° R$
$454° R \leq T_B \leq 509° R$

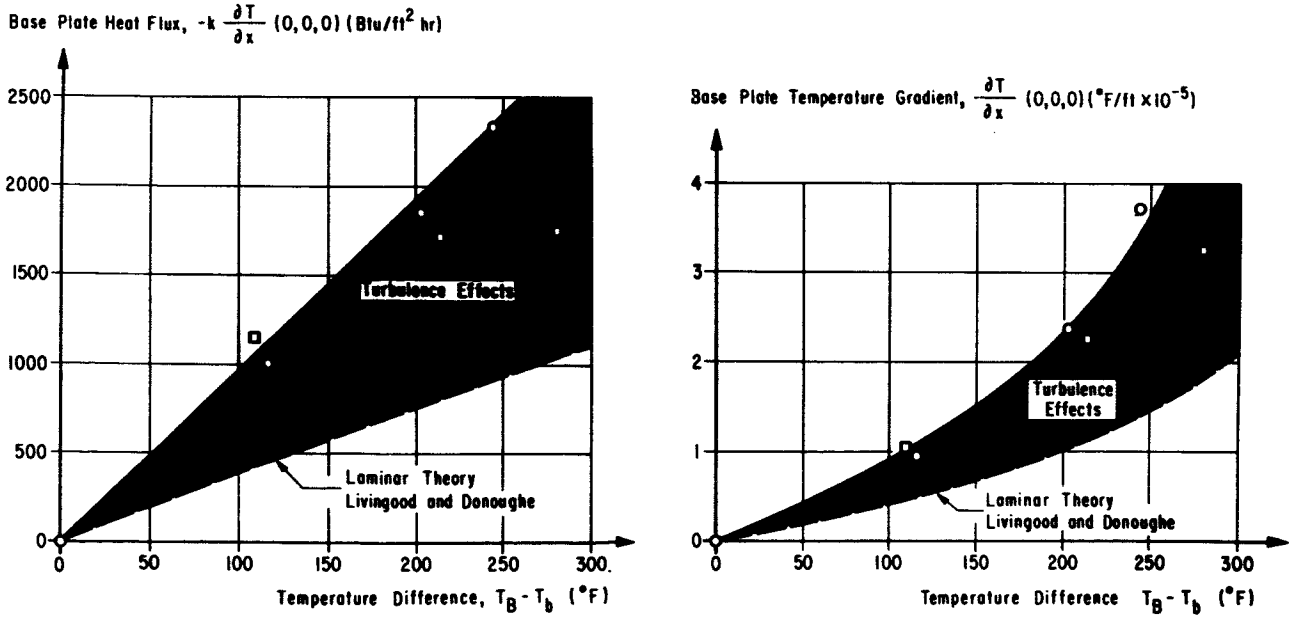

FIGURE 18. THE EFFECT OF TURBULENCE LEVEL ON BASE HEAT TRANSFER

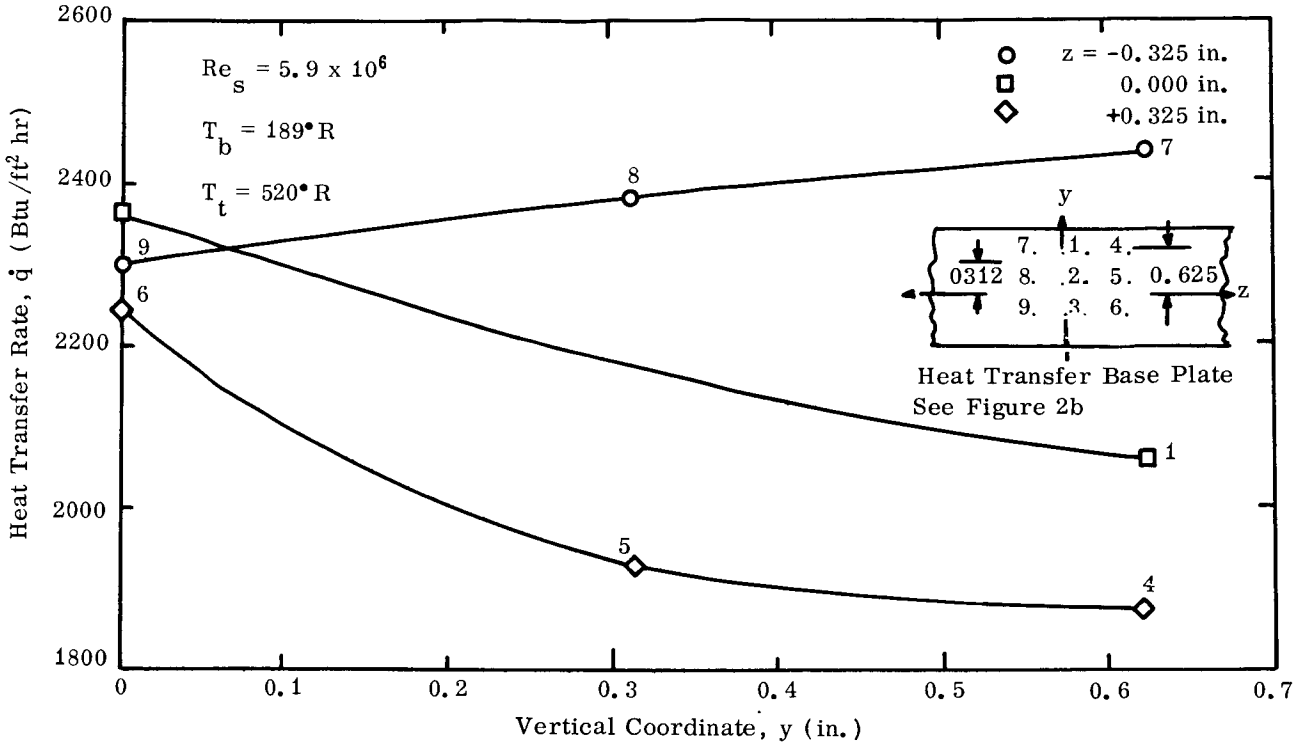

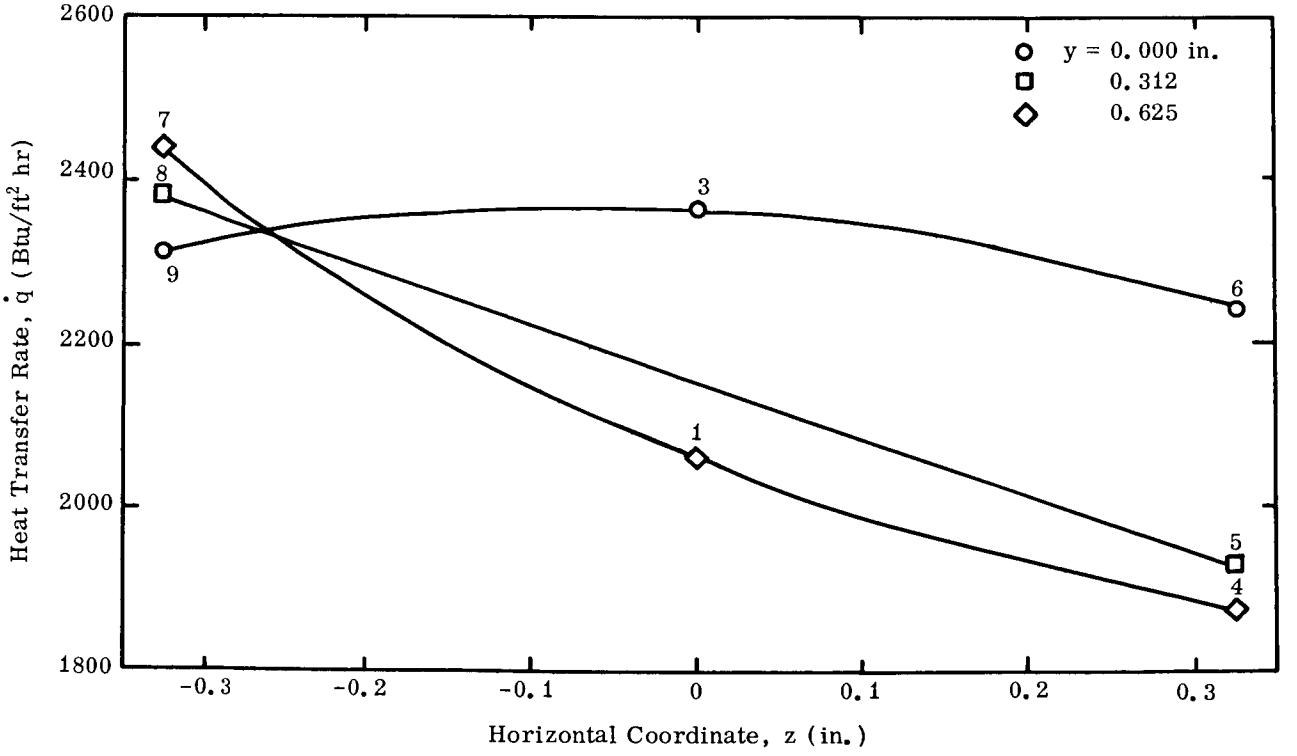

FIGURE 19. DISTRIBUTION OF BASE HEATING RATES

is shown in Figure 20. We have tried to suppress dependence on position by using the area-averaged heat transfer rate $\dot{q}_A$ only. The effects of base plate temperature are eliminated by replacing the heat transfer rate with the heat transfer coefficient h_{tot}. If the heat transfer rate $\dot{q}_A$ increases linearly with increasing temperature difference $(T_r - T_b)$, h_{tot} should be independent of the cooling rate. Actually, the variation with base plate temperature T_b is slightly nonlinear as shown in Figure 18, which explains the cluster of points at each Reynolds number.

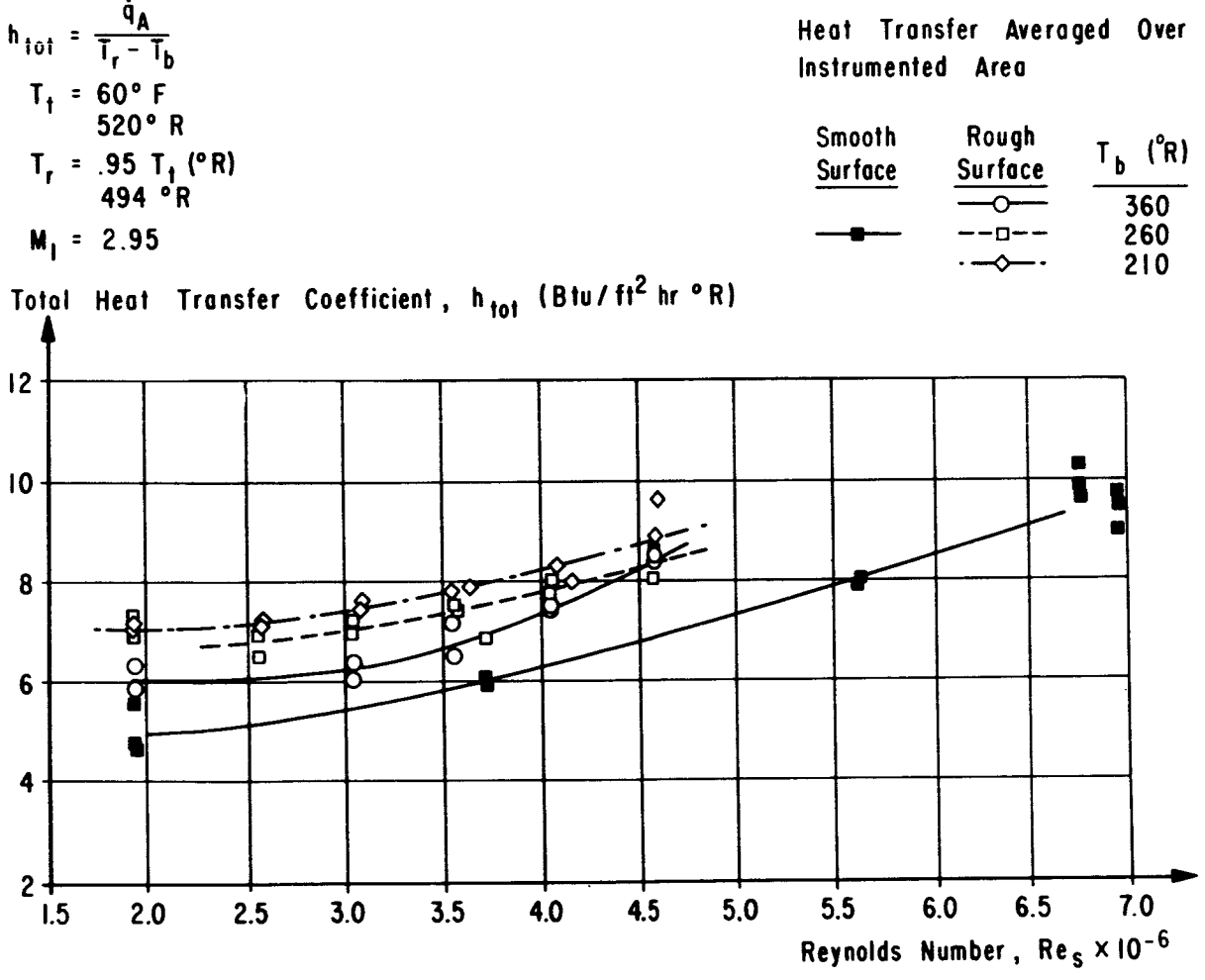

FIGURE 20. VARIATION OF TOTAL HEAT TRANSFER COEFFICIENT WITH REYNOLDS NUMBER

A. HEAT FLOW RESISTANCE OF FREE SHEAR LAYER AND BASE BOUNDARY LAYER

All of the heat flowing into the base plate must come from adjacent jets. The transport of this heat is by conduction through the free shear layer, conduction through the base boundary layer, and convection in the recirculation process. However, the conductive transport can be analyzed separately if we let the dividing streamlines define the boundaries of a control surface for heat transfer "through" the jet shear layer. Since the net mass transfer across each surface element is zero, there is no net convective transport. Consequently, the convective recirculation process operates only internally to create a base recirculation zone of constant temperature; that is, it establishes a region of a very high "apparent" heat conductivity. The heat which flows into the base must also be conducted through the two dividing streamlines. We can draw an analogy to

electrical current flow by assuming the jet shear layer and the base boundary layer act as two heat flow "resistances" in series, connected by a region of high heat conductivity whose resistance may be neglected. To estimate the magnitude of these two resistances, we define new heat transfer coefficients, h_{SL} and h_{BP}, for the jet shear layer and the base plate boundary layer. Then

$$\dot{q}_A = h_{SL} (T_r - T_B) = h_{BP} (T_B - T_b)$$

$$= h_{tot} (T_r - T_b) \qquad (9)$$

where

T_r = recirculation zone and base recovery temperature

T_B = recirculation zone temperature

T_b = base plate temperature.

This concept of two heat flow resistances in series has also been used recently by Page and Dixon [18], although they refer to the second resistance as that provided by the "recirculating flow." In a mathematical description, the term "resistance" is now identified with the reciprocal of the heat transfer coefficient ("conductivity").

$$1/h_{tot} = 1/h_{SL} + 1/h_{BP} \ , \qquad (10)$$

which uses the additive property of series resistances. A comparison between the resistance of the base boundary layer and the total resistance is then given by

$$\frac{h_{tot}}{h_{BP}} = \frac{T_B - T_b}{T_r - T_b} \ . \qquad (11)$$

To obtain an average value, independent of the base cooling rate, we shall approximate the measured dependence of T_B on T_b (Fig. 12) with the straight line

$$T_B = T_r + \frac{\partial T_B}{\partial T_b} (T_b - T_r)$$

$$= T_r + 0.143 (T_b - T_r) \qquad (12)$$

for $Re_s = 4.5 \times 10^6$. Substitution into the previous equation gives

$$\frac{h_{tot}}{h_{BP}} = 1 - \left(\frac{\partial T_B}{\partial T_b}\right)_{T_B = T_r} = 0.857. \qquad (13)$$

Accordingly, 86 percent of the total heat flow resistance can be attributed to the thermal base boundary layer, which clearly indicates its dominance in the base heating process. The remaining heat flow resistance is provided by the jet shear layer, such that

$$\frac{h_{tot}}{h_{SL}} = 1 - \frac{h_{tot}}{h_{BP}} = \left(\frac{\partial T_B}{\partial T_b}\right)_{T_B = T_r} = 0.143. \qquad (14)$$

The foregoing results have been obtained for one reference Reynolds number, $Re_s = 4.5 \times 10^6$. To show the heat transfer coefficient of the base boundary layer and the free shear layer as a function of Reynolds number, we have repeated this calculation for other test conditions, converting to the non-dimensional Stanton number

$$St = \frac{h_{tot}}{\rho_2 \bar{U}_2 c_{p2}} \ , \qquad (15)$$

where the density, velocity and specific heat (ρ_2, $\bar{U}_2$, c_{p2}) have been evaluated at the outer (high speed) edge of the jet shear layer. This enables us to compare our free shear layer heat transfer coefficient with those of Korst, et al. [19].

The expansion process of the forebody boundary layer is known to be essentially isentropic [20, 21], at least in the supersonic portions; so the calculations of the properties at the outer edge of the shear layer were based on the measured base static pressure ratio p_b/p_1, using the assumption of constant total pressure $p_2 = p_1$. This also assumed that the lip shock wave is of negligible strength.

The static-to-total-pressure ratio

$$\frac{p_2}{p_{t2}} = \frac{p_b}{p_{t2}} = \left(\frac{p_b}{p_1}\right)\left(\frac{p_1}{p_{t1}}\right)_{M=2.95} \qquad (16)$$

can thus be calculated; and the Mach number M_2, density ρ_2 and velocity $\bar{U}_2$ at the outer edge follow from isentropic flow tables and the known stagnation temperature T_t.

The results of the free shear layer heat transfer data are summarized in Figure 21, which also shows Korst's semiempirical results depending on the choice of the spreading parameter σ. The plotted

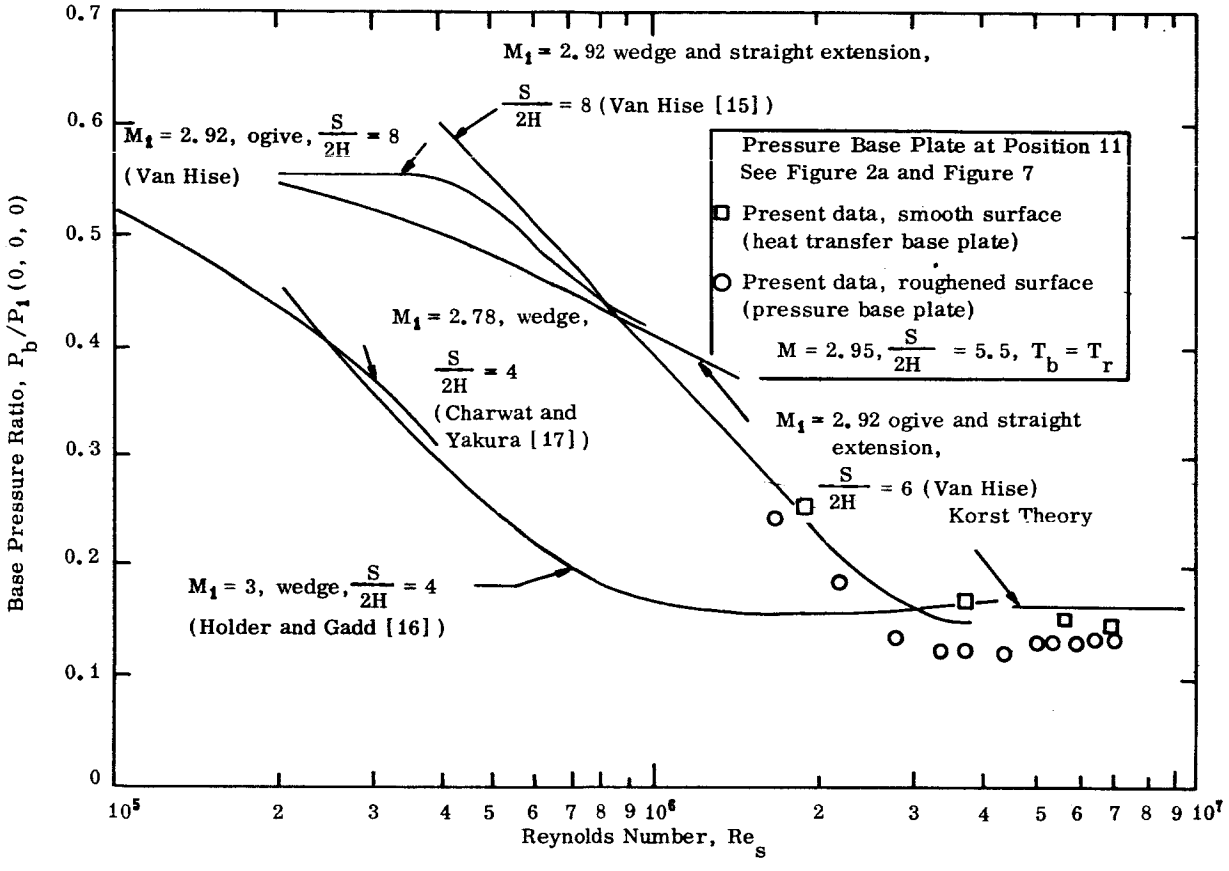

FIGURE 21. BASE PRESSURE VARIATION WITH REYNOLDS NUMBER

values take account of the fact that Korst based his transfer coefficient h_{SL} on the area of the dividing streamline, whereas we utilized the base area. The data agree fairly well for $\sigma = 12$, the incompressible value. Korst recommends that σ be calculated from the formula,

$$\sigma = 12.0 + 2.76\, M_2 = 24.2, \qquad (17)$$

suggested by Tripp [22] and based on values for jets exhausting into still air; but this evidently leads to large discrepancies. Because of the differences in the flow fields this value may not be applicable to our case.

B. REYNOLDS NUMBER EFFECTS

The predominant heat flow resistance of the base boundary layer and the extremely high turbulence levels have been found at comparatively small Reynolds numbers. In order to draw conclusions on base heating and acoustical loads in flight one would like to extrapolate the result to full scale Reynolds numbers. A first step in this direction is to consider the Reynolds number dependence over the tested Reynolds number range. Additional measurements at higher Reynolds numbers are presently prepared.

The measured total, Stanton numbers appear to decrease slightly with an increasing Reynolds number,

as shown in Figure 22. However, this trend is barely recognizable within the measuring accuracies and any extrapolation of flight Reynolds numbers is very questionable.

In view of the extremely high turbulence levels, one might argue that an increase in Reynolds number should not affect the heating rates very much. The Reynolds number independence of highly turbulent

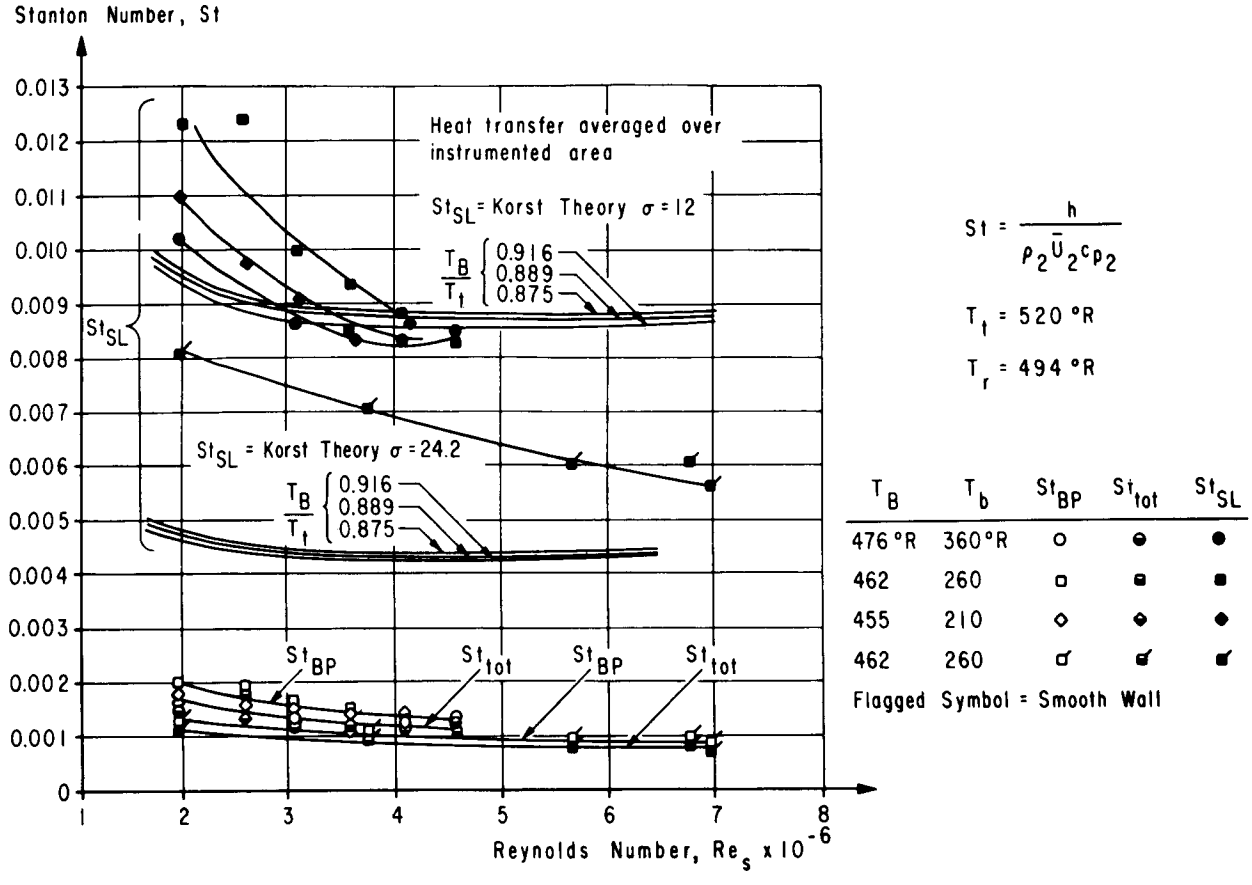

FIGURE 22. VARIATION OF TOTAL, SHEAR LAYER, AND BASE PLATE HEAT TRANSFER COEFFICIENTS WITH REYNOLDS NUMBER

flows has been established for mean velocity profiles in true shear layers and above rough walls. In such cases the shear stresses are directly proportional to the dynamic pressure $\rho\bar{U}^2$. The linear variation of the stagnation point velocity gradient with Reynolds number (Fig. 14) now suggests that the shear stress in the base boundary vanes with the stream density ρu rather than the dynamic pressure. The base boundary layer therefore exhibits an unexpected Reynolds number dependence and any extrapolation beyond the tested Reynolds number range remains questionable, even if one uses physical analogies.

The dimensional heat transfer rates (Fig. 2) do show a significant increase with Reynolds number. This Reynolds number dependence is provided almost entirely by the Reynolds number dependence of the recirculation base density, since the Stanton number itself is almost independent from the Reynolds number. For the uncooled base the density and pressure are directly proportional. The Reynolds number dependence of density may therefore be evaluated from the plot of base pressure versus Reynolds number, which is given in Figure 22. The measurements indicate the typical "jump" which is known from laminar turbulent transition and may be attributed to transition effects of the forebody boundary layers. In actual flight, the forebody boundary layers (nozzle shear layers) are far from transition. This is an additional reason why the heat transfer rates from small scale model tests should not be extrapolated to full scale Reynolds numbers, in spite of the light turbulence levels.

V. CONCLUSIONS

Heat transfer processes in a two-dimensional recirculation zone behind a blunt trailing edge in a Mach 3 wind tunnel have been studied by hot-wire and total temperature traverses combined with wall pressure and heat transfer measurements. The results indicate:

1. The recirculating flow is subjected to extremely high local turbulence levels of $\approx$ 100 percent, which makes a quantitative hot-wire interpretation difficult.

2. Oscilloscope traces and a third-octave frequency band analysis indicate at least five narrow-band frequency components in the base approach flow. We speculate that one of these is connected with sound radiation emanating from the subsonic hole between the plume impingement shocks and the jet shear layers, while another arises from noise generated by the shear layer.

3. Cooling the base plate produces a constant total temperature throughout the recirculation zone, which is below the recovery temperature. The associated influence of the wall on the remote base approach flow can not be duplicated with a stagnation point analysis.

4. Turbulent reattachment produces thermal and velocity base boundary layers of approximately the same thickness.

5. The high level of turbulence affects both the shape of the mean velocity and the total temperature profiles. Heat transfer rates are correspondingly increased by a factor of 2.

6. The velocity of base boundary layers exhibits an unexpected Reynolds number dependence.

7. The total heat transfer coefficient can be related to the heat transfer coefficients of the base boundary layer and the jet shear layer, which act like two heat flow resistances in series. The thermal base boundary layer contributes 86 percent of the total heat flow resistance and, therefore, dominates convective base heating.

8. The shear layer heat transfer coefficient agrees with Korst's theory when the incompressible $\sigma = 12$ is utilized. This indicates that spreading factors obtained for compressible exhausting jets may not apply to our flow field.

REFERENCES

1. Schlichting, H.: Boundary Layer Theory. Fourth Edition, McGraw-Hill Book Company, Inc., New York, 1960.

2. Sutera, S. P., Maeder, P. F., and Kestin, J.: "On the Sensitivity of Heat Transfer in the Stagnation Point Boundary Layer to Free-Stream Vorticity." Journal of Fluid Mechanics, Vol. 16, pp. 497-519, 1963.

3. Sutera, S. P.: "Vorticity Amplification in Stagnation-Point Flow and its Effect on Heat Transfer." Journal of Fluid Mechanics, Vol. 21, pp. 513-534, 1965.

4. Larson, R. E., Scott, C. J., Elgin, D. R., and Seiver, R. E.: Turbulent Base Flow Investigations at Mach Number 3. University of Minnesota, Rosemount Aeronautical Laboratories, Research Report No. 183, July 1962.

5. Domich, E. G., Jantscher, H. N., and Olson, D. N.: Aeronautical Research Facilities. University of Minnesota, Rosemount Aeronautical Laboratories Research Report No. 152, September 1958.

6. Hanson, A. R., Larson, R. E., and Krause, F. R.: Hot-Wire Techniques in Low Density Flows with High Turbulence Levels. NASA George C. Marshall Space Flight Center, TM X-53295, April 1964.

7. Janssen, J. M. L., Ensing, L., and Van Erp, J. B.: "A Constant-Temperature- Operation Hot-Wire Anemometer." Proceedings of the IRE, Vol. 47, pp. 555-567, 1959.

8. Fingerson, L. M.: A Heat Flux Probe for Transient Measurements in High Temperature Gases. Ph. D. Thesis, University of Minnesota, 1961.

9. Ffowcs-Williams, I. E., and Maidanik, G.: "The Mach Wave Field Radiated by Supersonic Turbulent Shear Flows." Journal of Fluid Mechanics, Vol. 21, pp. 641-657, 1965.

10. Falkner, V. M., and Skan, S. W.: "Solutions of the Boundary Layer Equations." Philosophical Magazine, Vol 12, pp. 865-898, 1931.

11. Sternberg, J.: "A Theory for Viscous Sublayer of a Turbulent Flow." Journal of Fluid Mechanics, Vol. 14, pp. 241-271, 1961.

12. Kuethe, A. M., Wilmarth, W. W., and Crocker, G. H.: "Stagnation Point Fluctuations on a Body of Revolution." Physics of Fluids, Vol. 2, pp. 10-12, 1959.

13. Townsend, A. A.: The Structure of Turbulent Shear Flow. Cambridge University Press, Cambridge, 1956.

14. Livingood, J. N. B., and Donoughe, P. L.: Summary of Laminar Boundary Layer Solutions for Wedge-Type Flow over Convection and Transpiration Cooled Surfaces. NASA TN 3588, 1955.

15. Van Hise, V.: Investigation of Variation in Base Pressure over the Reynolds Number Range in which Wake Transition occurs for Two-Dimensional Bodies at Mach Numbers from 1.95 to 2.92. NASA TN D-167, 1959.

16. Holder, G. W., and Gadd, G. E.: Interactions between Shock Waves, Boundary Layers and Wakes. Symposium on Boundary Layer Effects in Aerodynamics, National Physical Laboratory, Teddington, England. Philosophical Library, Inc., New York, 1955.

17. Charwat, A. F., and Yakura, J. K.: "An Investigation of Two-Dimensional Supersonic Base Pressures." Journal of the Aeronautical Sciences, Vol. 25, No. 2, 1958.

18. Page, R. H., and Dixon, R. J.: Base Heat Transfer in a Turbulent Separated Flow. The Boeing Company, Document D2-20191-1, 1963.

19. Korst, H. H., Chow, W. L., and Zumwalt, G. W.: Research on Transonic and Supersonic Flow of a Real Fluid at Abrupt Increases in Cross Section. University of Illinois, Engineering Experiment Station Report NE 392-5, 1959.

20. Murthy, K. R. A., and Hammit, A. G.: Investigation of the Interaction of a Turbulent Boundary Layer with Prandtl-Meyer Expansion Fans at M = 1.88. Princeton University, Department of Aeronautical Engineering Report 434, 1958.

21. Morkovin, M. V.: Effects of High Acceleration on a Turbulent Shear Layer. Proceedings of the 1955 Heat Transfer and Fluid Mechanics Institute, Stanford University Press, Stanford, 1955.

22. Tripp, W.: Analytical and Experimental Investigation of the Base Pressure behind a Blunt Trailing Edge for Supersonic Flow. Ph. D. Thesis, University of Illinois, 1956.

II. FLUID MECHANICS

FLUID MECHANICS REGIMES RELATED TO PROPELLANT OSCILLATIONS UNDER LOW GRAVITY CONDITIONS

By

Harry J. Buchanan

SUMMARY

This paper presents a discussion of the basic regimes of fluid mechanics pertinent to propellant oscillation problems. In particular an explanation is given of some of the fluid phenomena observed under low gravity conditions in terms of certain dimensionless products which are used to define the regimes of fluid behavior: ordinary high gravity sloshing, ordinary low gravity sloshing, low gravity sloshing predominated by liquid moving along the container surface, and sloshing involving breaking of the surface by splashing or spraying.

LIST OF SYMBOLS

a	Tank radius
Bo	Bond number
F	Force
Fr	Froude number
g_o	Acceleration due to gravity at sea level
$\bar{g}$	Vehicle acceleration prior to main engine shutdown
g	Vehicle acceleration after main engine shutdown
L	Characteristic length
r	Radius measured from tank centerline
V	Velocity of fluid elements at free surface
We	Weber number
ρ	Fluid mass density
σ	Fluid surface tension
ζ_w	Slosh wave amplitude at tank wall
ω	First mode slosh frequency

INTRODUCTION

In the past, problems relating to propellant oscillations in the tanks of launch vehicles have been concerned primarily with the boost phase of flight where body forces due to vehicle acceleration are fairly large. Recently, with the advent of liquid fueled space vehicles designed to restart after an extended period in a near weightless condition, interest in problems involving low gravity propellant oscillations has increased. As of yet little progress has been made toward solving these problems. One of the specific problems to which considerable attention has been turned involves the dynamic behavior of liquids following a large reduction in vehicle acceleration.

At main engine shutdown the space vehicle experiences a transition from a high forward acceleration to a low deceleration resulting from aerodynamic drag. For ordinary tanks the fluid will then reorient to a position of minimum potential energy. Since the fluid will move to the other end of the tank when this acceleration sign change takes place, one design philosphy has been to prevent this by applying sufficient thrust to insure a small forward acceleration. Under these conditions, if the fluid were initially at rest, the free surface would merely adjust its slope to minimize the potential energy. While the resulting motion might require considerable time to damp out, it is not particularly violent. On the other hand, if the fluid is sloshing initially, which is certainly the most likely case, a considerable amount of energy is possessed by the fluid. How this energy will be divided into potential and kinetic energy depends upon the phasing of the main engine cutoff. If this event takes place when the kinetic energy of the fluid is large, a particularly violent motion can result.

FLUID DYNAMIC REGIMES

In order to examine qualitatively the dynamic behavior of the liquid for the case described above, consider four basic fluid mechanics regimes for describing sloshing phenomena. Figure 1 illustrates these regimes in terms of the Weber and Froude numbers. The Weber number ($We = \frac{\rho V^2 L}{\sigma}$) represents the ratio of the inertial forces to the capillary forces, and the Froude number ($Fr = \frac{V^2}{gL}$) is the ratio of inertial forces to body forces. The Bond number ($Bo = gL^2\rho/\sigma$) is equal to the Weber number divided by the Froude number.

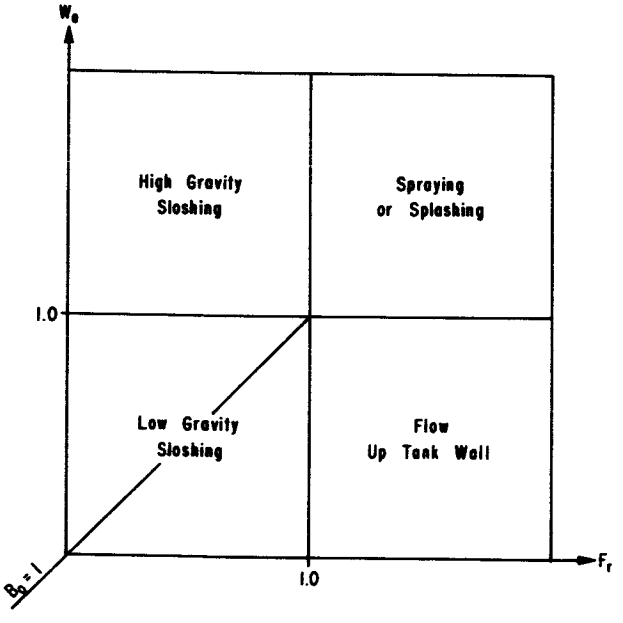

FIGURE 1. SLOSHING FLUID MECHANICS REGIMES

A. HIGH GRAVITY SLOSHING

This is the familiar case experienced in tests conducted at 1 g and in flight tests at several g's. Here the body forces predominate over inertial forces, and inertial forces are very large compared to surface tension forces. In terms of the above dimensionless products, this regime is defined by:

$Fr < 1.0$, $We > 1.0$, $Bo > 1.0$.

The resulting fluid motion in this regime has been thoroughly treated, both analytically and experimentally, by a number of investigators [1-4]. The slosh wave is essentially planar as indicated in Figure 2.

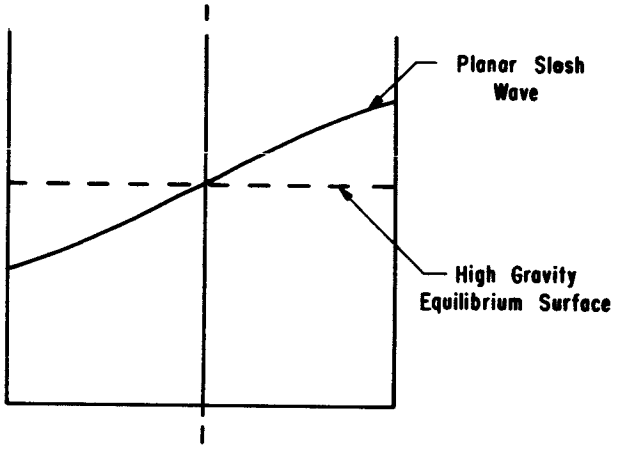

FIGURE 2. HIGH GRAVITY SLOSHING

B. LOW GRAVITY SLOSHING

In this regime capillary forces and body forces both are greater than inertial forces. In terms of the dimensionless products this condition can be described by

$Fr < 1.0$ $We < 1.0$.

For these conditions the fluid oscillates or sloshes, but the resulting wave shape is entirely different from that for high gravity sloshing, as shown in Figure 3. A detailed solution for this motion is not

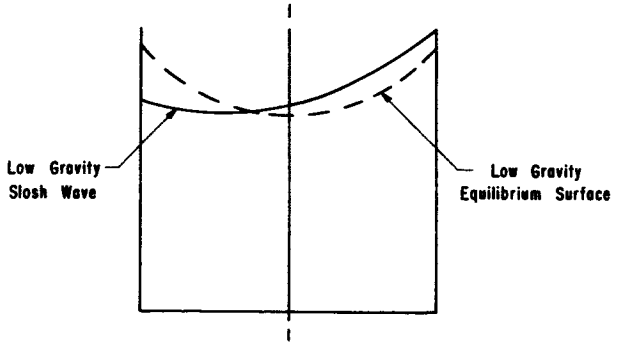

FIGURE 3. LOW GRAVITY SLOSHING

yet available although a method for determining the natural frequency was developed [5]. This region can be divided into two subregions by detailed consideration of the restoring mechanism. In one case the body forces provide the most important restoring force; however, capillary forces cannot be entirely ignored. This regime is described by

$$We > Fr \quad Bo > 1.0.$$

In the second case capillary forces supply the primary restoring mechanism, for this situation

$$We < Fr \quad Bo < 1.0.$$

C. FLOW UP TANK WALL

This is the regime which is apparent in the drop tests; it occurs where inertial forces predominate over body forces; however, capillary forces remain stronger than inertial forces. For this case

$$Fr > 1.0 \quad We < 1.0 \quad Bo < 1.0.$$

In this regime the fluid climbs the container walls, while the surface is prevented from spraying by the surface tension forces.

D. SPRAYING

This last regime is characterized by liquid spraying or splashing. This occurs when the capillary forces can no longer resist the inertial forces which already exceed the body forces. For this condition

$$Fr > 1.0 \quad We > 1.0.$$

The Bond number for this case can be either high or low. For high Bond numbers the spraying criterion has been derived [6] and is consistent with the criterion put forward here.

EVALUATION OF DIMENSIONLESS NUMBERS

Figure 1 and the suggested regimes are of little practical significance unless expressions for Fr and We can be derived which correspond to the ratios described.

$$Fr = \frac{F_{Inertial}}{F_{Body}} = \frac{\rho V^2 a^2}{\rho a^3 g} = \frac{V^2}{ag} \qquad (1)$$

$$We = \frac{F_{Inertial}}{F_{Capillary}} = \frac{\rho V^2 a^2}{\sigma a} = \frac{\rho V^2 a}{\sigma} \qquad (2)$$

In order to evaluate the velocity, V, let us assume that we are interested only in the main engine cutoff phasing which produces the maximum kinetic energy. Since this corresponds to the maximum velocity, it will also produce the maximum inertial force. If the slosh wave prior to main engine cutoff can be assumed to be planar, the velocity of the fluid particles at the surface becomes

$$V = \zeta_w \, r/a \, \omega \qquad (3)$$

and, since the maximum velocity is at the wall,

$$V_{max} = \zeta_w \omega \qquad (4)$$

The Froude number can now be rewritten

$$Fr = \frac{\zeta_w^2 \omega^2}{ag} \qquad (5)$$

and, in like manner, the Weber number

$$We = \frac{\rho \zeta_w^2 \omega^2 a}{\sigma} \qquad (6)$$

By setting Fr = We = 1.0 in (5) and (6), it is possible to arrive at the equations for the lines dividing the various regimes in Figure 1.

From (5)
Fr = 1.0 $$\zeta_w = \sqrt{\frac{ag}{\omega^2}} \qquad (7)$$

From (6)
We = 1.0 $$\zeta_w = \sqrt{\frac{\sigma}{a\rho\omega^2}} \qquad (8)$$

RESULTS

In order to compare the above explanation with the observed phenomena, consider the case shown in Figure 4. This sequence of photographs was

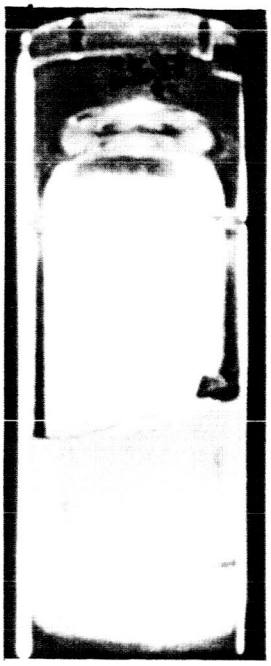

a. High Gravity Sloshing Prior to Drop

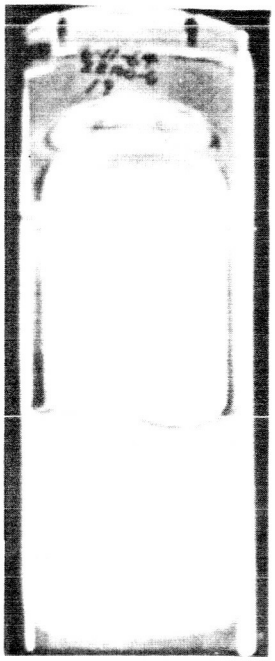

b. Slosh Wave at Drop -Maximum Kinetic Energy

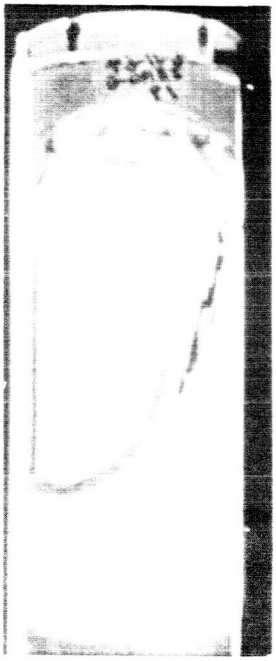

c. Flow up Tank Wall

d. Flow around Tank Completed

FIGURE 4. FLOW UP WALL
TANK DIAMETER: 3 INCHES
FLUID: CARBON TETRACHLORIDE
FACILITY: NORTH AMERICAN
AVIATION DROP TOWER

taken from a drop tower test conducted by North American Aviation and shows a model of one of the Apollo Service Module propellant tanks. The test procedure was to establish an initial slosh wave at 1 g and then to release the package to produce the maximum kinetic energy. Since this tank is nearly cylindrical, the natural frequency prior to drop is given [1] by

$$\omega^2 = (18)\ \frac{\bar{g}/g_o}{a} \quad . \tag{9}$$

Then from (7), Fr = 1.0

$$\zeta_w = .74\sqrt{a^2\ \frac{g/g_o}{\bar{g}/g_o}} \tag{10}$$

and from (8), We = 1.0

$$\zeta_w = .74\sqrt{\frac{\sigma/\rho}{\bar{g}/g_o}} \quad . \tag{11}$$

Using equations (10) and (11) it is possible to define the four regimes in terms of ζ_w and g. Figure 5 was constructed using the dimensions and fluid properties for the model shown in Figure 4. The shaded region indicates the acceleration level experienced in the North American test facility. From the photographs it appears that the wave height is sufficient to initiate spraying. However, these boundaries define only the onset of each of these regimes. Actually all the fluid participating in the motion must have a velocity equal to or greater than that associated with this wave height. Therefore, the wave height required to produce the motion pictured in Figure 4 would probably be greater than that indicated by Figure 5. It appears that the value of the Bond number determines which flow regimes will be possible regardless of wave height. Thus, according to Figure 5, flow up the wall is not possible if Bo > 1.0.

The effect of tank size on the phenomena is demonstrated by considering a much larger tank such as the Saturn S-IVB liquid hydrogen (Fig. 6). The current plan for propellant control requires that an acceleration level of 5×10^{-3} m/sec^2 be applied to the vehicle for 77 seconds following main engine cutoff [7]. Figure 6 indicates that the phenomena involved here include spraying or splash-

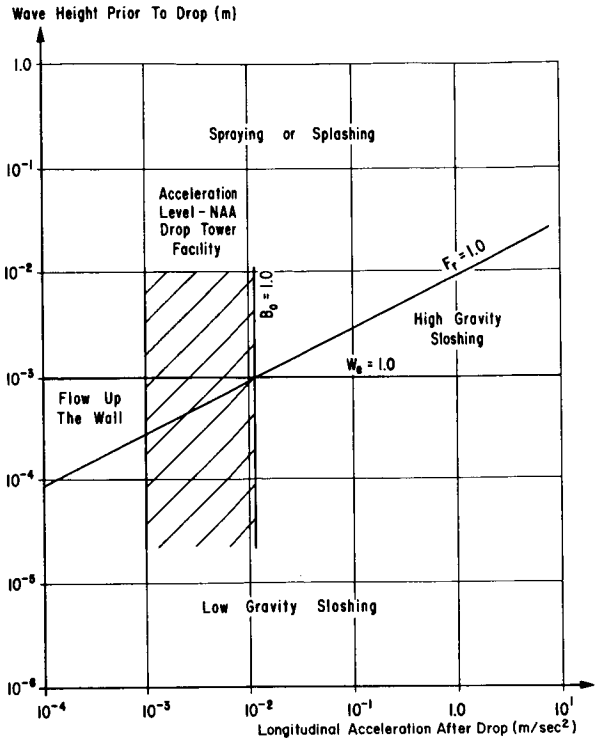

FIGURE 5. SLOSH REGIMES FOR APOLLO SERVICE MODULE PROPELLANT TANK MODEL

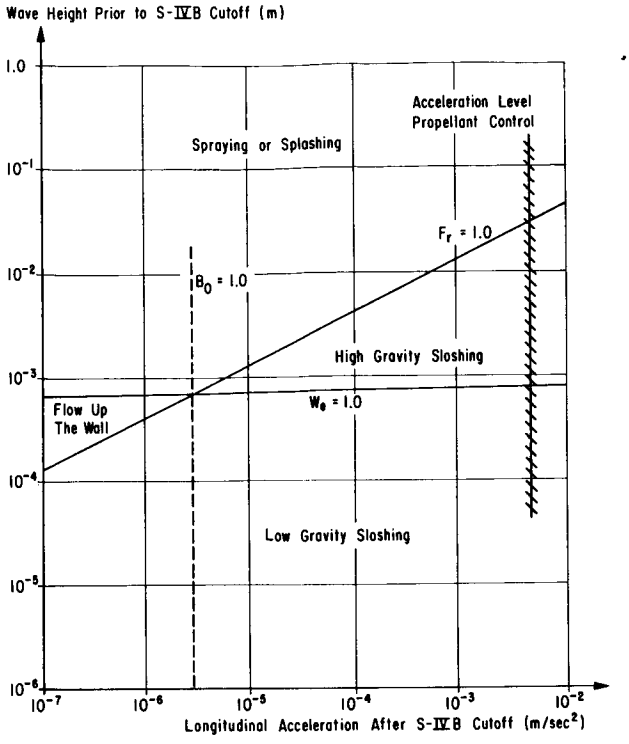

FIGURE 6. SLOSH REGIMES FOR SATURN S-IVB LIQUID HYDROGEN TANK

ing but not flow up the tank wall as pictured in Figure 4. Therefore, it would seem that in large tanks (large Bond numbers) the spraying or splashing phenomena would be more prevalent than that described as flow up the tank wall.

CONCLUSIONS

From the discussion it seems possible to explain for at least some cases the mechanism which produces the flow up the tank wall. Although the method for evaluating the dimensionless numbers is based on several simplifying assumptions, it does offer a means of estimating the possible flow regimes and of scaling experiments. Some subjects for future investigation include the effect of viscous forces and the influence of contact angle or adhesion between the fluid and wall.

REFERENCES

1. Bauer, H. F.: Fluid Oscillations in the Containers of a Space Vehicle and their Influence upon Stability. NASA TR R-187.
2. Lomen, D. O.: Liquid Propellant Sloshing in Mobile Tanks of Arbitrary Shape. Technical Report, GD/A-DDE64-061, General Dynamics/ Astronautics, 1964.
3. Silveira, M. A.; Stephens, D. G.; and Leonard, H. W.: An Experimental Characterization of the Damping of Liquid Oscillations in Cylindrical Tanks with Various Baffles. NASA TN D-715, 1961.
4. Abramson, H. N. and Ransleben, G. E., Jr.: Simulation of Fuel Sloshing Characteristics in Missile Tanks by Use of Small Models. Technical Report No. 3, Southwest Research Institute, 1959.

5. Satterlee, H. M. and Reynolds, W. C.: The Dynamics of the Free Liquid Surface in Cylindrical Containers under Strong Capillary and Weak Gravity Conditions. Technical Report No. LG-2, Standford University, 1964.

6. Eulitz, W. R.: Practical Consequences of Liquid Propellant Slosh Characteristics derived by Nomographic Method. NASA MTP-P&VE-P-63-7, 1963.

7. Swalley, F. E.; Platt, G. K.; and Hastings, L. J.: Saturn V Low-Gravity Fluid Mechanics Problems and their Investigation by Full-Scale Orbital Experiment. Symposium on Fluid Mechanics and Heat Transfer under Low-Gravitational Conditions, 1965.

III. INSTRUMENTATION

REMOTE SENSING WITH OPTICAL CROSS CORRELATION METHODS

By

F. R. Krause and M. J. Fisher

SUMMARY

Our basic concept is to employ the cross correlation of two narrow light beams for remote sensing. The problem with most optical methods such as schlieren, shadowgraph systems or spectrometers is that the received signal is always integrated along the line of sight. However, we want information for a particular spot along the line of sight. To this purpose we adjust a second beam to intersect the first at the point of interest. The integration along the two beams is then eliminated by a cross correlation of the detected fluctuations. This paper indicates how this new concept of combining standard spectroscopy with a statistical cross correlation analysis might be used for turbulence investigations in model tests and in the atmosphere.

The concept has been demonstrated successfully by comparing hot wire measurements with optical cross correlation results. Since remote sensing methods are not limited by scale, AAP applications are conceivable. The main problems in atmospheric and AAP experiments are formulated in terms of questions, such that the background information becomes apparent which is needed to establish the feasiblity of particular experiments.

I. INTRODUCTION

The cross correlation of optical signals has been used for remote sensing in jet shear layers [1]. Concentration fluctuations of a water vapor fog could be resolved with good accuracy in space and time [2]. In principle, the method should also work on an atmospheric scale. Experimental investigations about the generation and motion of atmospheric constituents such as clouds, nuclear debris, ozone, radiation belts, etc., offer an exciting challenge. We will now give a simplified version of our new remote sensing concept and outline some of the problems, which one would have to overcome in atmospheric applications.

II. THE CROSSED BEAM CONCEPT

Remote sensing of distant light sources like planets is based on a fundamental theorem of geometrical optics, which states that the spectral radiance, I, of a source and its image are equal, if one neglects light extinction and emission along the line of sight. The spectral radiance of a distant source is therefore accessible through the spectral radiance of its image on the exit slit of a monochromator, as shown in Figure 1. Source area, ΔA, and wave length interval, $\Delta\lambda$, are set by the optical filter. The solid angle, $\Delta\vartheta$, into which the exit slit radiates, is set by the photodetector. Therefore, the received radiative power is directly proportional to the spectral radiance, I, of the distant source:

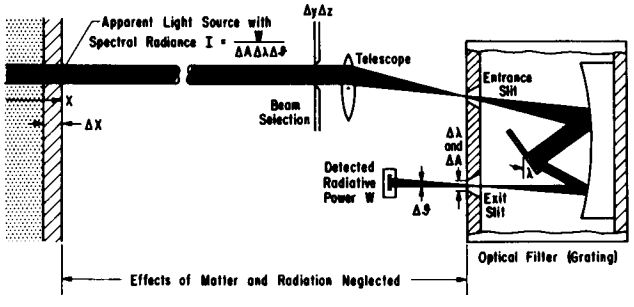

FIGURE 1. REMOTE SENSING OF DISTANT LIGHT SOURCES

$$I(\vec{x} \to -\infty, t, \lambda) = I_s(t, \lambda)$$

$$= \frac{w(\vec{x} \to +\infty, t, \lambda)}{\Delta A \ \Delta\vartheta \ \Delta\lambda} = I_d \,. \qquad (1)$$

However, if the line of sight goes through the atmosphere, the detected spectral radiance $I_d(t, \lambda)$ is changed due to the light extinction or emission in the detector's field of view. In the two limiting cases of dominant extinction or dominant emission, the change in spectral radiance

$$I_d(t, \lambda) = I(\vec{x} \to +\infty, t, \lambda) \; e^{-\int_{-\infty}^{+\infty} K(\vec{x}, t, \lambda)\, dx} = I_s(t, \lambda)\, e \qquad (2)$$

may be expressed by integrating the extinction or emission coefficient

$$K(\vec{x}, t, \lambda) = \frac{1}{I} \frac{\partial I}{\partial x} = K(\vec{x}, \lambda) + k(\vec{x}, t, \lambda). \qquad (3)$$

In astronomy and optical communication, these effects are a nuisance. From an atmospheric science point of view, they can be used to study the thermodynamic properties of the atmosphere, since the extinction coefficient K is uniquely determined by the thermodynamic properties.

The problem with local measurement of atmospheric properties is how to retrieve the local information that is buried in the integrated signal. A solution is possible only by repeating the remote sensing as a function of the remaining independent variables, such that some mathematical transformation can be used to extract the local extinction coefficient.

Several authors [3 - 8] used the remaining space variables y and z and had to assume axial symmetry. This assumption can be made in the study of single rocket exhaust and flames but not in the atmosphere. Another group [9 - 15] used the dependence on optical wave length λ. They subdivide the line of sight into as many zones as there are isolated molecular bands, and need some advance knowledge about the spatial distribution of temperatures and concentrations. The method worked on a package of controlled burners [16]. In the atmosphere, a larger number of isolated bands which are free from scattering and the advance knowledge are hard to find. However, the "zonal approximation" should be considered as a backup of our cross correlation method, since it does use the same test arrangement.

We use the time aspect to retrieve the local information. Consider the experimental arrangement on Figure 2. Two lines of sight intersect in an atmosphere-fixed point. These lines define a plane which we shall call "turbulence wave front" and a normal in the intersection point (x, y, z) which is called the wave normal. We then measure the spectral radiance I(t, λ) (radiative power/solid angle, area, and wave length interval) along both fields of view, split off the time average signal, $\bar{I}$, cross correlate the fluctuations, i(t), and calculate the quantity, G, as described in Figure 2. Let us assume that the two detecting telescopes have been aligned to the y and z axis of a Cartesian, atmosphere-fixed coordinate system. Each line of sight is denoted by a y or z subscript and each point on the line of sight by the distances η or ζ relative to the intersection point. The quantity G is then equal to

$$G(\vec{x}, \lambda) = \frac{\overline{i_z(t, \lambda)\, i_y(t, \lambda)}}{\overline{I_y} \cdot \overline{I_z}}. \qquad (4)$$

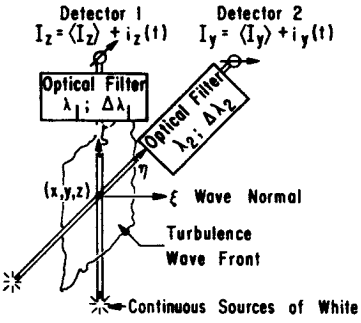

The Crossed Beam Technique Area Integrates the Cross Correlation Function of Light Extinction Coefficients, $K = \bar{K} + k$

$$\frac{\langle i_z(t)\, i_y(t+\tau) \rangle}{\langle I_z \rangle \langle I_z \rangle} = G(\xi, \tau, \lambda)_{\vec{x}} = \int_{-\infty}^{+\infty} \overline{k(x, y, z+\zeta, t, \lambda_1)\, k(x+\xi, y+\eta, z, t+\tau, \lambda_2)}\, d\eta\, d\zeta$$

FIGURE 2. REMOTE SENSING OF LOCAL TURBULENCE THROUGH CROSS CORRELATION OF OPTICAL SIGNALS

The interpretation of the measured quantity G follows by relating it to the local fluctuations, k, of the extinction coefficient. We have shown that G is equal to an area integral over the space time correlation function [17],

$$G(\xi, \tau, \lambda)_{\vec{x}} = \int_{-\infty}^{+\infty} \overline{k(x, y, z+\xi, t, \lambda_1)\, k(x+\xi, y+\eta, z, t+\tau, \lambda_2)}\, d\eta\, d\xi, \qquad (5)$$

provided that the following assumptions are met:

1. The number of statistically independent atmospheric disturbances is small enough to avoid a cancellation of the integrated fluctuation.

2. The integrated fluctuation of the extinction coefficient is small enough to permit linearization.

3. The light source fluctuations and the atmospheric fluctuations are statistically independent.

4. The fluctuations of the two light sources are uncorrelated.

5. Either extinction or emission dominates the change of the detected radiative power.

The second assumption is not very restrictive since the integrated mean value would still be large. Furthermore, the local fluctuation, k, does not have to be small; only the integral over statistically independent fluctuations is assumed to be linearized. In the very few cases where these weak restrictions are not met, one can possibly choose another wave length, λ, where the second assumption is met. The other assumptions can mostly be met by a suitable experimental arrangement. Therefore, the result of equation 5 appears to be sufficiently general for atmospheric applications.

Two important conclusions can be derived from equation 5:

1. For a pair of statistically independent light sources, the source characteristics do not have to be known. The method would work for any source, such as ground beacons, the sun, or reflected sunlight.

2. The random nature of turbulent fluctuations assures that integrand drops to zero over distances which are comparable to a typical eddy size. This explains, qualitatively, why the cross correlation partially eliminates the usual optical integration along a line of sight.

According to equation 5, the crossed beam correlation works whenever the wanted signal is common to both lines of sight. The way in which the wanted signal is then pulled out of the integrated signal may be described best by splitting each of the integrated signals in two parts. The first describes the contribution of the "correlated volume" where the integrand of equation 5 does not vanish. The second part describes the rest of the integrated signal. Multiplying the fluctuations of the two integrated signals then leads to four products. Three of these change between positive and negative values in a random fashion. If we now average these products over time, their mean value will go to zero, whereas the deviation from the mean will increase with the square root of time.

The fourth product describes the contribution of the correlated volume, which is common to both lines of sight. The associated product is always positive, and its summation over time should increase linearly with time. Therefore, it will be the dominant one, if one goes on adding long enough. Even small contributions at the beam intersection can be pulled out provided (1) the integrated signals show detectable fluctuations and (2) the combination of light source fluctuations, shot noise and instrument noise is not orders of magnitudes larger than the root mean square value of the integrated signal.

III. MEASURABLE TURBULENCE PARAMETERS

The optical integration is restricted to the wave front. Along the wave normal, no integration takes place and local information inside a correlated volume may be obtained by repeating the crossed beam experiment for several beam separations along the normal as shown in Figure 3. The space separation, ξ, describes the minimum beam distance, which defines the wave normal. Also a time separation is introduced electronically by a time delay unit. As will be discussed later, the measured signal, G, then approximates a two-point product mean value, which would have been measured by point probes on the wave normal.

$$\frac{G(\xi, \tau, \lambda)_{\vec{x}}}{G(0, 0, \lambda)_{\vec{x}}} = \frac{\overline{i_z(t)\, i_y(t+\tau)}}{\overline{(i_z(t)\, i_y(t))}_{\xi=0}} \cdot \frac{\overline{(I_y)}_{\xi=0}}{\overline{(I_y)}_{\xi\neq 0}}$$

$$\simeq \frac{\overline{k(x, y, z, t, \lambda)\, k(x+\xi, y, z, t+\tau, \lambda}}{\overline{k(x, y, z, t, \lambda)\, k(x, y, z, t, \lambda)}} \qquad (6)$$

The position of these imaginary point probes is indicated on Figure 3 by two dots. Thus, all turbulent properties, which are commonly derived from two-point product mean values, may also be approximated with the crossed beam method.

The local integral scale of turbulence is defined by averaging the area under the covariance curve $G(\xi, \tau=0)$ and its graphical evaluation is illustrated on Figure 3.

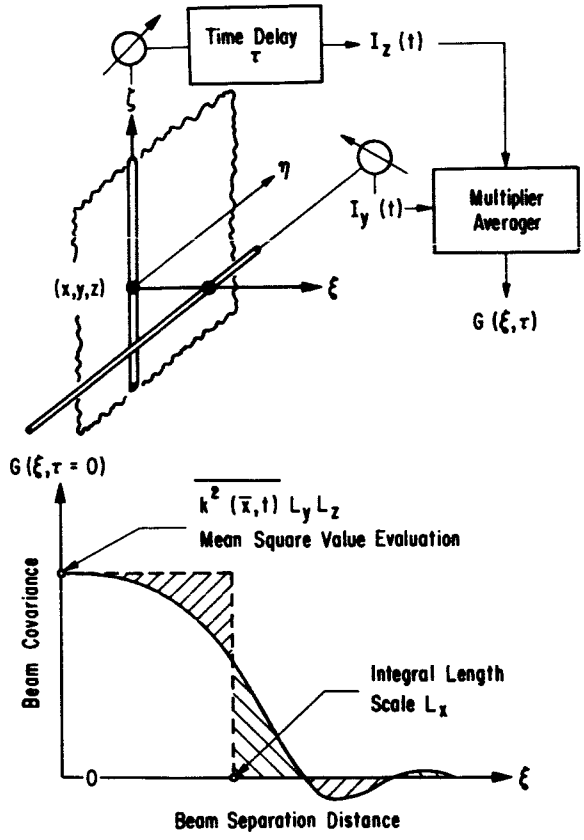

FIGURE 3. TURBULENCE SCALES AND INTENSITIES FROM CROSSED BEAM COVARIANCE MEASUREMENTS

Plotting the beam correlation coefficient against the time separation instead of the space separation (Fig. 4) allows bulk convection speeds to be read. For a given space separation, the correlation will reach a maximum at the time that the turbulent eddies need to travel from the upstream to the downstream beam. The time lag, τ_M, which is indicated by the maximum, is therefore a direct measure of convection speeds.

Power spectra and cross power spectra are defined by a Fourier transform of the measured auto-correlation, $\xi = 0$, and cross correlation $\xi \neq 0$, curves. They may be calculated using the digital computer programs, developed for the analysis of mechanical vibrations [18].

A study of the envelope to the time correlations, $r(\tau)_\xi$, provides a measure of the temporal rate of decay of turbulent eddies as seen by an observer moving with the convection speed. Therefore, the decay of this correlation curve to 1/e of its original value is used to define the average eddy lifetime. The Fourier transform of this envelope would indicate the dominant frequencies which are felt by the moving observer.

Summarizing the graphical evaluations sketched in Figures 3 and 4, we find that the crossed beam method remotely senses integral scales of turbulence, convection speeds, eddy lifetimes and spectra for arbitrarily chosen atmosphere-fixed points at which a beam intersection can be achieved.

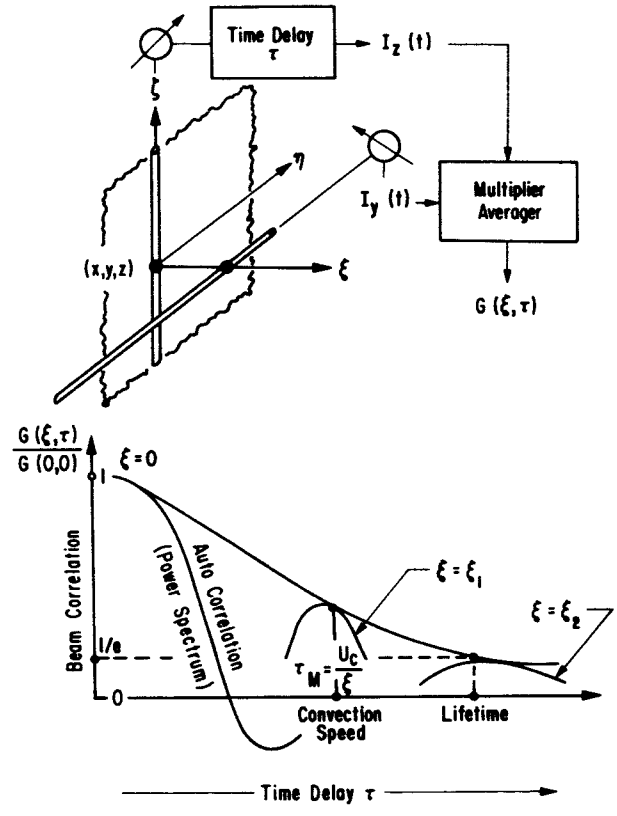

FIGURE 4. LOCAL POWER SPECTRA CONVECTION SPEEDS AND EDDY LIFETIMES FROM CROSSED BEAM CORRELATION MEASUREMENTS

The above turbulent properties are only approximations, since the optical integration over the wave front does catch fluctuations which are not felt by the point probe on the wave normal. However, our experiments in a subsonic jet have shown that weighting of contributions close to the wave normal is sufficiently strong to yield a good spatial resolution. One may thus expect a good spatial resolution on a wide range of other turbulent motions which are of practical interest.

The absorption (or emission) spectrum of extinction coefficients is commonly used to find species concentrations and temperatures of both stagnant gases and small scattering particles. Adjusting the optical wave length of the crossed beams to chosen atomic lines and/or molecular bands, one might therefore extend the spectroscopic methods from stagnant media to inhomogeneous turbulent flows and study multicomponent or two-phase flow phenomena.

IV. EXPERIMENTAL VERIFICATIONS

The most revealing and instructive test of the crossed beam concept is to compare the optical approximation of point measurements with known hot-wire measurements. The initial portion of an axisymmetric free shear layer was chosen for the experiments since (1) the turbulence is anisotropic and inhomogeneous and (2) convection speeds, turbulence scales and eddy lifetimes are well documented in the literature.

All measurements were taken in a subsonic ($M = 0.2$) air jet exhausting through a one-inch diameter nozzle into the atmosphere (Fig. 5). Light extinction was achieved by spraying a small amount of liquid nitrogen into the settling chamber. This produced small water droplets in the exhaust flow which attenuate the crossed beams by scattering. Later, the nitrogen injection was replaced with water spray which offered a better control of the tracer concentration.

A diagram of the optical and electronic hardware is also shown in Figure 5. A plane mirror and a spherical mirror collect the light from a powerful mercury arc and transmit it as a parallel beam through the jet. A similar mirror combination projects the arc image on the entrance slit of a grating spectrograph. The aperture stop in front of the spectrograph is set at a beam diameter of 2 mm. The photomultiplier then scans the first order spectrum of the grating. In this way, the wave length interval $\Delta\lambda$ and the wave length λ are adjusted by the width of the monochromator slit and the rotation of the grating, respectively. By exchanging light sources, gratings, and photodetectors, the system is able to cover the spectrum from the vacuum ultraviolet ($\lambda = 1200A$) to the infrared ($\lambda = 25\ \mu$).

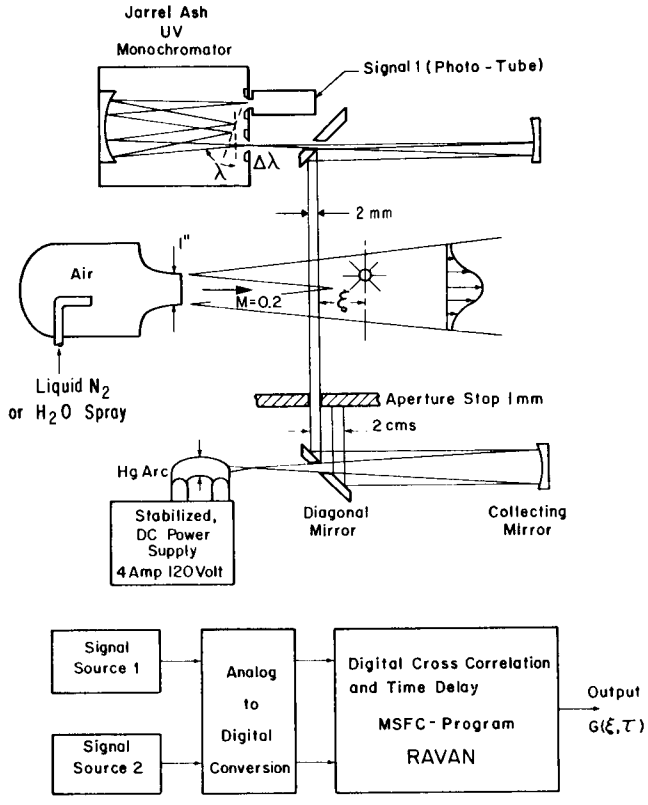

FIGURE 5. BREAD BOARD MODEL OF CROSSED BEAM CORRELATOR

The above light source and detector arrangement is used to generate two beams, one in a horizontal and one in a vertical direction (Fig. 5). A lathe bed provides a mechanical support which allows us to align the beams parallel to the nozzle exit plane. A beam separation in the streamwise direction gives the longitudinal turbulence scales and convection speeds. Transport of the whole system allows us to repeat the measurements for all axial and radial traverses of the jet.

The contribution of correlated light source fluctuations, created by ripple in the power supply, was eliminated using electronic filters. A typical sample of optically measured two-point product mean values is shown in Figure 6. The beam intersection was adjusted to the center of the free shear layer three exit

diameters downstream of the nozzle exit. The turbulent convection process is clearly indicated by the displaced maxima for finite beam separation. The monotonic decay of the envelope shows the decay of the moving eddies. Measuring the time delay for which this curve falls to 1/e of its initial value yields a value of 880 microseconds. This is in excellent agreement with the hot-wire data of [19], from which we estimate that the value of the time scale for our experimental conditions should be 920 microseconds.

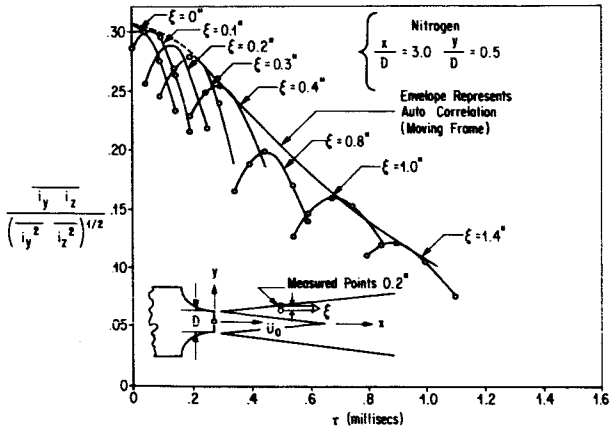

FIGURE 6. CROSS-CORRELATION WITH DOWNSTREAM BEAM SEPARATION

Figure 7 shows the same experiment under different conditions. The initial intersection point of the beams was six diameters from the jet exit, (i.e., at x/D = 6.0) instead of at x/D = 3.0. Instead of using liquid nitrogen to generate a water droplet fog tracer, a small nozzle was mounted in the jet settling tank which sprayed water droplets into the flow to form the tracer fog. The curves do appear to fall onto or close to an envelope as required. Unfortunately, the range of beam separations used is not sufficient to merit the extrapolation of the curve to 1/e of its initial value. Therefore, the moving axis autocorrelation curve has been obtained from the hot-wire data of [19] and is shown as the dotted line superimposed on the measured cross correlation curve.

The spatial resolution of the crossed beam method seems very encouraging, considering that the envelope from the hot-wire data exactly matches the individual curves from the crossed beam method. For the moving frame, the optically measured autocorrelation therefore agrees with the hot-wire curves, regardless of whether nitrogen or water spray was used as a tracer[1].

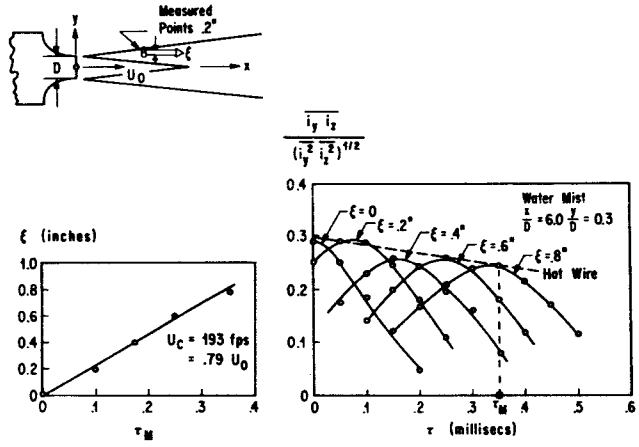

FIGURE 7. CROSS CORRELATION WITH DOWNSTREAM BEAM SEPARATION

A quantitative comparison of individual cross correlation curves $G(\tau)_\xi$ has been based on the indicated convection velocities. These velocities have been evaluated graphically following the procedure of Figure 4. To increase the accuracy, we have always used more than one curve. The chosen set of beam separations was plotted as a function of the time lag values τ_M, which were indicated by the common tangent of envelope and individual cross-correlation curve. The result is a straight line which is shown in the upper part of Figure 7. The desired convection speed follows from the slope of this line.

The results of all convection velocity determinations made using the crossed beam correlation system to date are summarized on Figure 8, where they are also compared with hot-wire data from Reference 19. In the outer portion of the shear layer ($\eta > 0$) the convection

velocity determinations agree within experimental accuracy. For $\eta < 0$, however, the crossed beam results tend to follow the mean velocity profile (U/U_o) rather than attain the constant maximum value observed for hot-wire data. This was not an unexpected result. All convection velocity results presented in Reference 19 were taken at axial stations where the potential core still exists. At these positions, the large difference between the mean velocity and convection velocity has not been completely explained. However, Davies [20] has discussed the subject recently, and it does appear that the closer correspondence between mean and convection velocity observed here is to be expected when a measuring technique other than the hot-wire anemometer is being used, and/or the potential core no longer exists.

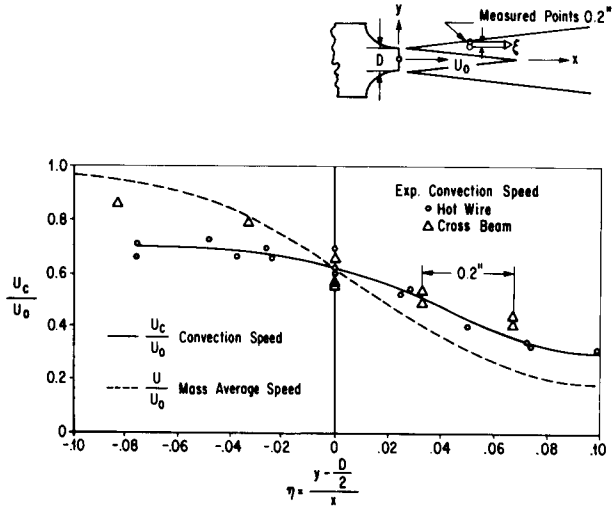

FIGURE 8. VELOCITY PROFILES FROM HOT WIRE AND CROSS BEAM METHODS

The optically measured results in Figure 8 were only 0.2 inch apart. This is much smaller than the geometrical shear layer thickness (≈.8") which is indicated by the hot-wire results. Apparently, convection speeds can be resolved inside a correlated volume by moving the intersection point.

V. REMOTE SENSING FROM LOW AND HIGH EARTH ORBITS

The concept of remote sensing through cross correlation of optical signals is not restricted by scale and the method should, at least in principle, work also over atmospheric distances. Mounting the two photodetectors on satellites instead of on the ground or on airplanes has the advantages of a larger field of view, quicker scanning, and avoiding vibration problems. In addition to these benefits, which were discussed during the recent remote sensing symposium, the satellite detector can use reflected sunlight, whereas the ground detector is restricted to scattered sunlight. The orbital detector can thus use absorption spectroscopy for a detailed study of atmospheric and ionospheric constituents, whereas the ground detector is restricted to refractive index fluctuations, the interpretation of which is very difficult.

Sometimes the fluctuations of atmospheric constituents may be detectable with the radiative power, which is provided by reflected and scattered sunlight or by emission inside the detector's field of view. In such a case, the optical hardware which would be needed for the crossed beam method is quite similar to that which is developed for the photographic surveys of the earth and the moon. Both applications require a diffraction-limited telescope coupled with an optical filter which selects the ultraviolet, visible, and infrared regions of the spectrum. The main difference consists in replacing the camera with a sensitive phototube and to fly two satellites instead of one.

Two orbital detectors could adjust their lines of sight to intersect on an atmosphere-fixed spot, by continuously turning the telescope during the fly-by. Remote sensing of disturbances around the intersection might be feasible for both the lower and the upper atmosphere. Typical lines of sight are sketched on Figure 9.

To study the feasibility of remote sensing in the lower atmosphere with respect to the following AAP experiments, we suggest:

1. The generation and motion of the aurora and airglow using emitted radiation during the night cycle.

2. The motion or generation of water vapor, pollutants, and trace constituents using reflected sunlight (Fig. 9) or the thermal radiation.

Remote sensing in the upper atmosphere is intriguing, if the use of ground beacons can be avoided. The optical path between the upper atmosphere and the orbital telescope is then short. Also, oxygen has extremely high absorption peaks in the ultraviolet, such that the motion of very diluted oxygen might still be detectable. To study the feasibility of remote sensing the upper atmosphere and ionosphere with re-

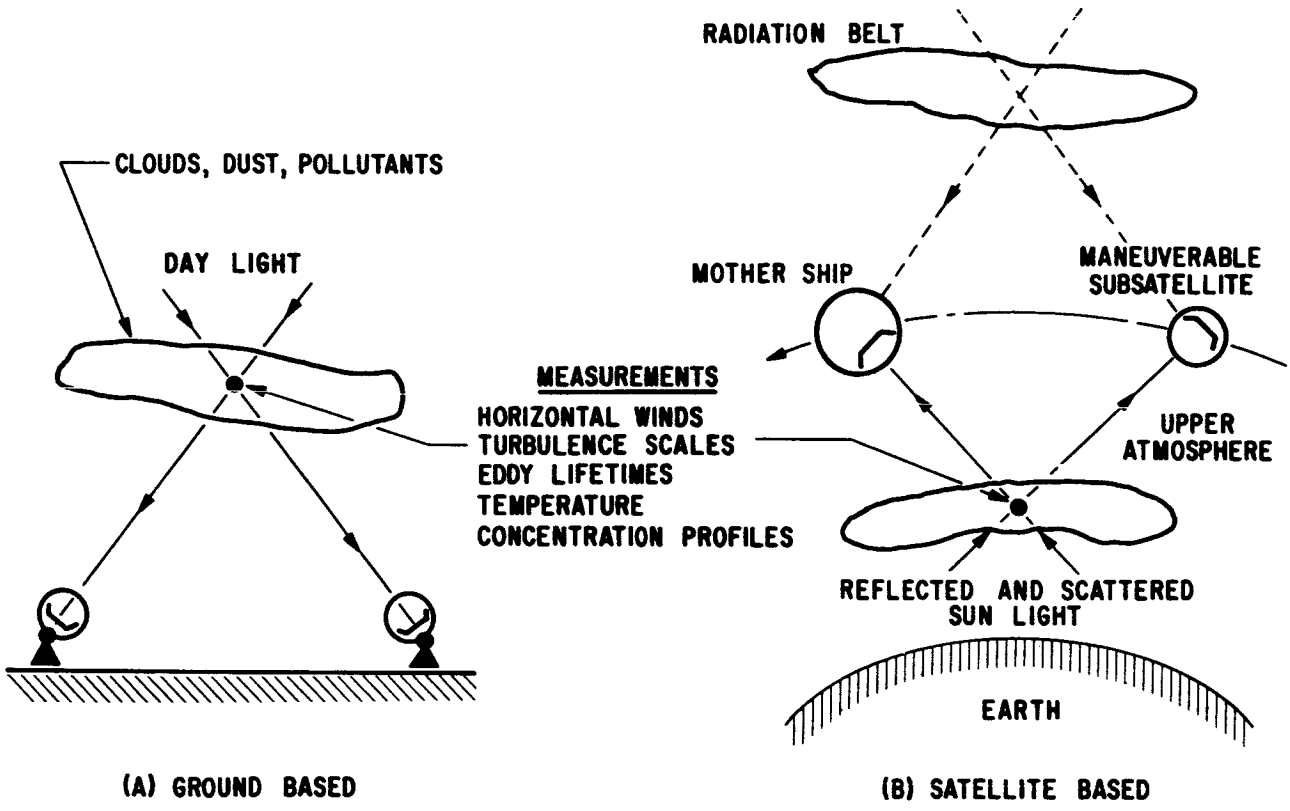

(C) GROUND AND SATELLITE BASED

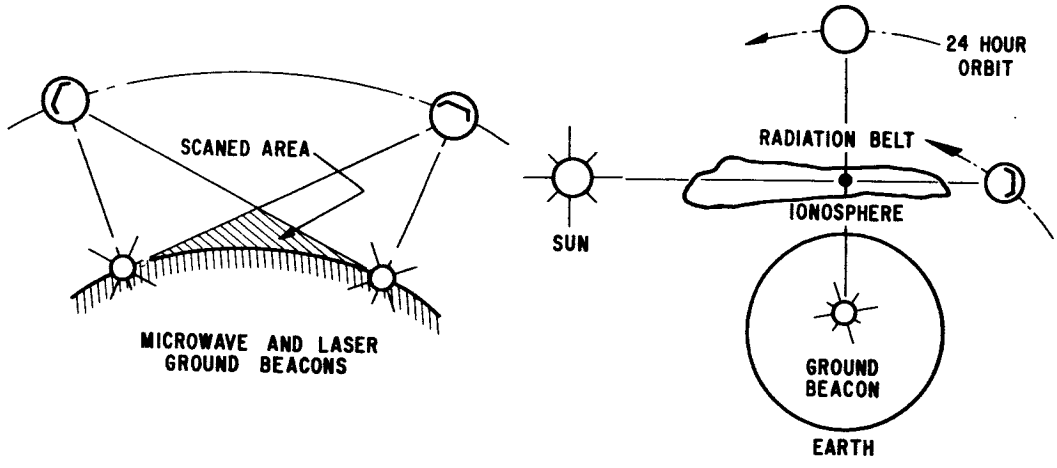

- THE METHOD CAN USE THE WHOLE ELECTROMAGNETIC SPECTRUM FROM X RAYS TO MICROWAVES
- NATURAL RADIATION AND SUN LIGHT MAY REPLACE MICROWAVE AND OPTICAL BEACONS
- A WIDE CLASS OF TEST ARRANGEMENTS IS PROVIDED BY COMBINING GROUND AND ORBITING STATIONS

FIGURE 9. HOW CAN THE CROSSED BEAM METHOD BE APPLIED IN THE ATMOSPHERE?

spect to the following AAP experiments, we suggest:

1. The motion or generation of ozone using direct or scattered sunlight (Fig. 9b).

2. The motion or generation of radiation belts using the emitted electromagnetic radiation. Both vertical and horizontal motions might be studied using the same arrangement sketched for the upper atmosphere (Fig. 9b).

VI. PROBLEMS

The main problems with the crossed beam method are as follows:

1. To find an atmosphere constituent that produces detectable fluctuations of the integrated signal along accessible lines of sight.

2. To reduce light source fluctuations, shot noise and instrument noise to root mean square levels, which have the same order of magnitude as the integrated signal.

3. To have the lines of sight intersect on an atmosphere-fixed spot for an observation time, which is sufficiently long to pull the local signal out of the integrated signal and the combined light source noise, shot noise and instrument noise.

These problems are formidable, and they may prohibit some of the applications that were outlined in the previous section. However, since we can pick the detected radiation from any region of the electromagnetic spectrum and since the orientation of the lines of sight may be chosen arbitrarily, we believe that there is at least one interesting AAP experiment where the above problems may be overcome through special test arrangements. Such an experiment presents an exciting challenge, since the dynamic behavior of the atmosphere, or radiation belts could be added to the "static" mapping on oceanic, geographic, and atmospheric surveys.

Several facts about atmospheric constituents and optical AAP hardware must be collected before we could decide the feasibility of particular experiments. These facts have been identified in the previous discussions and may be summarized by the following questions:

1. Which constituents of the lower atmosphere, such as clouds, pollutants and trace constituents, produce detectable fluctuations within a response time of 0.1 second along a line of sight which traverses the entire atmosphere?

2. Do the usual constituents of the upper atmosphere and ionosphere such as ozone produce detectable fluctuations along a line of sight which traverses the outer portions of the upper atmosphere?

3. Do reflected or scattered sunlight and/or radiation belts put enough radiative power into the orbital detector's field of view to reduce the shot noise below the expected signal levels, considering the telescopes and optical filters which are developed for other AAP missions?

4. Does the continuous motion of the detector's field of view lead to fluctuations of the reflected sunlight that are comparable to the signal fluctuations?

5. For which observation time is it possible to have the narrow fields of view intersect at a point on the lower and the higher atmosphere and what are the beam diameters and pointing accuracies?

6. Is it possible to extend these applications to the complete day and night cycle by using ground beacons besides reflected and scattered sunlight?

REFERENCES

1. Fisher, M. J., and Krause, F.: Local Measurements in Turbulent Flows through Cross-Correlation of Turbulent Fluctuations. NASA TM X-53295, 1 April 1965.

2. Fisher, M. J., and Black, T. H.: Optical Measurements with High Temporal and Spatial Resolution. IITRI Progress Report M6114-18, Contract NAS8-11258, December 1965.

3. Nestor, O. H., and Olsen, H. N.: SIAM Rev. 2,200, 1960.

4. Freeman, M. P. and Katz, S.: J. Opt. Soc. Am. 50,826, 1960.

5. Bockasten, K.: J. Opt. Soc. Am. 51,943, 1961.

6. Barr, W. L.: J. Opt. Soc. Am. 52,885, 1962.

7. Herlitz, S. I.: Arkiv Vysik 23, 571, 1963.

8. Paquette, D. R. and Wiese, W. L.: Appl. Opt. 3, 291, 1964.

9. Howard, J. N., Burch, D. E., and Williams, D.: J. Opt. Soc. Am. 46, 186, 237, 242, 334, 452, 1956.

10. Burch, D. E., and Williams, D.: Appl. Opt. 1, 473, 1962.

11. Burch, D. E., Gryvnak, D., Singleton, E. B., France, W. L., and Williams, D.: Air Force Cambridge Research Labs., Report AFCRL-62-698, 1962.

12. Edwards, D. K.: J. Opt. Soc. Am. 50, 617, 1960.

13. Plass, G. N.: J. Opt. Soc. Am. 48, 690, 1958.

14. Plass, G. N.: J. Opt. Soc. Am. 50, 868, 1960.

15. Plass, G. N.: J. Opt. Soc. Am. 49, 821, 1959.

16. Tourin, H. and Krakow, B.: Appl. Opt. 4, 237, 1965.

17. Krause, F. R., and Fisher, M. J.: Optical Integration over Correlation Areas in Turbulent Flows. Fifth International Congress on Acoustics, Paper K65, Liége, Belgium, September 7-14, 1965.

18. The Vibration Manual. NASA, Geo. C. Marshall Space Flight Center, 1st ed., 1964.

19. Davies, P. O. A. L., Fisher, M. J., and Barrat, M. T., J. Fluid Mech., Vol. 15, pp. 337-367.

20. Davies, P. O. A. L., Near-Field Generation by Intense Turbulence. 5th International Congress of Acoustics, Liége, Belgium, paper L53.

APPLICATION OF THE Q-BALL ANGLE OF ATTACK TRANSDUCER TO LARGE SPACE VEHICLES

By

Paul E. Ramsey

SUMMARY

The angle of attack of large space vehicles can be measured either indirectly or directly. Indirect methods consist of using accelerometers or obtaining rawinsonde wind data, which are used in conjunction with telemetered attitude angles and control parameters to calculate the angle of attack. Direct methods, which tend to be the most accurate, consist of using externally mounted angle of attack sensors. Early direct methods consisted of "weather cock" stable vanes of various types and gimbaled bodies, with and without wings, which were boom-mounted on the nose of the vehicle. Later, stable vane configurations and slotted, self-servoed, cylindrical probes were extended perpendicularly from the vehicle skin. These devices were limited in accuracy, sensitivity, and use because of their electromechanical nature, fragility, external mounting positions, and mode of operation.

The Q-ball was developed to eliminate or reduce the severity of these limitations normally associated with the earlier angle of attack meters. Since the Q-ball is faired into the nose of the vehicle, the strict requirements for surface smoothness ahead of the sensor and local upwash calibrations do not exist. Also, since the Q-ball is not a fragile, protruding device, it is not likely to sustain damage during vehicle ground handling. The accuracy and sensitivity of the Q-ball are enhanced because its principle of operation requires no mechanical moving parts; rather it uses sensitive pressure transducers and associated tubing and electronics.

The Q-ball provides a valuable method for determining the angle of attack of any space vehicle during most of the atmospheric portion of flight. Because of its accuracy and ability to detect slow angular divergence rates away from normal flight angle of attack, the Q-ball has been used to obtain data for post-flight analysis and is being developed for use in the manned Apollo-Saturn emergency detection system to detect abort situations.

LIST OF SYMBOLS

Symbol	Definition
M	Free stream Mach number
q	Free stream dynamic pressure, psia
P	Pressure, psia
α	Angle of attack, degrees
θ	Angle measured from stagnation point on the spherical nose, degrees
ψ	Angle of yaw, degrees
ΔP_α	Pressure differential measured across the pair of 45° ports in the pitch plane, psia
ΔP_ψ	Pressure differential measured across the pair of 45° ports in the yaw plane, psia
ΔP_q	Pressure differential measured across the Q-ports, psia
$\frac{\partial}{\partial\alpha}\left(\frac{\Delta P_\alpha}{q}\right)$ or $\frac{\Delta P_\alpha}{\alpha\, q}$	Slope of $\frac{\Delta P_\alpha}{q}$ versus α curves at $\alpha = 0°$; $\frac{1}{\text{deg.}}$
K	$\frac{\Delta P_q}{\Delta P_\alpha}\alpha$
$C_{p_{max}}$	Pressure coefficient at stagnation point
Subscripts	
θ	Measured at angle θ

LIST OF SYMBOLS (Concluded)

Symbol	Definition
∞	Free stream conditions
1	Upper α port
2	Lower α port
39	Q-port located 39° from Q-ball center line
51	Q-port located 51° from Q-ball center line

I. INTRODUCTION

The control systems of today's advanced space vehicles are a relatively complex organization of vehicle attitude sensors, electronic computers, and actuators needed for movement of a portion of the vehicle, such as a fin, an engine, or a control surface. The major function of such a system is to keep the space vehicle on a prescribed path as closely as possible. An equally important function for the control system, especially for large slender Saturn vehicles, is to keep lateral aerodynamic loads within the failure limits of the vehicle's structure. Since these loads are proportional to the angle of attack and the flight dynamic pressure, the allowable angle of attack must be restricted, especially during the high dynamic pressure regions of flight. Also, since the Saturn vehicles are generally aerodynamically unstable throughout most of the flight range, the control system must induce artificial stability. These control system functions are normally accomplished through some means of engine thrust vector control.

To determine the amount of thrust vectoring needed, the vehicle attitude and angle of attack or accelerations caused by angle of attack induced forces must be known at all times during flight. An exception would be the attitude control system presently planned for Saturn V which will not require angle of attack inputs. This information is fed into a control computer which determines the required engine deflection according to predetermined gain factors. The attitude or vehicle orientation with respect to the vertical can be determined by measuring the angle between the axis of a space-fixed gyrostabilized platform and the vehicle centerline. Angle of attack is normally measured during flight, either directly or indirectly, by any one of various means.

Direct methods, which tend to be the most accurate, use externally mounted angle of attack meters; indirect methods use accelerometers or rawinsonde wind data along with telemetered attitude angles and control parameters to calculate the angle of attack. In the past, several types of angle of attack meters have been used. Early devices consisted of "weather cock" stable configurations which were mounted on the nose of the vehicle and aligned themselves with the direction of the winds. Boom-mounted vanes and gimbaled bodies with and without wings were the most common examples. Later devices consisted of stable vane configurations and slotted, self-servoed, cylindrical probes which were extended perpendicularly from the vehicle skin into the flow field around the vehicle.

All of these devices had limitations characteristic of their mode of operation. Some of these limitations are discussed below:

a. Local body-mounted probe and vane sensors require an accurate calibration of the upwash around the vehicle in the vicinity of the angle of attack sensor for each sensor-vehicle combination.

b. The surface ahead of body-mounted sensors must be free of protuberances or sudden discontinuities which could cause unpredictable local flow conditions.

c. Because local body-mounted sensors are electromechanical devices, good sensitivity and accuracy are limited to relatively high dynamic pressure regions of flight where the aerodynamic forces are sufficient to overcome bearing friction and the momentum of mechanical parts.

d. Because these angle of attack devices are usually fragile and are mounted externally, they can be easily damaged during ground handling, and are subjected to aerodynamic heating during the ascent and reentry phases of flight.

To eliminate or reduce the severity of these limitations, a more advanced sensor for use on large space vehicles was developed by adapting the movable nose sphere Q-ball used on the X-15 research aircraft. The result was a fixed-sphere Q-ball which indicated the angle of attack by sensing differential pressures on the nose sphere. The Q-ball was designed to be incorporated into the nose cones of ballistic missiles (without disturbing the overall vehicle aerodynamic characteristics) and to be sturdy enough to withstand aerodynamic heating during the ascent and to remain essentially intact, even

though inoperative, when exposed to the heat of atmospheric reentry.

During the development period of the Q-ball, angle of attack devices gave way to accelerometers for control purposes, but were and still are required for other applications. Because of an accuracy advantage over accelerometers, angle of attack meters (such as the Q-ball) are used to measure precisely the angle of attack during flight. This information is telemetered back to Earth for postflight analysis of vehicle performance. A Q-ball is now being developed for use as part of an abort warning system for the manned Apollo-Saturn flights. In this capacity, the Q-ball can detect slow divergence from normal flight angles of attack toward the abort limit more accurately than accelerometers.

This paper is concerned with the Q-ball and its application to large space vehicles, and with the major problems and sensor accuracies encountered during actual use.

II. DESCRIPTION AND OPERATION OF Q-BALL

The standard Q-ball is a spherically blunted 15° half-angle cone with diametrically opposite differential pressure orifices which are located 45° from the stagnation point in both the pitch and yaw planes. A pair of differential pressure orifices, called Q-ports, are located 39° and 51° from the stagnation point in a plane rolled 45° from the pitch plane. Figure 1 shows the Q-ball configuration and location of the three pairs of pressure ports.

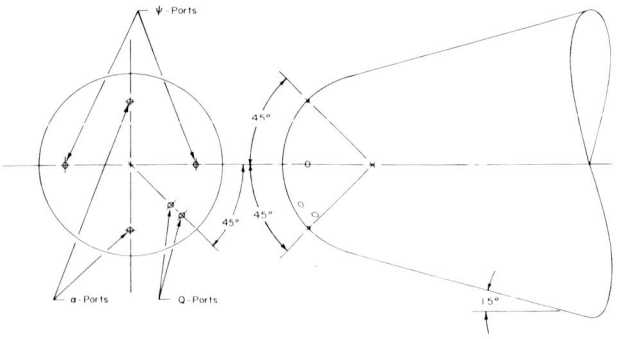

FIGURE 1. PORT CONFIGURATION OF Q-BALL

The Q-ball works on the principle that a linear function exists between the differential pressures measured across the 45° (α and ψ) ports and the angles of pitch and yaw. Because the Q-ball is axisymmetrical, this pressure-to-angle relationship can be represented by a single set of calibration data for both the pitch and yaw planes. Therefore, for simplicity, all further comments will be restricted to the pitch plane. Calibration data are obtained experimentally by placing a scale model of the Q-ball into a wind tunnel (Fig. 2) and measuring the resulting ΔP_α as a function of α. Since the differential pressure variation with α is linear for angles of attack up to approximately 15°, the data are conveniently presented as the slope of the $\Delta P_\alpha/q$ versus α curves or $\Delta P_\alpha/\alpha q$ as a function of free stream Mach number. Typical data are presented in Figures 3 and 4 for several Q-ball sizes and configurations. More complete data are shown by Mills and Lukesh [1] and Ramsey [2]. Also, for comparison, suppersonic experimental data for hemisphere-cylinders, along with some subsonic perturbation theory [3] and modified Newtonian Theory, are presented in Figure 4.

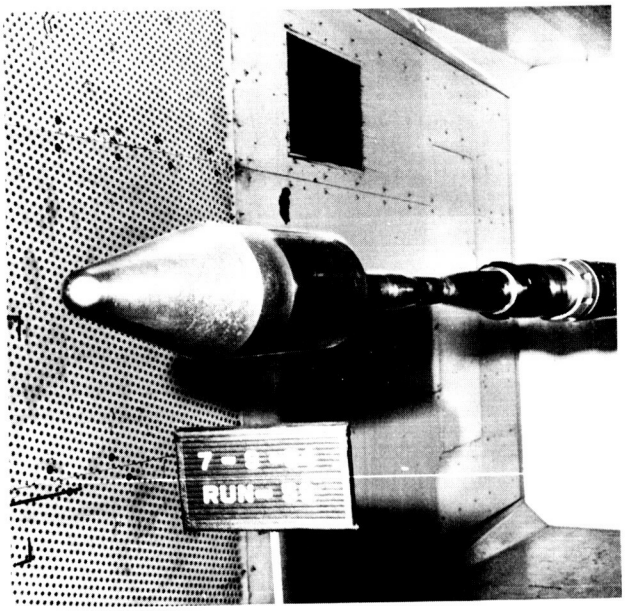

FIGURE 2. TYPICAL LARGE SCALE Q-BALL EXPERIMENTAL MODEL SHOWN INSTALLED IN THE CORNELL AERONAUTICAL LABORATORY 8-FOOT TRANSONIC WIND TUNNEL

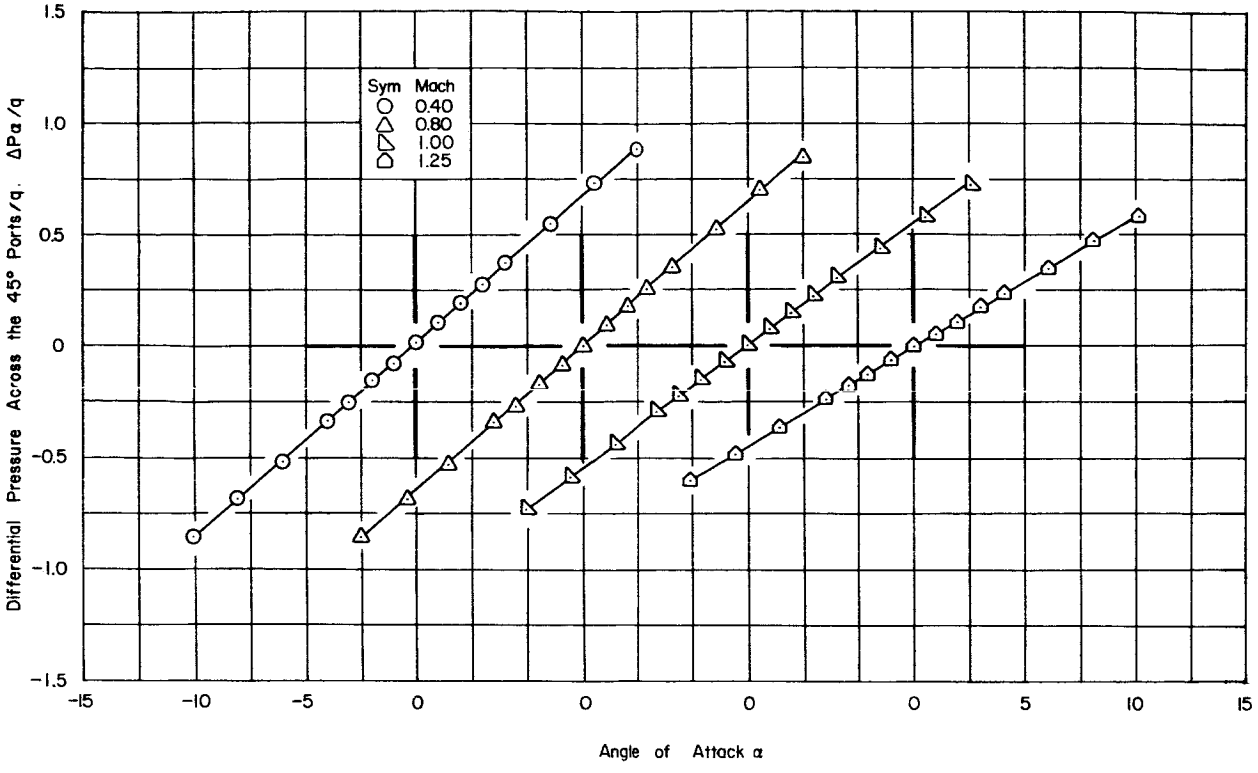

FIGURE 3. VARIATION OF DIFFERENTIAL PRESSURE ACROSS THE 45° PORTS/q WITH ANGLE OF ATTACK

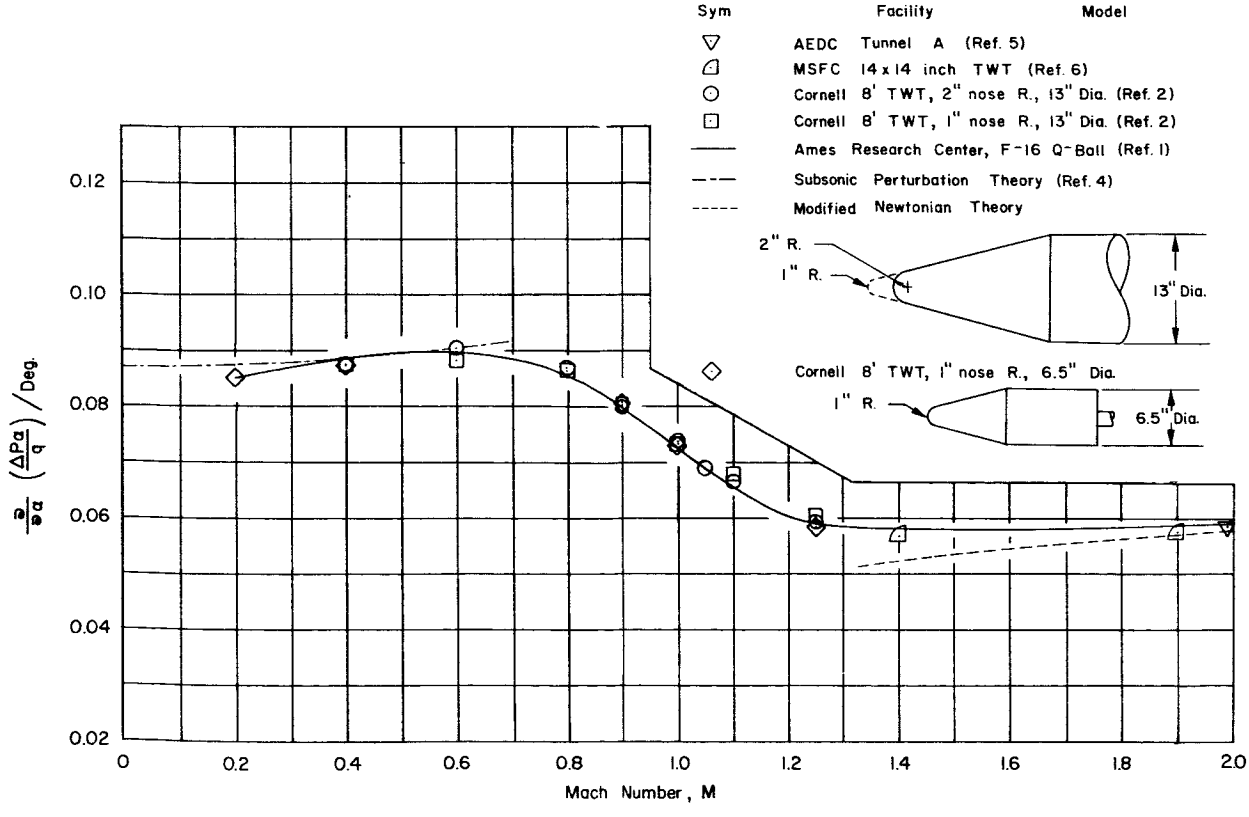

FIGURE 4. SLOPE OF DIFFERENTIAL PRESSURE ACROSS α-PORTS/q VERSUS α CURVES AS A FUNCTION OF FREE STREAM MACH NUMBER

The modified Newtonian data were obtained by using the familiar Newtonian expression to write the equation for the pressure at each of the α-ports and combining them to obtain $\frac{\partial}{\partial \alpha}\left(\frac{\Delta P_\alpha}{q}\right)$ for the pitch plane. Mills and Lukesh [1] give a complete derivation which includes the effects of yaw.

The pressure on a sphere at any point $\theta°$ from the stagnation point is as follows:

$$P_\theta = P_\infty + C_{p_{max}} q \cos^2 \theta .$$

At some angle of attack (α), the θ angles for ports 1 and 2, shown in Figure 5, are as follows:

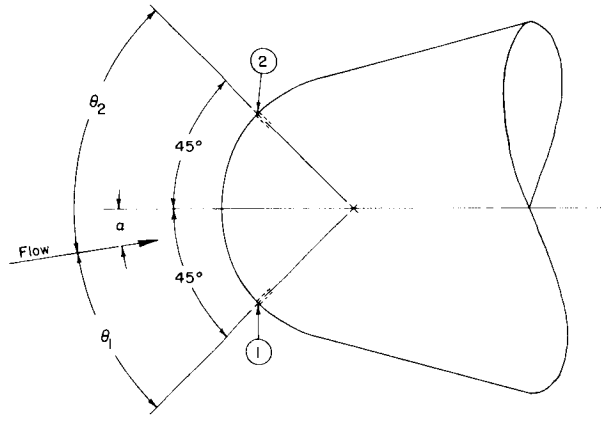

FIGURE 5. NOTATION FOR PRESSURE CALCULATIONS WITH Q-BALL AT AN ANGLE OF ATTACK

$$\theta_1 = \frac{\pi}{4} - \alpha$$

$$\theta_2 = \frac{\pi}{4} + \alpha .$$

Therefore,

$$P_1 = P_\infty + C_{p_{max}} q \cos^2 \theta_1 \qquad (1)$$

$$P_2 = P_\infty + C_{p_{max}} q \cos^2 \theta_2 . \qquad (2)$$

Subtraction of Equations (1) and (2) and substituting the expressions for θ_1 and θ_2 yields

$$\frac{P_1 - P_2}{q} = C_{p_{max}} \cos^2 \theta_1 - C_{p_{max}} \cos^2 \theta_2$$

$$\frac{\Delta P_\alpha}{q} = C_{p_{max}} \left[\cos^2 \left(\frac{\pi}{4} - \alpha\right) - \cos^2 \left(\frac{\pi}{4} + \alpha\right)\right] . \qquad (3)$$

Now, we have

$$\cos \left(\frac{\pi}{4} - \alpha\right) = \cos \frac{\pi}{4} \cos \alpha + \sin \frac{\pi}{4} \sin \alpha$$

and

$$\cos \frac{\pi}{4} = \sin \frac{\pi}{4} .$$

Substituting we get

$$\cos \left(\frac{\pi}{4} - \alpha\right) = \sin \frac{\pi}{4} (\cos \alpha + \sin \alpha).$$

Therefore,

$$\cos^2 \left(\frac{\pi}{4} - \alpha\right) = \sin^2 \frac{\pi}{4} (\cos^2 \alpha + 2 \sin \alpha \cos \alpha + \sin^2 \alpha)$$

$$\cos^2 \left(\frac{\pi}{4} + \alpha\right) = \sin^2 \frac{\pi}{4} (\cos^2 \alpha - 2 \sin \alpha \cos \alpha + \sin^2 \alpha).$$

Substitution in Equation (3) yields

$$\frac{\Delta P_\alpha}{q} = C_{p_{max}} \sin^2 \frac{\pi}{4} (4 \sin \alpha \cos \alpha)$$

$$\frac{\Delta P_\alpha}{q} = C_{p_{max}} \sin 2\alpha .$$

Differentiating, we obtain

$$\frac{\partial}{\partial \alpha}\left(\frac{\Delta P_\alpha}{q}\right) = 2 C_{p_{max}} \cos 2\alpha . \qquad (4)$$

Equation (4), which determines $\frac{\partial}{\partial \alpha}\left(\frac{\Delta P_\alpha}{q}\right)$ in radian measure $\left(\frac{1}{\text{rad}}\right)$, was converted to degrees before being presented in Figure 4.

The Q-ball measured differential pressures are also a function of the dynamic pressure level; consequently, a means of determining the dynamic pressure

is necessary, which is the function of the Q-ports. Differential pressures measured across these ports are directly related to free stream dynamic pressure. Necessary calibration data are normally presented as the differential pressure across the Q-ports, ΔP_q, ratioed to free stream dynamic pressure, q, or simply $\Delta P_q/q$ as a function of Mach number. Typical ΔP_q calibration data are presented in Figure 6 for several Q-ball configurations. Some hemisphere-cylinder data, along with subsonic perturbation and Newtonian theories, are also presented for comparison with the ΔP_q calibration data.

The $\Delta P_q/q$ and $\Delta P_\alpha/\alpha q$ data can be combined to obtain the flight angle of pitch, α, in the following manner. First, for any Mach number, $\Delta P_\alpha/\alpha q$ and the corresponding $\Delta P_q/q$ value can be used to determine a K factor (represented by λ [4]) as follows:

$$K = \frac{(\Delta P_q/q)}{\Delta P_\alpha/\alpha q} = \frac{\Delta P_q}{\Delta P_\alpha}\,\alpha \quad . \tag{5}$$

Then, to obtain the vehicle angle of pitch, the flight-measured ΔP_α and ΔP_q are ratioed and multiplied by K as follows:

$$\alpha = K\left(\frac{\Delta P_\alpha}{\Delta P_q}\right)_{\text{measured in flight}} \quad . \tag{6}$$

III. Q-BALL TYPES

There are three versions of the Q-ball either in existence or under development. The Q-ball principle was used on early Saturn vehicles by measuring differential pressures across pairs of holes drilled into the nose cone. A complete Q-ball package known as the F-16 was flown on Saturn SA-4 through SA-7 vehicles. This is a normal Q-ball which has a 2-inch

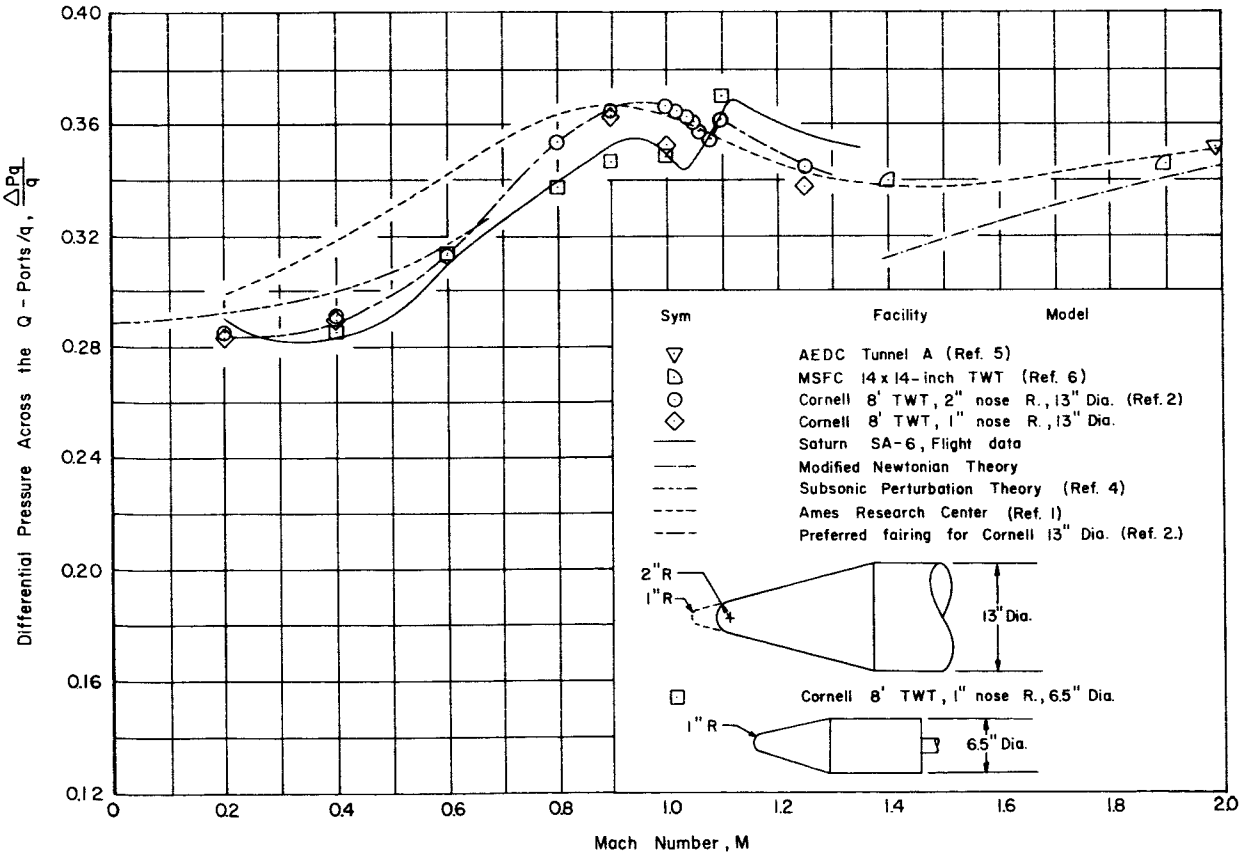

FIGURE 6. THE DIFFERENTIAL PRESSURE ACROSS THE Q-PORTS/q AS A FUNCTION OF FREE STREAM MACH NUMBER FOR ZERO ANGLE OF ATTACK

nose radius and was used with the q-measurement as explained above.

The measuring Q-ball, a second highly refined version now being developed at MSFC, has a nose radius of 4 inches and operates on the same principle as the F-16 model, but uses six pressure transducers instead of three. This arrangement provides a low and high range transducer for each of the three differential pressure measurements (ΔP_α, ΔP_ψ, and ΔP_q). The extra set of transducers extends the range of this Q-ball to cover a larger portion of the vehicle flight period. Flown on Saturn I vehicles SA-8, SA-9, and SA-10, this version will be used on future vehicles requiring angle of attack measurements.

The third Q-ball, which is presently of greatest interest, is the emergency detection system (EDS) Q-ball being developed for the manned Apollo-Saturn flights. This device has a 4-inch nose radius and only α and ψ ports. Since the differential pressures are a function of both the vehicle angular attitude and dynamic pressure, they are an effective indication of the aerodynamic loads on the vehicle. During flight, the vector sum of ΔP_α and ΔP_ψ will be displayed to the astronaut. Should this sum go beyond a set limit or "red line" and if the astronaut has confirmation from other EDS sources, he may initiate manual abort. The "red line" will be based on vehicle structural limits, trajectory data, and Q-ball calibration data.

IV. CALIBRATION PROBLEMS AND Q-BALL LIMITATIONS

The existing experimental evidence indicates that the ΔP_α measurements are relatively unaffected by afterbody configuration, scaling effects, or slight hardware inaccuracies due to manufacturing tolerances. On the other hand, because of the disagreement between data obtained from various experimental test models and flight Q-balls, the ΔP_q measurement appears to be very sensitive to these same parameters. This is indicated in Figure 6. A natural consequence is that any ΔP_q measurements obtained experimentally will have a limited accuracy because the full scale flight hardware and flight aerodynamic parameters cannot be exactly simulated.

During the present discussion, the $\Delta P_q/q$ calibration curves have been conveniently assumed to be constant with variations in α, but an examination of the typical $\Delta P_q/q$ versus α data, obtained from Ramsey [2] and presented in Figure 7, indicates that there are significant effects which must be considered when the Q-ball is used. In effect, this reduces the precision of the angle of pitch as computed from Equations (5) and (6). To obtain an accurate α, a second $\Delta P_q/q$ value, which corresponds to the first computed α, must be obtained from data similar to that in Figure 7 and used to calculate a new K factor. This K can then be used to compute a new α which is used to start the entire process again. This iteration should be made at least three times to obtain the necessary accuracy.

The $\Delta P_q/q$ nonlinear variation with α apparently is caused by the location of the Q-ports in the plane rotated 45° from the pitch plane. By using spherical geometry to derive expressions for the angular distances of the Q-ports from the stagnation point and using the Newtonian expression for the pressure distribution, an equation that describes $\Delta P_q/q$ for various angles of attack can be derived as follows.

Figure 8 indicates the geometry involved in computing θ for the Q-ports. For the 39° port,

$$\sin b = \sin B \sin c \tag{7}$$

$$\tan a = \frac{\cos B}{\operatorname{ctn} c} \quad \text{and} \quad \frac{1}{\operatorname{ctn} c} = \tan c.$$

Therefore,

$$\tan a = \cos B \tan c. \tag{8}$$

Equations (7) and (8) become

$$\sin b = \sin 45° \sin 39° \tag{9}$$

$$\tan a = \cos 45° \tan 39° \tag{10}$$

Now, since we have a right spherical triangle,

$$\cos \theta_{39} = \cos (a - \alpha) \cos b. \tag{11}$$

Solving Equations (9) and (10) and substituting into Equation (11), we obtain

$$\cos \theta_{39} = 0.8956 \cos (29.80 - \alpha). \tag{12}$$

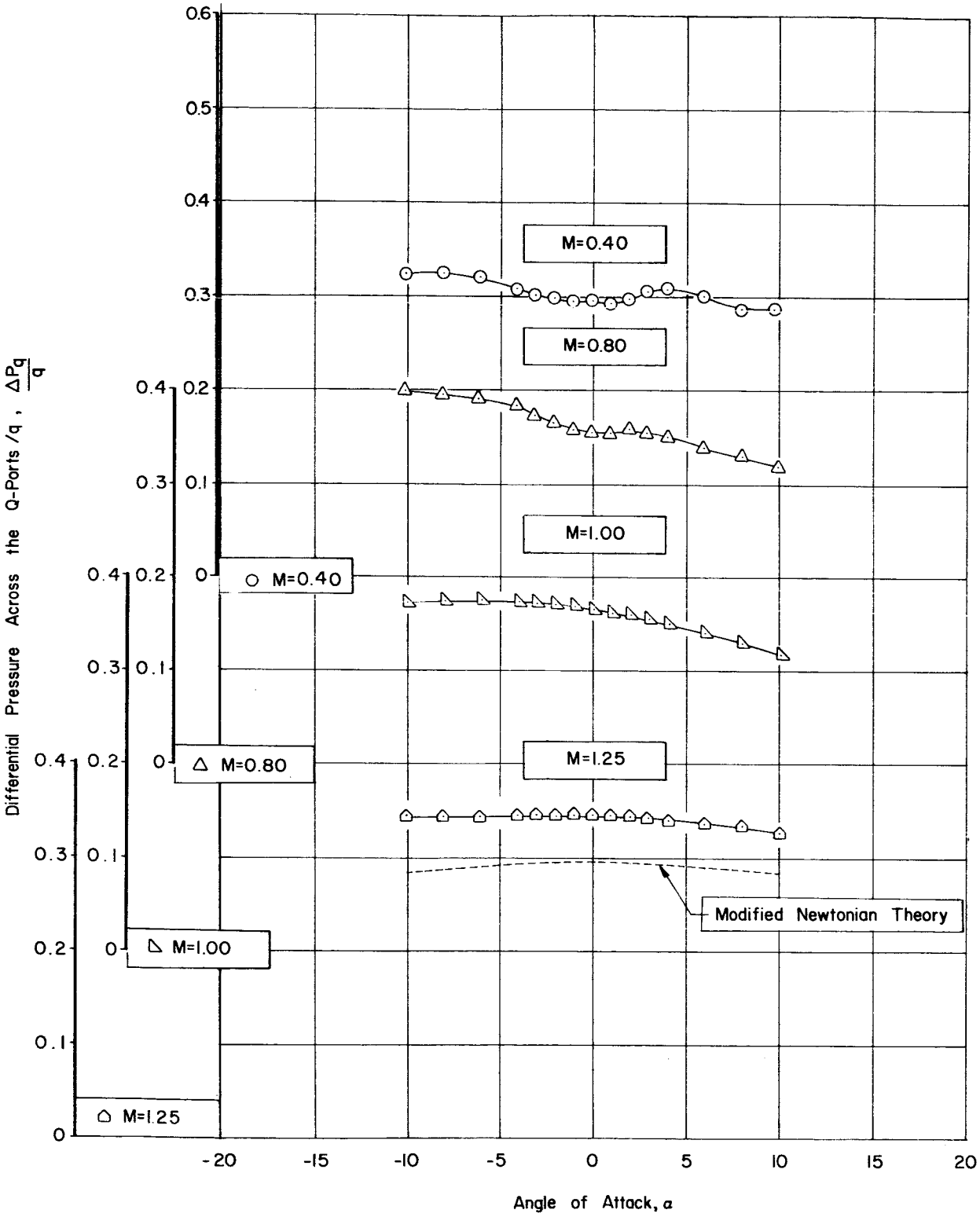

FIGURE 7. VARIATION OF DIFFERENTIAL PRESSURE ACROSS THE Q-PORTS/q WITH ANGLE OF ATTACK FOR SEVERAL MACH NUMBERS

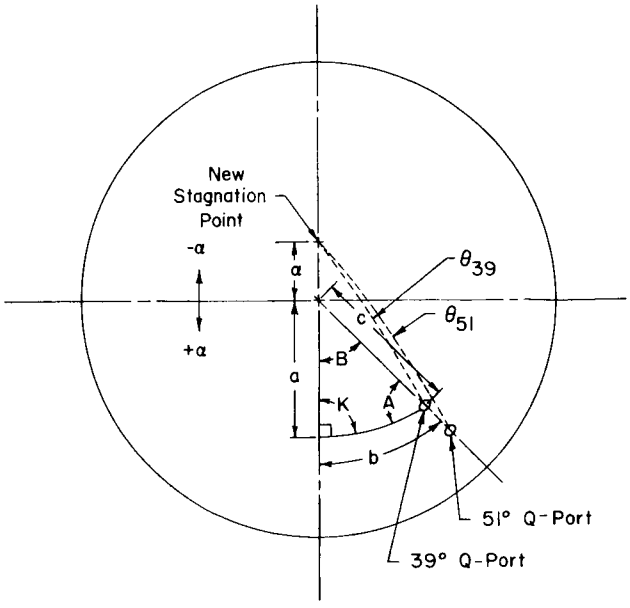

FIGURE 8. THE RELATIONSHIP BETWEEN THE Q-PORTS AND THE STAGNATION POINT AT ANGLE OF ATTACK

Similarly,

$$\cos \theta_{51} = 0.8355 \cos (41.13 - \alpha). \quad (13)$$

The Newtonian expressions for the two Q-ports are

$$P_{\theta_{39}} = P_\infty + C_{p_{max}} q \cos^2 \theta_{39} \quad (14)$$

$$P_{\theta_{51}} = P_\infty + C_{p_{max}} q \cos^2 \theta_{51}. \quad (15)$$

Rearranging and subtracting Equations (14) and (15), we obtain

$$\frac{\Delta P_q}{q} = C_{p_{max}} (\cos^2 \theta_{39} - \cos^2 \theta_{51}). \quad (16)$$

Squaring Equations (12) and (13) and substituting into Equation (16) yields

$$\frac{\Delta P_q}{q} = C_{p_{max}} [\cos^2 (29.80 - \alpha)\, 0.8019 - \cos^2 (41.13 - \alpha)\, 0.6981]. \quad (17)$$

Data obtained from Equation (17) are presented in Figure 7 for angles of attack between ± 10° and a Mach number of 1.25.

Because the theory is less valid for low supersonic Mach numbers, the modified Newtonian values are lower than the experimental data, but the nonlinear trends are similar. The locations of the Q-ports cause the distance between each of the two ports and the stagnation point to vary differently with changing α as is shown in Figure 8. Since the pressures sensed by these ports are a function of the distance from the stagnation point, the measured ΔP_q will be nonlinear with α. The difference between the two $\cos^2 \theta$ terms in Equation (17) represents this conclusion.

Because of these limitations of the dynamic pressure measurement, it is sometimes desirable to use the Q-ball without the ΔP_q measurement and instead to rely on the dynamic pressure obtained from other sources such as some type of on-board pilot-static probe or calculation from the telemetered trajectory parameters. The source which is used to obtain the dynamic pressure measurement should be determined by whether the Q-ball is used as a measurement instrument or as a control input. For instance, if the Q-ball were being used as a measurement device, immediate on-board dynamic pressure information would not be necessary since all data would be telemetered back to Earth for postflight analyses.

A rigid mounting must be provided for the Q-ball to prevent errors caused by flexing of the mounting structure. Also, the vehicle configuration should provide for a nose-mounting position for the Q-ball to ensure that the sensor will be located in relatively undisturbed free stream flow.

V. ESTIMATED Q-BALL ERRORS

The probable errors for the Q-ball are dependent not only on the accuracy of the angular pressure measurements (ΔP_α and ΔP_ψ), but on whether the dynamic pressure measurement is used. The 99.73 percent probability errors for a normal Q-ball using both the angular and dynamic pressure measurements are presented in Figure 9 for a typical Saturn trajectory. These errors would be somewhat less if a more refined externally obtained dynamic pressure were used.

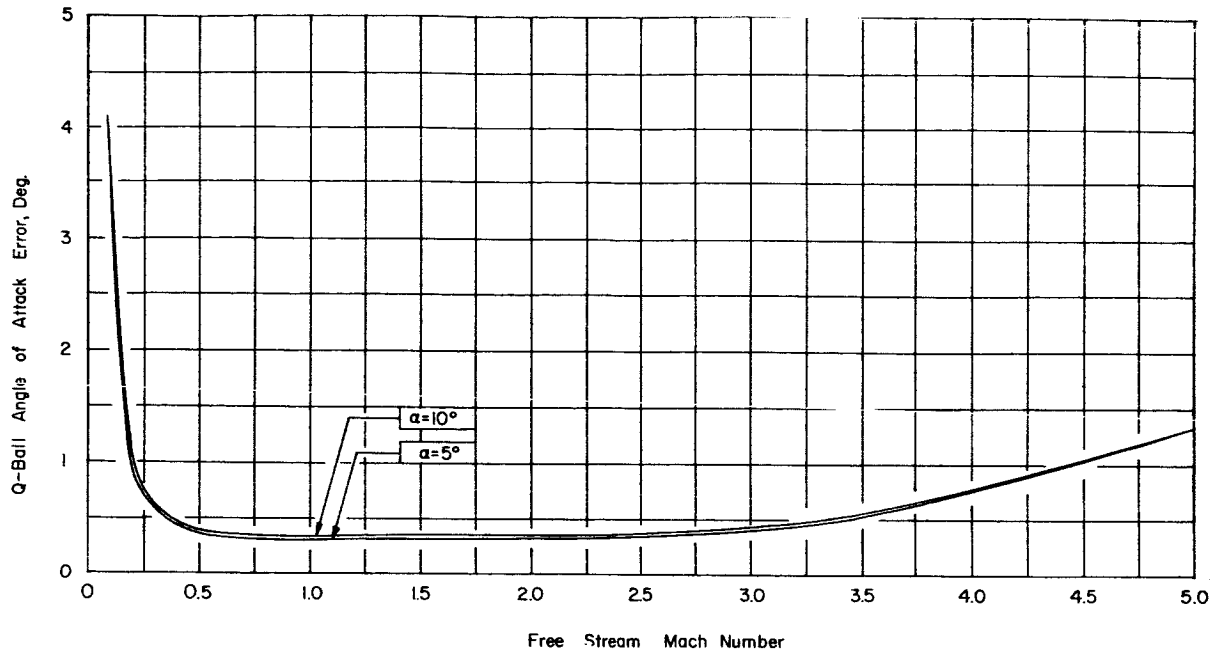

FIGURE 9. THE 99.73 PERCENT PROBABLE ERROR FOR THE Q-BALL DESCRIBED AS A FUNCTION OF MACH NUMBER FOR 5° AND 10° ANGLE OF ATTACK

Other sources which contribute to the errors presented in Figure 5 are listed below.

a. ΔP_{α} measurement error due to the pressure transducer inaccuracies.

b. Manufacturing errors, such as port mislocations for the flight Q-ball and the test models, which introduce inaccuracies in the calibration curves.

c. Slight nonlinearities in the pressure distribution over the spherical nose.

d. Q-ball misalignment with respect to the space vehicle.

e. Vehicle subsonic upwash ahead of the Q-ball transducer. The upwash cannot be completely corrected by wind tunnel calibrations because of the impracticability of placing the complete Q-ball/vehicle combination in a wind tunnel. Calculation of the upwash is impractical because of the range and complexity of possible vehicles on which the Q-ball will be flown.

Since vehicle elastic bending, which causes Q-ball angular misalignment, can be different for various vehicle configurations, it has not been included. In most cases, elastic bending can more than double the expected error in measurement of angle of attack.

Figure 9 indicates that the accuracy of the Q-ball drops off rapidly during the early and latter part of flight because of the relatively low dynamic pressure levels in these regions. The Q-ball differential pressures drop to such low values that they approach the measuring inaccuracies of the pressure transducers used in the Q-ball. The accuracy of all externally mounted angle of attack sensors suffers during these regions of flight, but because of its greater sensitivity, the Q-ball is less affected than the other devices.

VI. COMPARISON WITH ACCURACY OF OTHER METHODS

The relative accuracies of the various methods of measuring the angle of attack are investigated by Addison [4]. Saturn SA-2 through SA-4 flight data from the Q-ball, rawinsonde winds, and accelerometers were compared to a slotted, cylindrical probe sensor, which was used as a reference because, at the time of this study, the probe device

had been flown successfully on a large number of Jupiter missiles and the early Saturns. The probe sensors have limitations, such as a need for an accurate calibration of the upwash field around the vehicle and possible misalignment with the vehicle centerline which can introduce errors. However, if these errors are assumed to be reasonably small, the various methods for determining angle of attack can be evaluated.

The Q-ball data compared favorably with the probe sensor data for most of the vehicles studied; therefore, the Q-ball sensor was considered to be an accurate method for measuring angle of attack.

VII. CONCLUSIONS

The angle of attack of large space vehicles is difficult to measure accurately because of the inevitable limitations of any known technique. Direct methods, i.e., externally mounted angle of attack sensors, are inherently more accurate than indirect methods such as accelerometers and rawinsonde winds.

The limitations of various externally mounted sensors used in the past are summarized as follows:

a. Local body-mounted probe or vane sensors require an accurate calibration of the local upwash around the vehicle for each sensor-vehicle combination.

b. The surface ahead of body-mounted sensors must be smooth and free of structures and protuberances which could cause unpredictable local flow conditions.

c. Bearing friction and momentum of mechanical parts reduce the accuracy, sensitivity, and therefore the range of flight times for which the sensor is useful.

d. Externally mounted sensors are easily damaged during vehicle ground handling and are subjected to aerodynamic heating during ascent and reentry.

The Q-ball was developed to eliminate or reduce the severity of the limitations of the earlier angle of attack meters. Because the Q-ball is faired into the nose ahead of the vehicle itself, the requirements for surface smoothness ahead of the sensor and local upwash calibrations no longer exist. Also, since the Q-ball is not a fragile device which protrudes from the vehicle skin, the sensor is not as likely to sustain damage during ground handling. Although it does not maintain an operational capability, the Q-ball is designed to survive reentry. Accuracy and sensitivity of the Q-ball is enhanced because its principle of operation requires no mechanical moving parts, only sensitive pressure transducers and associated tubing and electronics.

It can be concluded that the Q-ball provides a valuable method for determining angle of attack of any launch vehicle during most of the atmospheric portion of flight, especially the important maximum dynamic pressure region. Because of its accuracy and ability to detect slow angular divergence rates, the Q-ball has been used to obtain data for post-flight analysis and is being developed for emergency detection system purposes.

REFERENCES

1. Mills, G. R. and Lukesh, J. S.: F-16 Q-Ball Pitch and Yaw Transducer Output Characteristics-Summary of Wind Tunnel Test Results. Northrop Corporation, Nortronics Division, Report NORT-63-152, July 1963.

2. Ramsey, Paul E.: Results of the Q-Ball Pressure Distribution Investigations in the Cornell 8-Foot Transonic Wind Tunnel. R-AERO-AD-64-99, November 6, 1964.

3. Struck, H. G.: Analytical Determination of Pressure Distribution on Blunt-Based Bodies of Revolution Under Influence of the Wake at Small Angles of Attack in Subsonic Flow by the Use of Surface Singularities. R-AERO-IN-18-64, July 10, 1964.

4. Addison, W. E.: Angle of Attack Sensor Analysis. Lockheed Missiles and Space Company LMSC/HREC A03348, August 1964.

5. Baer, A. L.: Pressure Distribution on a Hemisphere Cylinder at Supersonic and Hypersonic Mach Numbers. AEDC-TN-61-96, August 1961.

6. Reichle, Henry G., Jr.: Hemisphere-Cylinder Pressure Distributions at Subsonic, Transonic, and Supersonic Mach Numbers. NASA TN D-1570.

IV. ORBIT THEORY AND PREDICTION

A SOLUTION OF A PROBLEM OF ORBIT DETERMINATION WITH POSSIBLE APPLICABILITY TO THE ABORT GUIDANCE PROBLEM

By

Robert J. Hill and William D. Goldsby, Jr.

SUMMARY

This paper presents a closed solution to the problem of orbital determination if two position vectors and the path angle at one of the vectors are given. The orbit thus determined may be considered as having application to the abort guidance problem where an alternate mission might be the alternative to mission failure.

The procedure here developed is available in an operative computer program. A slight modification in the program could allow the user, by varying the specified terminal position vector, to iterate on some final desired geocentric coordinates.

I. INTRODUCTION

Consider a vehicle with a given position vector ($\bar{P}$) and velocity vector ($\bar{V}$) traveling in an isolated central force field. What is the elliptical path which the vehicle must follow so that it will arrive at a desired later position with a prescribed direction of the velocity vector (flight path angle, ϑ)? This is, in effect, a statement of the abort guidance problem, the application of which is assumed in investigating situations in which alternate missions may become necessary.

The problem is solved in closed form by use of some geometrical properties of the ellipse and by use of some standard procedures of celestial mechanics. The approach is first to determine the required path (ellipse) the vehicle must follow, and then to determine the necessary velocity vector needed to transfer the vehicle from its present path to the required ellipse.

II. ANALYSIS

The abort guidance problem is one of insuring that certain specified end points of vehicle position and flight path angle are met after mission abort.

For the purpose of this analysis, this problem statement implies the determination of the required ellipse to meet the specified end point and the velocity increment necessary for the vehicle to transfer to that ellipse.

The adoption of the following notation is convenient for the required analysis:

$\bar{P}_1$ - the position vector of the vehicle at the time the abort is initiated.

$\bar{P}_2$ - the position vector of the vehicle desired at some later time.

$\bar{F}_1$ - the position of the attracting body. The coordinates of $\bar{F}_1$ are taken without loss of generality as the origin

$$F_1 = (0, 0, 0)^T$$

$$\bar{I} = (1,0,0)^T$$

$$\bar{J} = (0,1,0)^T$$

$$\bar{K} = (0,0,1)^T$$

The angle, $\Delta\varphi$, between $\bar{P}_1$ and $\bar{P}_2$ in the plane determined by $\bar{P}_1$ and $\bar{P}_2$ may be computed in the following manner:

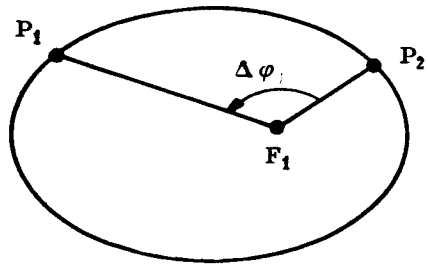

$$\cos \Delta\varphi = \frac{\bar{P}_1 \cdot \bar{P}_2}{|\bar{P}_1|\ |\bar{P}_2|}$$

$$\sin \Delta\varphi = \frac{(\bar{P}_1 \times \bar{P}_2)}{|\bar{P}_1|\ |\bar{P}_2|} \cdot \frac{(\bar{P}_1 \times \bar{P}_2)}{|\bar{P}_1 \times \bar{P}_2|}$$

$$\Delta\varphi = \tan^{-1}\left(\frac{\sin \Delta\varphi}{\cos \Delta\varphi}\right) .$$

Now, let $\bar{F}_2$ denote the position of the other focus and have coordinates (X, Y, Z) to be determined. In order to determine these values, it is convenient to transform the coordinate system so that the X and Y axes lie in the plane of $\bar{P}_1$ and $\bar{P}_2$ and so that the three coordinate axes form a right-handed system. In order to perform this transformation, the following computations are made. Let ζ be the angle measured in the plane of $\bar{P}_1$ and $\bar{P}_2$ from $\bar{P}_1$ to the intersection of the X-Y plane and the plane of $\bar{P}_1$ and $\bar{P}_2$.

The unit vector, $\bar{N}$, in the direction of the descending node is given by

$$\bar{N} = \frac{(\bar{P}_1 \times \bar{P}_2) \times \bar{K}}{|(\bar{P}_1 \times \bar{P}_2) \times \bar{K}|} .$$

The angle ζ is then given by

$$\cos \zeta = \frac{\bar{P}_1 \cdot \bar{N}}{|\bar{P}_1|}$$

$$\sin \zeta = \frac{(\bar{P}_1 \times \bar{N})}{|\bar{P}_1|} \cdot \frac{(\bar{P}_1 \times \bar{N})}{|\bar{P}_1 \times \bar{N}|}$$

$$\zeta = \tan^{-1}\left(\frac{\sin \zeta}{\cos \zeta}\right) .$$

The angle, σ, which is the angle between the line of nodes of the two planes and the X axis, is given by

$$\cos \sigma = \bar{N} \cdot \bar{I}$$

$$\sin \sigma = (\bar{N} \times \bar{I}) \cdot \frac{(\bar{N} \times \bar{I})}{|\bar{N} \times \bar{I}|}$$

$$\sigma = \tan^{-1}\left(\frac{\sin \sigma}{\cos \sigma}\right) .$$

The angle, i, which is the inclination of the plane of $\bar{P}_1$ and $\bar{P}_2$ to the X-Y plane, is given by

$$\cos i = \frac{\bar{P}_1 \times \bar{P}_2}{|\bar{P}_1 \times \bar{P}_2|} \cdot \bar{K}$$

$$\sin i = \frac{(\bar{P}_1 \times \bar{P}_2) \times \bar{K}}{|(\bar{P}_1 \times \bar{P}_2) \times \bar{K}|} \cdot \bar{N}$$

$$i = \tan^{-1}\left(\frac{\sin i}{\cos i}\right) .$$

Now the transformation may be made from the (X, Y, Z) system to the (X', Y', Z') system, where the X axis lies along $\bar{P}_1$ and the Z axis is perpendicular to the plane of $\bar{P}_1$ and $\bar{P}_2$ and the (X, Y, Z) system forms a right-handed system.

$$\bar{X}' = (\sigma)_3\ (i)_1\ (\zeta)_3\ \bar{X}$$

where

$$(\sigma)_3 = \begin{pmatrix} \cos\sigma & \sin\sigma & 0 \\ -\sin\sigma & \cos\sigma & 0 \\ 0 & 0 & 1 \end{pmatrix}, \quad (i)_1 = \begin{pmatrix} 1 & 0 & 0 \\ 0 & \cos i & \sin i \\ 0 & -\sin i & \cos i \end{pmatrix}$$

and

$$(\zeta)_3 = \begin{pmatrix} \cos\zeta & \sin\zeta & 0 \\ -\sin\zeta & \cos\zeta & 0 \\ 0 & 0 & 1 \end{pmatrix} .$$

The transformation takes the vector $\bar{P}_1$ into the vector $\bar{P}_1 = (P_1, 0, 0)$ and the vector $\bar{P}_2$ into the vector $\bar{P}_2 = (|P_2| \cos \Delta\varphi, |P_2| \sin \Delta\varphi, 0)$.

A useful property of an ellipse is now stated. Given the foci, F_1 and F_2, of any ellipse and any point P on an ellipse, then the angle that F_1 P makes with the tangent at P is equal to the angle that F_2 P makes with the tangent at P. This property is essential to the analysis and is proved in the Appendix.

The angle that the vector $\bar{P}^*_1$ makes with the velocity vector is $180 - \vartheta_1$ where ϑ_1 is the path angle at $\bar{P}^*_1$.

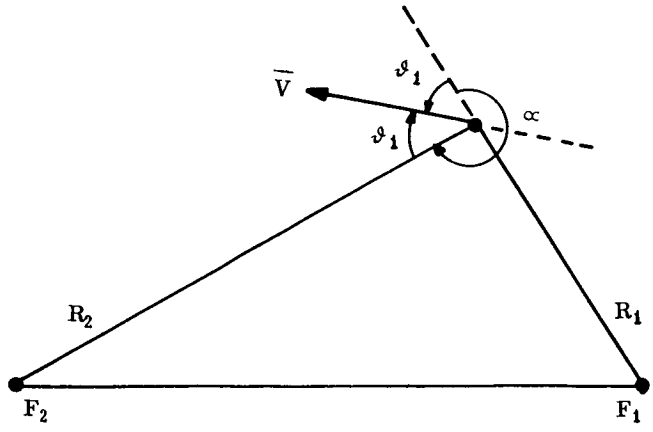

Then the angle, α , between the extension of $\bar{P}_1$ and $\bar{F}_2$ is given by

$$\alpha = 360 - 2\vartheta_1 .$$

If the origin is translated to P'_1 and a rotation through the angle α is performed, the coordinates of F''_2, the double prime denotes the third coordinate system, become (X'', 0, 0). The transformation may be represented in general by

$$\bar{X}'' = (\alpha)_3 (\bar{X}' - \bar{P}'_1) \text{ where}$$

$$(\alpha)_3 = \begin{pmatrix} \cos\alpha & \sin\alpha & 0 \\ -\sin\alpha & \cos\alpha & 0 \\ 0 & 0 & 1 \end{pmatrix} .$$

Another property of the ellipse is shown:

Given any point P on an ellipse and the two foci, then

$$|\bar{F}_1 - \bar{P}| + |\bar{F}_2 - \bar{P}| = \text{Constant.}$$

Using this property yields

$$P_1 + X'' = P_2 + \left[(Y'' - Y''_2)^2 + (X'' - X''_2)^2\right]^{\frac{1}{2}} .$$

But Y'' = 0, Z'' = 0, after the transformation. Solving for X'' results in

$$X'' = \frac{Y''^2_2 + X''^2_2 - (P_1 - P_2)^2}{2(P_1 - P_2 + X''_2)} .$$

Then

$$\bar{X}' = (\alpha)_3^T \bar{X}'' + \bar{P}_1$$

gives the coordinates of F_2. Since F_1 is at the origin, the distance between the foci is given by $|\bar{X}'|$. The distance between P'_1 and F'_2 is given by $|\bar{P}'_2 - \bar{F}'_2|$ and the semi-major axis, a, is given by

$$a = \frac{P_1 + |\bar{P}'_1 - \bar{F}'_2|}{2} .$$

For any ellipse, the distance between the center and either focus is given by $(a^2 - b^2)^{\frac{1}{2}}$ where b is the semi-minor axis. This distance is also given by $\frac{|\bar{X}'|}{2}$ since F'_1 is at the origin.

Hence, $(a^2-b^2)^{\frac{1}{2}} = \frac{|\bar{X}'|}{2}$;

i.e., $b^2 = a^2 - \frac{|\bar{X}'|^2}{4}$.

The numerical eccentricity, e, is given by the relation

$$e = \frac{(a^2-b^2)^{\frac{1}{2}}}{a} \qquad (0 < e < 1).$$

The semilatus rectum, p, is given by

$$p = \frac{b^2}{a} .$$

The angular momentum, h, is given by

$$h = (\mu p)^{\frac{1}{2}} , \quad h > 0 ,$$

where μ is the gravitational constant.

Now, the magnitude of the velocity at $\bar{P}'_2$ is given by

$$V_2 = \left(\frac{2\mu}{P_2} - \frac{\mu}{a}\right)^{\frac{1}{2}} .$$

The unit vector in the direction of peri-center $\bar{U}'$ is is given by

$$U' = -\frac{\bar{X}'}{|\bar{X}'|} .$$

The true anomaly, φ_2, of the position vector $\bar{P}'_2$ may be obtained as follows:

$$\cos\varphi_2 = \frac{\bar{U}' \cdot \bar{P}'_2}{|\bar{P}'_2|}$$

$$\sin\varphi_2 = \frac{\bar{U}' \times \bar{P}'_2}{|\bar{P}'_2|} \cdot \bar{K}$$

$$\varphi_2 = \tan^{-1}\left(\frac{\sin\varphi_2}{\cos\varphi_2}\right) .$$

The path angle, ϑ_2, at $\bar{P}'_2$ may be computed

$$\vartheta_2 = \sin^{-1}\left(\frac{h}{P_2 V_2}\right)$$

where $90 \leq \vartheta_2 \leq 180$ if $\varphi_2 \geq 180$

$0 < \vartheta_2 < 90$ if $\varphi_2 < 180$.

The velocity vector $\dot{\bar{X}}'_2$ may be computed by the relationship

$$\dot{\bar{X}}'_2 = (-\Delta\varphi)_3 \begin{bmatrix} V_2 \cos\vartheta_2 \\ V_2 \sin\vartheta_2 \\ 0 \end{bmatrix} .$$

Then the velocity vector $\dot{\bar{X}}_2$ in the original coordinate system is given by

$$\dot{\bar{X}}_2 = (\zeta)_3^T \, (i)_1^T \, (\sigma)_3^T \, \dot{\bar{X}}'_2 .$$

Then the vector $\Delta\bar{V} = \dot{\bar{X}}_2 - \dot{\bar{X}}_m$ where $\dot{\bar{X}}_m$ is the velocity of the vehicle at the time of abort. The magnitude $|\Delta\bar{V}| = |\bar{X}_2 - \bar{X}_m|$ and the angle ξ between $\bar{X}_2$ and $\bar{X}_m$ are given by

$$\cos\xi = \frac{\dot{\bar{X}}_2 \cdot \dot{\bar{X}}_m}{|\dot{\bar{X}}_2| \, |\dot{\bar{X}}_m|}$$

$$\sin\xi = \frac{(\dot{\bar{X}}_2 \times \dot{\bar{X}}_m)}{|\dot{\bar{X}}_2| \, |\dot{\bar{X}}_m|} \cdot \bar{K}$$

$$\xi = \tan^{-1}\left(\frac{\sin\xi}{\cos\xi}\right) .$$

III. CONCLUSION

This paper has presented a closed solution to a problem of orbit determination that has direct application to the abort guidance problem. The problem can be presented mathematically as follows:

> Given two radius vectors and the path angle at one of them; determine the unique ellipse which satisfies these conditions.

If this solution were to be applied to the abort guidance problem, it would be necessary to place the vector $\bar{P}_1$ at a specified geocentric position; however, the time it takes a vehicle to traverse from P_2 to P_1 must be taken into account, and during this time interval, the earth would have rotated so that P_2 would no longer be at the specified geocentric position. In order to use this solution, then, an iteration would be necessary to match the time of travel along the determined ellipse and the rotation of the earth.

APPENDIX

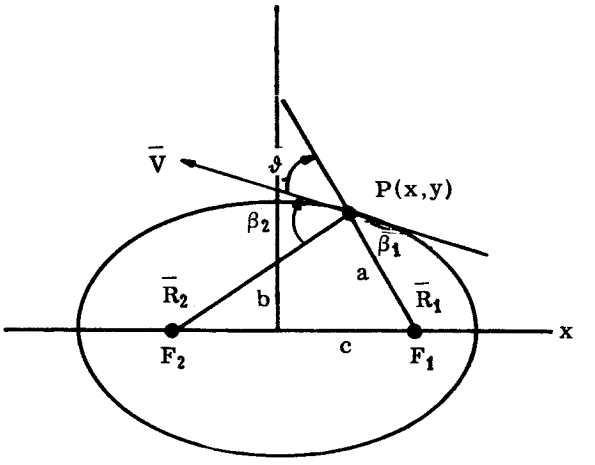

$F_1 = (c,0)$; $F_2(-c, 0)$; $a^2 = b^2 + c^2$

$$F = \frac{X^2}{a^2} + \frac{y^2}{b^2} = 1 \; ; \; b^2X^2 + a^2y^2 = a^2b^2 .$$

Then $\frac{dF}{dx} = 2b^2X + 2a^2y\,\frac{dy}{dx} = 0.$

Hence, the slope of the tangent at any point P(x,y) is given by

$$\frac{dy}{dx} = \frac{-b^2x}{a^2y} = S .$$

This slope is undefined at $y = 0$ (apogee and perigee); however, the angles β_1 and β_2 are readily attainable here.

Now consider any point P(x,y) where $X \neq \pm c$ and $y \neq 0$.

The slope of $R_2 = \frac{y}{x+c} = m_2 \; x \neq -c$

and

the slope of $R_1 = \frac{-y}{c-x} = m_1 \; x \neq c$.

$$\tan\beta_1 = \frac{s - m_1}{1 + (s)(m_1)} = \frac{\frac{-b^2x}{a^2y} + \frac{y}{c-x}}{1 + \frac{b^2x}{a^2y}\,\frac{y}{c-x}}$$

$$= \frac{-b^2x(c-x) + a^2y^2}{y\,a^2(c-x) + b^2x}$$

$$= \frac{-b^2xc + b^2x^2 + a^2y^2}{y\,a^2c - x(a^2-b^2)} = \frac{-b^2xc + a^2b^2}{yc\,(a^2-xc)}$$

$$= \frac{b^2(a^2-xc)}{yc\,(a^2-xc)} = \frac{b^2}{yc} \quad .$$

Hence, $\tan\beta_1 = \frac{b^2}{yc}$ $\quad (y \neq 0,\ X \neq c)$

$$\tan\beta_2 = \frac{m_2 - s}{1 + (s)(m_2)} = \frac{\frac{y}{x+c} + \frac{b^2x}{a^2y}}{1 - \frac{y}{x+c}\,\frac{b^2x}{a^2y}} \qquad \begin{matrix} x \neq -c \\ y \neq 0 \end{matrix}$$

$$= \frac{a^2y^2 + b^2x(x+c)}{y\,a^2(x+c) - b^2x}$$

$$= \frac{a^2y^2 + b^2x^2 + b^2xc}{y\,x(a^2-b^2) + a^2c}$$

$$= \frac{a^2b^2 + b^2xc}{y\,xc^2 + a^2c} = \frac{b^2}{yc}\,\frac{(a^2+xc)}{(xc+a^2)} = \frac{b^2}{yc} \quad .$$

Hence, $\tan\beta_2 = \frac{b^2}{yc} = \tan\beta_1$

since for $y \neq 0$, $x \neq \pm c$; $\beta_1, \beta_2 \neq \pm 90$

$\beta_1 = \beta_2 = \vartheta$.

Now, let us consider the cases where $x = \pm c$. (This will occur at four points on the ellipse.)

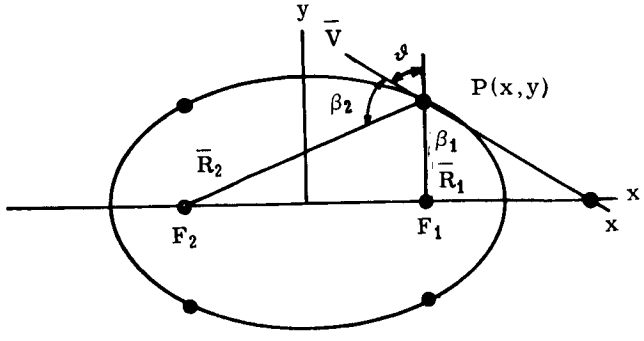

In particular, let us take the case where $x = c$.

m_2 is still given by $\frac{y}{x+c} = \frac{y}{2c}$

S is still given by $\frac{-b^2x}{a^2y} = \frac{-b^2c}{a^2y}$

and $\tan\beta_2 = \frac{b^2}{yc}$.

However, slope of $R_1 = m_1$ is not defined for $x = c$, but

$$\tan\beta_1 = \frac{x'-c}{R_1} = \frac{x'-c}{y} \quad ; \quad y \neq 0$$

where x' is the value of x where the extension of $\bar{V}$ intersects the x-axis.

Further

$$\frac{y'-y}{x'-c} = \frac{-b^2c}{a^2y}, \quad y \neq 0 \ .$$

Now solving of $x'\,(y' = 0)$ we get

$$-y = \frac{-b^2c}{a^2y}\,(x'-c)$$

or

$$\frac{a^2y^2}{b^2c} + c = x' \ .$$

Then $\tan\beta_1 = \frac{x'-c}{y} = \frac{a^2y}{b^2c}$ $\quad x = c,\ y \neq 0$.

Since $\beta_1, \beta_2 \neq \pm 90$, $y \neq 0$,

<u>if</u> $\beta_1 = \beta_2$, then

$\tan\beta_1 = \tan\beta_2$

i.e.,

$$\frac{b^2}{yc} = \frac{a^2y}{b^2c}$$

or

$$b^2 = \frac{a^2y^2}{b^2} \ ,$$

$$b^4 = a^2y^2$$

$$b^2(a^2-c^2) = -b^2x + a^2b^2$$

$b^2x - b^2c = 0.$

Since $x = c$

$b^2c^2 = b^2c^2.$

Since the steps are reversible, $B_1 = B_2 = v$

Solution may be made similarly for $x = -c$.

Where $y = 0$, the proof is trivial.

V. SELENOGRAPHY

LUNAR MARIA TERRAIN MODEL FOR USE IN LUNAR SURFACE VEHICLE MOBILITY STUDIES

By

Otha H. Vaughan, Jr. and Donald Rose

LIST OF SYMBOLS

Symbol	Definition
c	Coefficient of soil cohesion, lbs/in^2
ϕ	Angle of internal friction (between grains), degrees
K_ϕ	Modulus of soil deformation due to frictional ingredients of the soil, lbs/in^{n+2}
K_c	Modulus of soil deformation due to cohesive ingredients of the soil, lbs/in^{n+1}
n	Exponent related to the shape of the pressure-sinkage curve, dimensionless
K_1	Slip parameter reflecting the degree of soil compactness, 1/in
K_2	Slip parameter reflecting the fundamental shape of the soil shear curve, dimensionless
H_{max}	Maximum traction available from soil characteristics, lbs
W	Weight of vehicle per contact area, lbs
W_t	Total weight of the vehicle, lbs
P	Ground pressure per track, lbs/in^2
Z	Sinkage in the soil, in
γ	Specific soil density, lbs/in^3
R	Motion resistance, lbs
R_i	Internal resistance, lbs
R_t	Total motion resistance, lbs
E	Drive motor to track efficiency, per cent
b	Width of bearing surface, per contact area, in
HP	Power, hp
A	Total area in contact with the ground, in^2
l	Length of bearing surface per contact area, in

I. INTRODUCTION

Lunar surface mobility capabilities of a roving vehicle are determined by the interactions of the vehicle with the lunar surface and the characteristics of the lunar soil (bearing strength, slope distribution, obstacle distribution, and many other parameters). The proposed model is an attempt to provide a more realistic maria model than the maria model as proposed by the study, "Engineering Lunar Surface Model" [1], and is based on small scale resolution data as determined from Ranger VII photographic and photometrically generated topographic information. The slope data were developed from the "Topographic Map of a Small Area of the Moon's Surface in Mare Cognitium" (Fig. 1) prepared by the Branch of Astrogeology of the United States Geological Survey (USGS) under NASA contract.

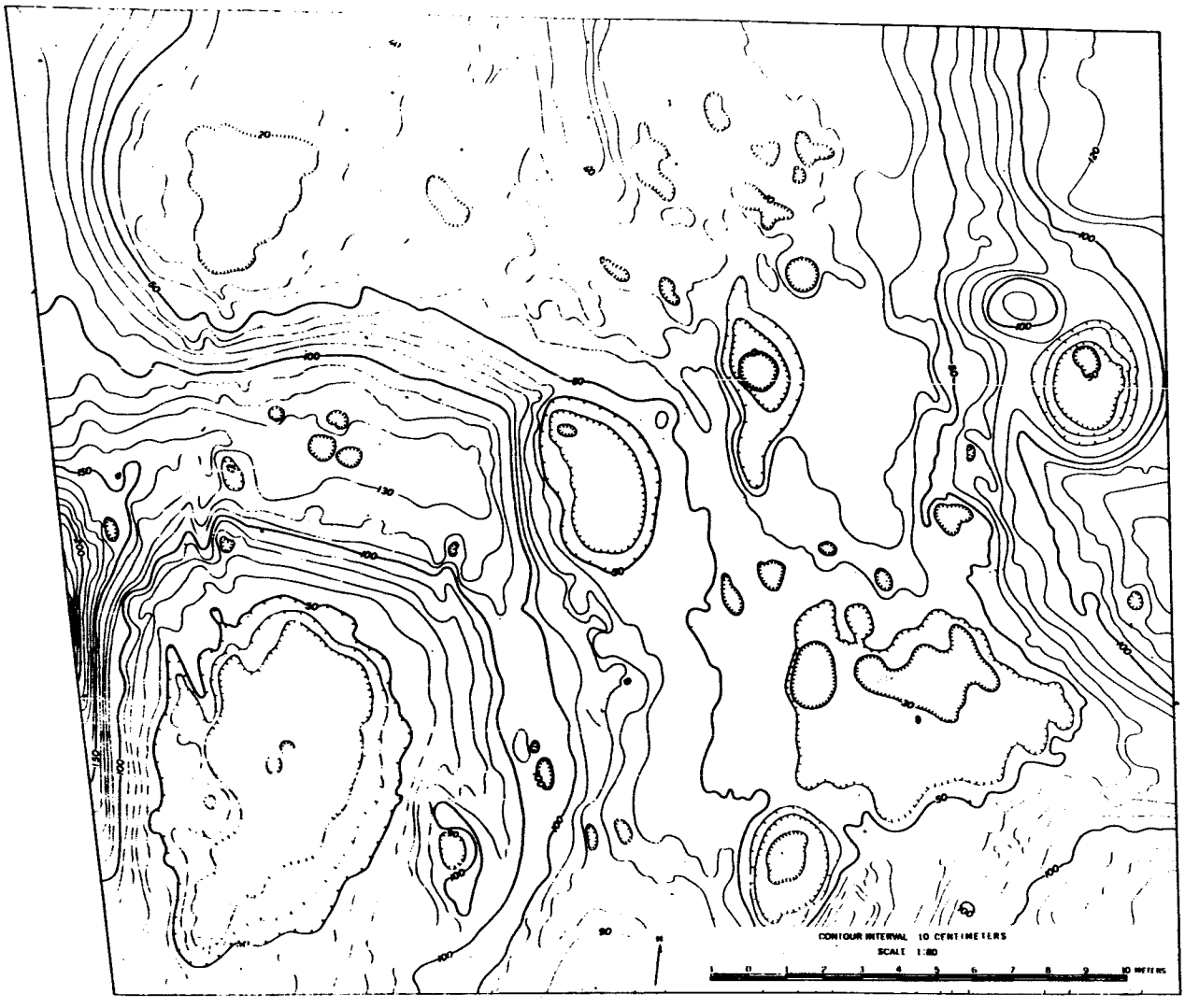

FIGURE 1. TOPOGRAPHIC MAP OF A SMALL AREA OF THE MOON'S SURFACE IN MARE COGNITUM

II. DISCUSSION

A. DISTRIBUTION OF SLOPE FOR THE MARIA MODEL

Since the previous Engineering Lunar Model Surface (ELMS) [1] was developed using small scale maps (1:1,000,000) and supporting photographs to produce a lunar surface model, it now is possible to use the same techniques to develop a large (1:80) scale engineering lunar model surface based on Ranger VII data. To construct this new surface model, a typical traverse for a lunar scientific mission was constructed in the map area. This traverse was 100 meters in length and consisted of of seven different legs as shown in Figure 2. The typical profile for each leg of the total traverse is shown in Figures 3 and 4. After these profiles were constructed, all of the positive and negative slopes were measured and tabulated. The distribution for the positive and negative slopes for this particular traverse was 71.4 per cent and 28.6 per cent, respectively. Only the positive slope data are presented since these are the slopes that require energy to be expended if the vehicle is not considered to use the power system for braking.

B. SOIL PARAMETERS FOR MOBILITY

1. Although the slope frequency distribution diagram gives an indication of the terrain profile, it is still necessary to determine what soil parameters should be used with the model profile. Bekker [2] in his work with locomotion and soil studies evaluated soils in terms of a series of constants. These constants are divided into two categories:

a. Soil Strength

c (cohesion)

ϕ (friction)

b. Soil Deformation

K_{ϕ} (friction modulus of deformation)

K_c (cohesive modulus of deformation)

n (exponent of sinkage)

K (slip coefficient)

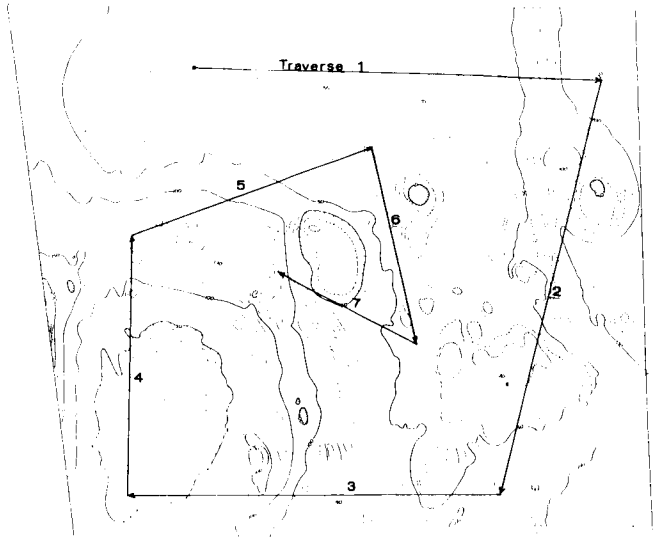

FIGURE 2. LUNAR MARIA SURFACE TRAVERSE

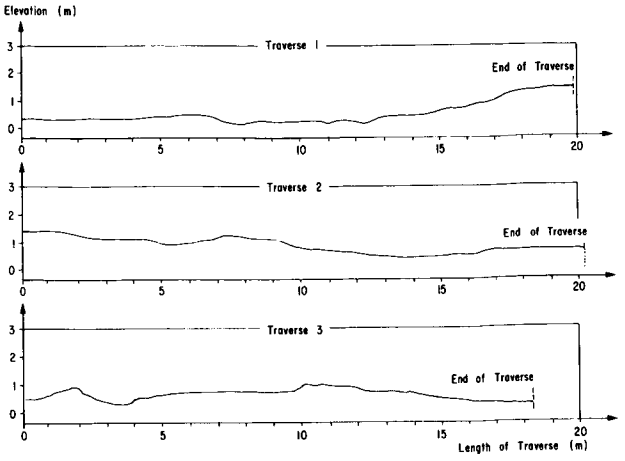

FIGURE 3. LUNAR MARIA TRAVERSE PROFILE

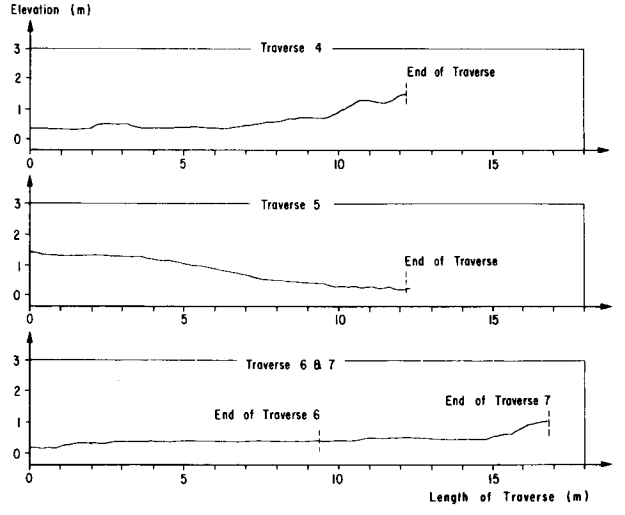

FIGURE 4. LUNAR MARIA TRAVERSE PROFILE

2. Values for these constants have been determined for various types of terrestrial soils, and values have been postulated for lunar soils based on the terrestrial laboratory data. Bekker [2] indicates that the lunar soil, in the absence of an atmosphere and the absence of water, will probably not consist of the saturated plastic clay types, but will probably be similar to sand, gravel, or dry mineral powder. Many other investigators of the lunar surface and its characteristics [2-12] also postulate (based on thermal, photometric, and radar data) that the soils will probably consist of gravel, sand, lava, pumice, or even fine powder. If the lunar soils are of the granular type, they will probably not exhibit the cohesive forces which result from moisture present between the grains. Laboratory data [13] have indicated that the modulus of cohesion (K_c) is equal to zero for both pumice and quartz sand in atmosphere and in vacuum. The soil properties selected for the ELMS model were c = 0, K_c = 0, and ϕ = 32° typical values for a cohesionless dry sand type soil. Laboratory data [14] indicate that the value of n (exponent of sinkage) for terrestrial soils ranges from a minimum of 0.5 for loose, minimum soils to a maximum of 1.25 for hard-packed high strength soils. These experimental data also imply that the value of K_{ϕ} (friction modulus of deformation) ranges from a minimum of 0.1 for a fine pumice or a fluffy, dust type soil to a maximum of six for a hard, dry-packed sand. In selecting these constants for the ELMS, the values for n and K for each slope were

selected such that the small slope material would have values of n = 0.5, and K_{ϕ}=0.5, respectively, increasing to values of n = 1.25 and K_{ϕ}=6 for slopes of 25°. Slopes larger than 25° were considered hard surfaces. Since the soil constants for the lunar surface are still largely unknown and since many thermal, radar, and photometric studies have indicated that the lunar surface may be covered with a fine dust or exhibit the soil characteristics of dry sand, then the soil constants as used in the ELMS model [1] are considered satisfactory at the present time and will be used with this model slope distribution. The revised lunar maria terrain model is presented in Table I.

TABLE I. LUNAR MARIA TERRAIN MODEL

Slope Angle* (Degrees)	Percent of Total Distance	Soil Constants**
0 - 2 2 - 4 4 - 6	44.7% 4.1% 5.6%	K_{ϕ} = 0.5 n = 0.5 (Loose fluffy dust)
6 - 10	5.4%	K_{ϕ} = 1.0 n = 0.75
10 - 20	7.9%	K_{ϕ} = 3.0 n = 1.0 (Loose dry sand)
20 - 30	3.0%	K_{ϕ} = 6.0 n = 1.25 (Hard compacted sand)
30 - 35	0.4%	Hard surface

* The distribution of slopes for this model are the distribution for the positive slopes. Negative slopes are not considered since they do not increase the power requirements unless the power system is used for braking.

** c = 0
K_c = 0
ϕ = 32

C. SLIPPAGE FACTORS FOR MOBILITY

In addition to the values of c, K_c, K_{ϕ}, n, and ϕ, in terms of mobility, one must consider some additional parameters, the slippage factors K_1 and K_2. These slippage factors, as proposed by Bekker, and other expressions as defined by Janosi and Hanamoto [15] are the result of the interactions of the particular soil and wheel combinations. Terrestrial data have indicated that K_1 values range from 0.3 for average soils to approximately 1.0 for the brittle or coherent soils, while K_2 values range from 1.0 for the brittle or coherent soils to approximately 3.0 for loose dry sands. The values for K_1 and K_2 for relatively smooth wheels, as selected for the ELMS [1] were K_1 = 0.2 and K_2 = 1.25. Computer studies [16] have shown that as the value of K_1 decreases from the larger values to smaller values, the effect is to increase the amount of slip for a given soil thrust; however, changes in the value of K_2 does not affect the slippage, but tends to increase or decrease the soil thrust for a given slip. Thus, by selecting a low value for K_1 and K_2, we will have pessimistic values of slip for our lunar soil model; and by a careful selection of a certain set of c, K_c, K_{ϕ}, n, and ϕ, it is possible to establish a model which represents a "worst case" moon surface from the standpoint of determining mobility performance estimates. Since no soil characteristics data have been determined from the Ranger photographic data, we will use the same soil slippage factors as recommended by ELMS [1] for our model slippage factors.

D. ENERGY REQUIRED FOR MOBILITY

Through the use of computer programs, incorporating the equations as developed by Bekker [2] to determine mobility energy requirements and using this maria model, the energy requirements for a vehicle traversing a smooth surface can be calculated. The mobility energy, as determined by this maria model, does not include that energy which is required to negotiate obstacles in the maria. An illustration on the use of the model constants and equations used in a mobility analysis can be found in Appendix A.

E. OBSTACLE DISTRIBUTION

The obstacle distribution for this particular maria has not yet been developed. Although the Ranger data did not show the surface littered with blocky debris, one must remember that lunar maria in some areas may still have some obstacles which are not recognizable due to the resolution of the Ranger VII data.

III. CONCLUSIONS

Although this model is developed from a small area within Mare Cognitium, it seems to represent a typical maria model for use in future lunar scientific mission planning studies. When better data

on the characteristics of the lunar surface are obtained, then many different traverses will be constructed and a more realistic lunar maria surface model will be developed. The major difference between this model and the ELMS [1] is the slope distributions. This proposed maria surface model produces a more rugged terrain for use in scientific mission planning studies and appears to be more realistic since it is based on a topographic map prepared from one meter resolution data.

APPENDIX A

The soft soil mobility of an off-the-road land roving vehicle is determined by many vehicle and soil parameters such as number of wheels or tracks, shape and size of ground contact area, center of gravity location, soil characteristics, vehicle speed, etc. The following simplified analysis will be used to illustrate how some of the soil constants as postulated can be used in a soft soil mobility analysis.

I. Statement of the Problem

A lunar roving vehicle weighing 2,328 pounds on the lunar surface is equipped with tracks for mobility. The vehicle tracks in contact with the surface each have a width of 12 inches and a length of 97 inches. Each track supports a load of 1,164 pounds. The centerline of the tracks is 12 feet apart, and there is no elastic deformation of the track. The soil model will be the loose fluffy dust soil (K_{ϕ}=0.5, n = 0.5, K_c = 0, c = 0, and $\phi = 32°$). The vehicle will operate on level terrain, and the slippage effects between soil and tracks will be neglected. Since the soil constants are normally stated in English units, the problem will be solved using English units; however, the results will be given in English and metric units.

II. To Be Determined

A. The maximum tractive effort available from the soil.

B. The sinkage of the vehicle in the soil.

C. The total resistance (R_t) created by the soil and the vehicle during motion.

D. The horsepower (HP) required to drive the vehicle at 5 miles/hour over a loose, fluffy dust, level terrain assuming a power transfer efficiency of 80 per cent (the drive motor to the track).

III. Solution

A. To determine the maximum tractive effort (H_{max}) produced by the soil, we use the Bekker equation [14] for a tracked vehicle while recognizing that it neglects the effect of slippage between the tracks and the soil:

$$H_{max} = Ac + W_t \tan \phi$$

since c = 0 from the model, the equation becomes

$$H_{max} = W_t \tan \phi$$

where ϕ is the angle of internal friction and W_t is the total weight of the vehicle,

using W_t = 2,328 lbs. and $\phi = 32°$ from the model,

then H_{max} = 1,455 lbs. (659.98 kg).

Thus in frictional soils (c = 0), the tractive effort depends only on the vehicle weight and the angle of internal friction and not the contact area.

Since the tracked vehicle as stated in the problem has a large track length with respect to the width, the effect of the slippage constants K_1 and K_2 can be neglected in this simplified analysis. However, if a comparison must be made of the track versus the wheel from an overall mobility standpoint (various soils, obstacles, etc.), then these constants must be considered in the mobility analysis.

B. The depth of sinkage (Z) can be determined using the Bekker equation [2] for the sinkage of a track or a high deflection elastic wheel in soils:

$$Z = \left[\frac{P}{\frac{K_c}{b} + K_\phi} \right]^{\frac{1}{n}}$$

where

$$P = \frac{W_t}{2b1} = \frac{2,328}{(2)\ (12)\ (97)} = 1.0 \text{ lb/in}^2 \ (70.31 \text{ g/cm}^2).$$

Since $K_c = 0$ from the model, the equation reduces to

$$Z = \left[\frac{P}{K_\phi} \right]^{\frac{1}{n}}$$

using $P = 1.0$ lbs/in^2, $n = 0.5$, and $K_\phi = 0.5$ then the sinkage/track

$Z = 4$ inches sinkage (10.16 cm).

The vehicle track will sink into the soil 4 inches (10.16 cm), before it will exert a bearing pressure of 1.0 lb/in^2 (70.31 g/cm^2).

C. The total resistance (R_t) to motion created by the soil and the vehicle during its motion is due to the soil compaction, resistance due to soil bulldozing, and the internal resistance due to friction in the bearings, links, etc. of the track.

1. The rolling resistance due to compaction of the soil can be determined by using the Bekker equation [18].

$$R_c = \frac{b\,(P)^{\frac{n+1}{n}}}{(n+1)\left[\frac{K_c}{b} + K_\phi \right]^{\frac{1}{n}}}$$

where

b = width of the bearing surface per contact area.

Since $K_c = 0$ from the model, the equation becomes

$$R_c = \frac{b\,(P)^{\frac{n+1}{n}}}{(n+1)\left[K_\phi \right]^{\frac{1}{n}}}$$

using b = 12 inches,

$P = 1.0$ lbs/in^2

$K = 0.5$, and

$n = 0.5$

then

$R_c = 32$ lbs/track (14.52 kg/track).

The motion resistance due to both tracks is equal to 64 pounds, (29.03 kg).

2. The bulldozing resistance of a track or wheel can be determined using the equation as recommended by Hegedus [17].

$$R_b = 1/2\ \gamma\ bz^2 \tan^2 (45^\circ + \phi/2 + 2cbz \tan (45^\circ + \phi/2).$$

Since $c = 0$, the equation reduces to

$$R_b = 1/2\ \gamma\ bz^2 \tan^2 (45^\circ + \phi/2).$$

Using $Z = 4$ inches, $b = 12$ inches, $\phi = 32^\circ$, and with a loose fluffy dust we assume $\gamma = .01$ lbs/in^3.

Then

$R_b = 3.12$ lbs/track (1.42 kg/track).

Thus, the total bulldozing resistance due to both tracks is equal to 6.24 lbs., (2.83 kg).

3. The internal resistance (R_i) due to the friction in bearings, links, etc., of the track can be determined as follows:

$$R_i = fW_t$$

where

f = coefficient of internal friction, approximately 0.04 for a small tracked vehicle,

using

$W = 2,328$ lbs and $f = 0.04$

then

$R_i = 93.12$ lbs. (42.24 kg) for both tracks.

4. The total resistance (R_t) is the sum of all these resistances:

$$R_t = R_c + R_b + R_i$$

R_t = 163.36 lbs. (74.10 kg).

D. The horsepower (HP) required to drive the vehicle at 5 mph over a loose, fluffy dust, level terrain can be determined as follows:

$$HP = \frac{(R_t)\ (V)}{(550)\ (E)}$$

$$HP = \frac{\text{(Total Resistance) (Velocity)}}{\text{(Drive motor to track efficiency) (550 ft-lbs/sec-hp)}}$$

using

R_t = 163.36 lbs., V = 7.30 ft/sec (5 mph), and a drive motor to track efficiency of 80 per cent.

Then, the required horsepower is 2.71 hp, (2.02 kw).

This analysis has demonstrated how the model soil constants can be used to determine some of the capabilities of a vehicle. In a complete mobility analysis, many other parameters must be determined before the vehicle mobility capabilities can be established.

REFERENCES

1. Mason, R., McCombs, W., and Cramblit, D.: Engineering Lunar Model Surface (ELMS). TR-83-D, 4 September 1964.

2. Bekker, M.: Mechanics of Locomotion and Lunar Surface Vehicle Concepts. TM 62-217, October 1962.

3. Sharnov, V. V.: The Nature of the Lunar Surface. Chapter IX, "The Moon," University of Chicago Press, 1962.

4. Gold, T.: Structure of the Lunar Surface. CRS Report 156, Cornell University Center for Radiophysics and Space Research, 1963.

5. Rogers, J., and Vaughan, O. H.: Lunar Environment and Interpretation of the Surface of the Moon and Its Atmosphere. NASA TM X-53124, 3 September 1964.

REFERENCES (Concluded)

6. Ryan, J. A.: Lunar Miscellany. Douglas Report SM-43544, April 1963.

7. Kopal, A., and Mikhailov: Physical Studies of the Lunar Surface. Academic Press, 1962, pp. 371-471.

8. McCracker, C. W., and Dubin, M.: Dust Bombardment on the Lunar Surface. NASA TN D-2100, February 1963.

9. Troitskii, V. S.: Nature and Physical State of the Surface Layer of the Moon. Soviet Astronomy: Vol. 6, No. 1, July and August 1962.

10. Bensko, J., Cortez, J. L., Fields, S. A., and Weathers, H.: Lunar Surface Conditions. MTP-M-63-1, 15 March 1963.

11. Halajian, J. D.: The Case for a Cohesive Lunar Surface Model, Grumman ADP Report 04-04-642, June 1962.

12. Hapke, B., and Van Horn, H.: Photometric Studies of Complex Surfaces with Applications to the Moon. CRS Report 139, Cornell University Center for Radiophysics and Space Studies, 1963.

13. Wong, R. E., and Kern, C.: Test Program for Determining Soil Constants in Vacuum. Ref. NASw 642, September 1963.

14. Bekker, M. G.: Off-the-Road Locomotion. University of Michigan Press, 1960.

15. Janosi, Z., and Hanamoto, B.: The Analytical Determination of Draw Bar Pull as a Function of Slip for Tracked Vehicles in Deformation Soils. Proceedings of the First International Conference on the Mechanics of Soil-Vehicle Systems, Edizioni Menerva Tecnica, Torino, Italy, June 1961.

16. Lunar Logistic Systems, Payloads. Vol. 10, MTP-M-63-1, 15 March 1963, pp. 72-80.

17. Hegedus, E.: A Simplified Method for Determination of Bulldozing Resistance. Land Locomotion Research Laboratory, Army Tank Automotive Command, Report No. 61, Detroit, Michigan, May 1960.

18. Olivier, J., and Crambit, D.: Mobility on the Lunar Surface. MTP-M-63-1, 15 March 1963.

VI. SPACE ENVIRONMENT

REVISED METEOROID FLUX AND PUNCTURE MODELS

By

Charles C. Dalton

SUMMARY

Interrelated cubic polynomial models are constructed for log puncture flux versus log effective target thickness and for log mass-cumulative incident flux versus particle mass, which give the best agreement between meteoroid measurement satellite data and photographic meteor data without relaxing the assumption that p/d is independent of d for particles of different velocity, where p and d are puncturable thickness and particle diameter, respectively.

An accurate account of the expected mean hazard for meteoroid puncture in earth orbit is needed for design and operations planning purposes for future programs. The model developed below is thought to give mean puncture flux accurate to within a factor 2 probable error with target equivalent thickness between 15 and 10^{-4} centimeters of aluminum. The corresponding model for mass-cumulative incident flux is also developed.

LIST OF SYMBOLS

Symbol	Definition
log	Logarithm with base ten.
p	Thickness of a just-puncturable sheet in centimeters.
d	Projectile diameter in centimeters.
v	Meteoroid air-entry velocity in kilometers per second.
v_m	Meteoroid lunar impact velocity in kilometers per second.
f(v)	Probability density function for v.
m	Mass of a meteoroid in grams.
$F_>$	Flux of meteoroids of mass equal to or greater than m; mean number of hits per square meteor per second per 2Π steradians without earth shielding.
p_o	Crater depth in centimeters for a semi-infinite target.
t	Target subscript.
C	Velocity of sound in kilometers per second in an unbounded solid.
E	10^{-6} x Young's modulus in kilograms per square centimeter.
ϵ	Ductility, relative elongation in 2-inch gauge length at fracture.
ν	Poisson's ratio.
$\bar{m}$	Meteoroid mass in grams nominally sufficient to puncture.
ϕ	Puncture flux; mean number per second per square meter of surface with 2Π steradian exposure.
β_2 and β_3	Respectively, the slope and intercept of the tangent to the curve for log $F_>$ versus log m.
β_5	Logarithm of the puncture flux enhancement factor due to the statistical variation of the particle and impact parameters.
x_2, x	Angle of impact of incident and of puncturing meteoroids, respectively, with respect to the surface normal in radians.
H_t	Material hardness in Brinell units.
k_4	Material parameter, (2/3) log $(\rho_t C_t)$ - 1.162.
y	Target parameter, k_4 + log p.
$a_0, \ldots a_3$	Constants.
z	Log ϕ, $a_0 + a_1 y + a_2 y^2 + a_3 y^3$.

LIST OF SYMBOLS (Concluded)

Symbol	Definition
R	Radius of effectively shielding atmosphere, 6487 km.
H	$(\frac{1}{2})$ (Perigee + Apogee) -109 km, effective height above atmosphere.
ζ	$(\frac{1}{2})$ [1 + cos $\sin^{-1}$ [R/(R+H)], relative exposability of randomly oriented surface [18].
At	Second-square-meters (partially shielded).
Δ_p	Centimeters thickness allowance for non-metallic mass in capacitor structure.
M. L.	Maximum likelihood value.
G	10^{-6} x torsion modulus in kilograms per square centimeter.
F_s and ϕ_s	Mean incident and puncture flux, respectively, per second per square meter of a randomly oriented surface near the earth ($\zeta = \frac{1}{2}$).

I. DISCUSSION AND RESULTS

It had been expected previously [1] that meteoroids with air-entry velocity only slightly in excess of escape velocity could be relatively so much more abundant, especially for those of small mass, that their flux in cislunar space might be strongly dependent on gravitational potential. But a weighted analysis of photographic meteor data [2] shows no significant statistical relation between mass and velocity, and gives the velocity distribution shown in Figure 1. The weighted mean log velocity is log 27 kilometers per second; and only 25 percent of the total flux is due to the gravity-effect factor. The remaining component, shown also in Figure 1, can be transformed into the distribution of lunar impact velocity shown in Figure 2, with median coincidentally 27 kilometers per second. In the same analysis the mean air-entry meteoroid flux was found to be

$$F = 10^{-14.49}\, m^{-1.34} \qquad (1)$$

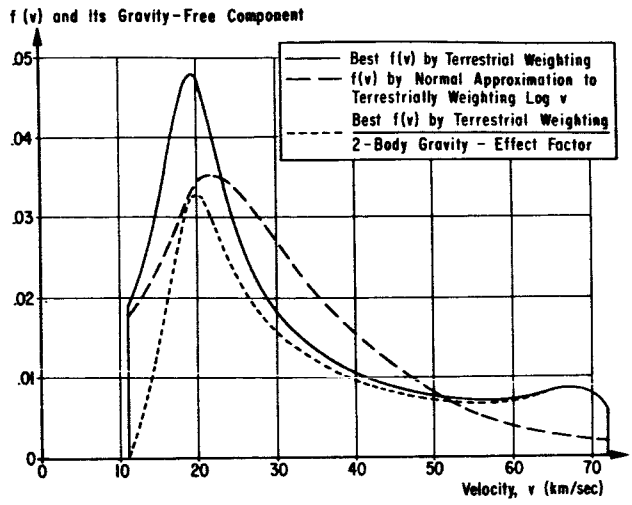

FIGURE 1. PROBABILITY DENSITY FUNCTION FOR METEOROID AIR-ENTRY VELOCITY

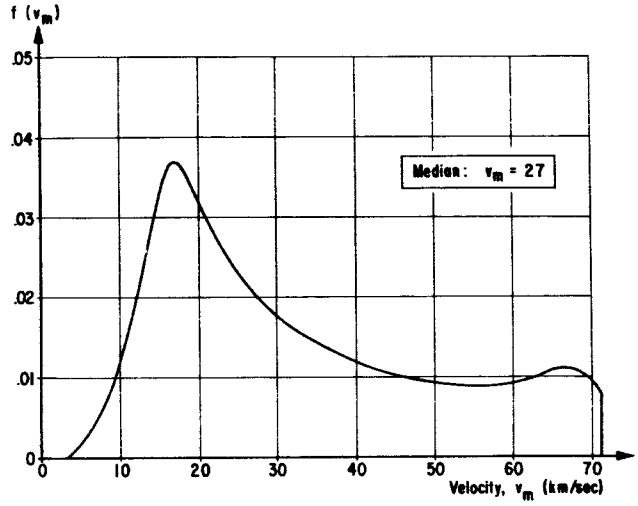

FIGURE 2. PROBABILITY DENSITY FUNCTION OF LUNAR-SURFACE IMPACT VELOCITY FOR PRIMARY METEOROIDS

when the particle material density is [3]

$$\rho = 0.44 \qquad (2)$$

and the least-countable mass m is in the interval $10^{-1.13} \leq m \leq 10^{-0.23}$. In establishing Equation (1) the mass of the zero-visual-magnitude-30-kilometer-per-second meteor has been increased 0.2 order of magnitude over Whipple's [3] one-gram estimate in consideration of the cube of the relative change in the 85-90 kilometer pressure for Reference 4 ,,versus Reference 5 which Whipple used (basis: Opik [6]).

Correspondingly, the mean lunar impact flux would be $10^{-14.61}\ m^{-1.34}$. When allowance is made for the mean solid angle of exposure for a surface in orbit, the mean flux will not differ appreciably from the fixed-level-surface values given above.

In a survey and multivariable analysis of available laboratory hypervelocity impact data, Reismann, Donahue and Burkitt [7] found that in the highest of three velocity regimes the multiple correlation coefficient is nearly maximized (to 0.989) by representing the relation between projectile and target parameters for impact at normal incidence as follows:

$$p_o/d = 2.5(v/C_t)^{0.50}(E/E_t)^{1.31}(\nu/\nu_t)^{8.0}(\epsilon/\epsilon_t)^{0.43} \quad (3)$$

The relation between puncturable target thickness p and crater depth p_o has been treated in considerable analytical depth by Andriankin and Stepanov [8]. Their results indicate that the ratio p/p_o is a function of the projectile and target material parameters and of the impact velocity, varying between somewhat more than 1 to somewhat less than 2 for impact velocity above about 6 kilometers per second. Herrmann and Jones [9] illustrate experimental results (which they attribute to Kinard, et al. at NASA, Langley) and an empirical formula indicating that, as target thickness is decreased toward the value p, the value of p/p_o approaches

$$p/p_o \rightarrow (1/1.3)^2 + 1 = 1.59. \quad (4)$$

If Equations (3) and (4) are valid for meteoroid impact, then p/d is independent of d, and the slope of log ϕ versus log p should be three times the slope of log $F_>$ versus log m, where ϕ is the puncture flux corresponding to incident flux $F_>$. Therefore, if the slope of log $F_>$ versus log m for photographic meteors in the vicinity of 10^{-1} gram mass, expressed by the constant -1.34 in Equation (1), were applicable also for the particles puncturing the meteoroid measurement satellites, then the slope of log ϕ versus log p should be -4.02 for the satellite puncture data. But in a previous working paper [10] the value -1.966 for the slope of log ϕ versus log p was shown to fit the satellite data very well. At first the author [10] interpreted this discrepancy between the -4.02 and -1.966 results as indicating that p/d is not essentially independent of d for meteoroid impact circumstances; but, after extensive consultation and further analysis, the present interpretation is that the slope of log $F_>$ versus log m is not essentially independent of m.

Because puncture flux ϕ versus effective target thickness p is of more direct technological interest than incident flux $F_>$ versus particle mass m, even though the opposite might be true for scientific interests, a model should be developed first for ϕ versus p by using the satellite puncture data and computed values of ϕ and p corresponding to the photographic meteor data, Equation (1). The relation between incident flux $F_>$ and puncture flux ϕ must be established through

$$F_> = 10^{\beta_3} m^{\beta_2} \quad (5)$$

and

$$\phi = 10^{\beta_3 + \beta_5} \bar{m}^{\beta_2}, \quad (6)$$

where β_2 and β_3 are, respectively, the slope and intercept of the tangent to the curve for log $F_>$ versus log m, $\bar{m}$ is the mass of the meteoroid which, with mean values of density ρ, velocity v, and angle of incidence x_2 with respect to the surface normal, is just sufficient to puncture the target of interest, and 10^{β_5} is the puncture flux enhancement factor [11] due to the statistical distribution of the parameters ρ, v, and x_2.

Recently, Equation (3) had been preferred [1, 10, 11, 12] as a basis for the relative puncturability of targets of different materials. That preference was based both on the detailed involvement of various material parameters and on the fact that the velocity exponent had the same value as had been preferred previously by the author [13, 14] because it was intermediate between the values supported by different authors [9, 15] at that time. The author [13, 14] had preferred

$$p_o = 10^{0.434}(\rho m/\rho_t H_t)^{1/3}(v \cos x_2)^{\frac{1}{2}} \quad (7)$$

where H_t is the material hardness in Brinell units. Then, by Equations (1), (2), (4), and (7), a meteroid with nominal mass $\bar{m} = 10^{-1}$ gram, nominal density $\rho = 0.44$, nominal velocity $v = 27$ kilometers per second, and nominal impact angle $x_2 = \Pi/4$ radians impacting a sheet of 2024 T-3 aluminum with density $\rho_t = 2.77$ and Brinell hardness $H_t = 120$ would just puncture the sheet of thickness $p = 10^{-0.017}$ or 0.96 centimeter. For the same conditions except with the intermediate value $\beta_2 = -1.23$, and Equation (7), the author [11] found

the puncture flux enhancement factor to be $10^{\beta_5} = 10^{0.70}$. Then, with Equations (1), (5), and (6), the mean puncture flux for $\overline{m} = 10^{-1}$ would be $\phi = 10^{-14.45}$. A line between this point (log ϕ, log p) = (-14.45, -0.017) and the corresponding point for the thickest Pegasus target would have a slope of -4.02 = 3(-1.34), which would support the extrapolation of Equation (1) if it were not for the fact that the puncture data for thinner targets (both on Pegasus and on Explorers XVI and XXIII) definitively establish a lower slope. It does not seem reasonable to accept an abrupt change in slope from about -4 to about -2 in the immediate vicinity of the Pegasus data point. Then it must be assumed that puncturable thickness p varies more steeply with velocity v than would be indicated by Equation (7). Therefore, the author prefers to abandon both of the formulations in Equations (3) and (7) for meteoroid puncture.

The NASA-Ames penetration criterion (by Summers [16] in 1959) has been recommended recently for meteoroid puncture analysis by Dohnanyi [17]; i.e.,

$$p_o = 3.56 \{ (m\rho/2\rho_t^2) [v(\cos x_2)/C_t]^2 \}^{1/3} . \quad (8)$$

Together, Equations (4) and (8) indicate that p/d is again independent of d. With $C_t = 6.25$ from [7] for 2024T-3 aluminum, the nominal meteoroid, with $\overline{m} = 10^{-1}$ and with the values for the other parameters mentioned above, the puncturable thickness is $p = 10^{0.229}$ or 1.69 centimeters, 76 percent thicker than that which was inferred by Equation (7).

Equations (4) and (8) lead to some revision in the puncture flux enhancement factor 10^{β_5} and in the probability density function of the angle of impact x of a puncturing meteoroid, as derived in [11]. It seems appropriate to retain the same value 0.52 for the standard deviation of log puncturable mass instead of increasing it to 0.57 to account for the stronger dependence on velocity in Equation (8). This accommodation is supported by a reduction in the standard deviation of log material density from 0.44 to 0.38. Then, by the derivation [11], differential puncture flux $d\phi$ must be multiplied by $e^{-\frac{1}{4}} (\cos x)^{-\frac{1}{2}}$. The results of this alteration are that

$$\beta_5 = 0.63 \quad (9)$$

$$f(x) = 1.77 (\cos x)^{1.54} \sin 2x. \quad (10)$$

Therefore, by Equations (5), (6), (9), and (10), the puncture flux enhancement factor is 4.26 instead of 5.05 and the median impact angle x for the puncturing meteoroids is 34.7 instead of 33.5 degrees from the normal.

By Equations (1), (5), (6), and (9), the mean puncture flux which is inferred by Equations (4) and (8) for $\overline{m} = 10^{-1}$ gram is $\phi = 10^{-14.52}$, with $p = 10^{0.229}$ for 2024T-3 aluminum. However, because Equation (1) represents the photographic meteor data over the interval $10^{-1.13} \leq m \leq 10^{-0.23}$, the nominally puncturing mass which is represented best is $\overline{m} = 10^{-0.68}$ with $F_> = 10^{-13.579}$. This corresponds to the point (log ϕ, log p) = (-12.949, 0.336) for 2024T-3 aluminum.

By introducing a material constant k_4 and a target parameter $k_4 + \log p$ and the values of the parameters already used with Equations (4) and (8), one can write

$$\overline{m} = 10^{3k_4 - 0.678 p^3} \quad (11)$$

$$k_4 = (2/3) \log (\rho_t C_t) - 1.162 \quad (12)$$

$$y = k_4 + \log p \quad (13)$$

$$= (1/3) \log \overline{m} + 0.226 \quad (14)$$

$$z = \log \phi \quad (15)$$

$$= a_0 + a_1 y + a_2 y^2 + a_3 y^3 \quad (16)$$

where $a_0, \ldots, a_3$ are constants to be determined below. Also,

$$\beta_2 = (1/3) (a_1 + 2a_2 y + 3a_3 y^2) \quad (17)$$

$$\beta_3 = z - 0.63 - \beta_2 \log \overline{m} . \quad (18)$$

Therefore, with Equations (5) and (14) through (18), one can determine the mass-cumulative flux $F_>$ as a function of mass m.

The constant term in Equation (12) for the material constant k_4 has been chosen so that the target parameter y in Equations (13) and (14) vanishes for the photographic meteor value log $\overline{m}$ = -0.68 and log ϕ = -12.949. Therefore, in Equation (16),

$$a_o = -12.95 \quad (19)$$

and, by Equations (1) and (11),

$$a_1 = -4.02 . \quad (20)$$

The values of the other constants a_2 and a_3 in Equations (16) and (18) must be determined by the satellite puncture data.

Puncture data for five meteoroid measurement satellites, compiled in Table 1, adjusted to remove earth-shielding according to the mean solid angle of exposure, are plotted in Figure 3. The values of the physical constants for the materials are also given in Table 1. The values used for p for the Pegasus

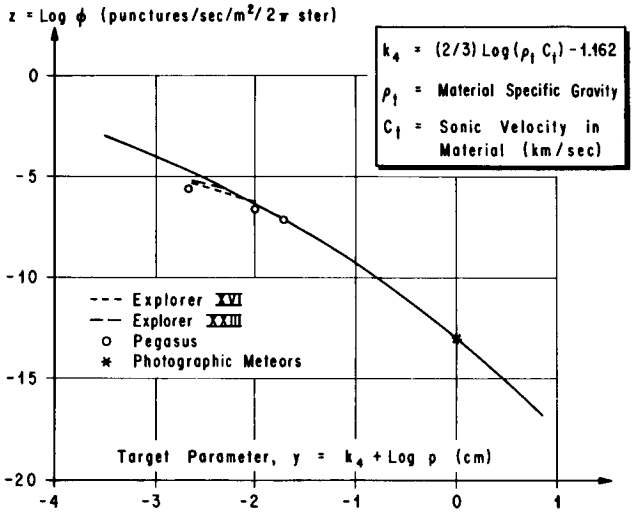

FIGURE 3. METEOROID PUNCTURE FLUX VS EFFECTIVE TARGET PARAMETER

sensors include a 10^{-3} - centimeter increment in consideration of the non-metallic components of the capacitor puncture sensors [1].

The values of log ϕ, as shown in Table 1 and Figure 3, have been corrected for geometric shielding [18] by dividing the mean puncture flux by ζ. Poisson's ratio for the Explorer XVI transducer material was calculated from Baumeister [19]:

$$\nu = (E - 2G)/2G. \quad (21)$$

Values for velocity of sound in the transducer materials were calculated with the extended-medium formula [7, 20]

$$C = 9.90 \left\{ (E/\rho) [(1-\nu)/(1+\nu)(1-2\nu)] \right\}^{\frac{1}{2}} \quad (22)$$

instead of from the corresponding formula for thin plates [21].

The two conditions for the satellite puncture results from Table 1 and Figure 3 which seem most significant for the determination of the constants a_2 and a_3 in Equation (16) are 1) the values -1.717 and -7.171 for the abscissa y and the mean ordinate z, respectively, for the thickest Pegasus target, and 2) the values -2.383 and -1.58 for the abscissa y, and the Hastings [27] maximum likelihood slope dz/dy, respectively, for the Explorer XVI target of intermediate thickness. Therefore, by these two conditions and Equations (16), (19), and (20),

$$a_2 = -0.424 \quad (23)$$

$$a_3 = -0.025 . \quad (24)$$

By Equations (13), (15), (16), (19), (20), (23), and (24), the relation between puncture flux ϕ and target parameter $(k_4 + \log p)$ is

$$\log \phi = -12.95 - 4.02 (k_4 + \log p) - 0.424 (k_4 + \log p)^2 - 0.025 (k_4 + \log p)^3 \quad (25)$$

where the material parameter k_4 is given by Equation (12). The corresponding numerical results are superimposed on Figure 3 for comparison with the satellite puncture data. It should be noted that, although the Pegasus puncture flux has been adjusted upward to correct for the approximately 30 percent earth shielding, it has not been corrected upward to correct for any counting loss, which might be about 14 percent [29].

The values of the mass-cumulative flux $F_>$ and mass m, corresponding to any point on the curve in Figure 3, can be computed most readily from

$$\log m = 3(k_4 + \log p) - 0.68 \quad (25)$$

$$\log F_> = \log \phi - 0.63 . \quad (26)$$

For example, the thickest Pegasus target is being punctured by particles with about 1.5 micrograms mass.

The results, which may be accurate to within a factor 2 probable error, are illustrated further in Figure 4 for the mass-cumulative flux $F_>$ (per effectively exposed hemisphere). For better comparison with other models, Figures 5 and 6 show the mass-cumulative flux F_s and puncture flux ϕ_s for a randomly oriented vehicle at low orbital altitude from the earth.

TABLE 1. DATA FOR TWELVE SATELLITE PUNCTURE TRANSDUCERS

ENTITIES	DATA AND SOURCES											
Satellite	Explorer XVI	Explorer XVI	Explorer XVI	Explorer XXIII	Explorer XXIII	Pegasus I	Pegasus II	Pegasus II	Pegasus II	Pegasus III	Pegasus III	Pegasus III
Launch Date	12-16-62	12-16-62	12-16-62	11-6-64	11-6-64	2-16-65	5-25-65	5-25-65	5-25-65	7-30-65	7-30-65	7-30-65
	[22]	[22]	[22]	[23]	[23]	[24]	[25]	[25]	[25]	[26]	[26]	[26]
Perigee (km)	750	750	750	463	463	497	506	506	506	529	529	529
	[22]	[22]	[22]	[23]	[23]	[24]	[25]	[25]	[25]	[26]	[26]	[26]
Apogee (km)	1180	1180	1180	980	980	745	748	748	748	532	532	532
H	856	856	856	612	612	512	518	518	518	422	422	422
	[27]	[27]	[27]	[23]	[23]	[28]	[28]	[28]	[28]	[28]	[28]	[28]
Punctures	44	11	0	24	25	125	121	18	58	71	14	41
	[27] Fin.	[27] Fin.	[27] Fin.	[23]	[23]	[28]	[28]	[28]	[28]	[28]	[28]	[28]
Tally Date	7-22-63	7-22-63	7-22-63	2-11-65	2-11-65	9-5-65	9-2-65	9-2-65	9-2-65	10-8-65	10-8-65	10-8-65
	[27]	[27]	[27]	[23]	[23]	[28]	[28]	[28]	[28]	[28]	[28]	[28]
Log At	7.060	6.738	6.512	6.731	7.065	7.953	7.737	8.014	9.101	7.587	7.938	8.951
ζ	0.734	0.734	0.734	0.703	0.703	0.688	0.689	0.689	0.689	0.672	0.672	0.672
	[27] M.L.	[27] M.L.	[27] M.L.									
Log ϕ	-5.266	-5.696	-6.275	-5.197	-5.514	-5.693	-5.492	-6.597	-7.176	-5.563	-6.619	-7.165
	[27]	[27]	[27]	[23]	[23]	[29]	[29]	[29]	[29]	[29]	[29]	[29]
$10^4(p-\Delta p)$	29.2	54.6	127	25.4	50.8	38±3	38±3	203±25	406±50	38±3	203±25	406±50
						[1]	[1]	[1]	[1]	[1]	[1]	[1]
$10^4(\Delta p)$	0	0	0	0	0	10	10	10	10	10	10	10
Log p	-2.535	-2.263	-1.896	-2.595	-2.294	-2.317	-2.317	-1.671	-1.381	-2.317	-1.671	-1.381
	[22]	[22]	[22]	[23]	[23]	[1] Al.	[1] Al.	[30] Al.	[30] Al.	[1] Al.	[30] Al.	[30] Al.
Material	Berylco 25	Berylco 25	Berylco 25	AISI 302	AISI 302	1100-H14	1100-H14	2024-T3	2024-T3	1100-H14	2024-T3	2024-T3
Condition	[22] Annealed	[22] Annealed	[22] Annealed	[23] $\frac{1}{2}$ hard	[23] $\frac{1}{2}$ hard							
Rockwell No.	[22] B 60	[22] B 60	[22] B 60									
ρ_t	[31] 8.23	[31] 8.23	[31] 8.23	[30] 7.83	[30] 7.83	[7] 2.72	[7] 2.72	[7] 2.77	[7] 2.77	[7] 2.72	[7] 2.77	[7] 2.77
E_t	[31] 1.195	[31] 1.195	[31] 1.195	[19] 1.941	[19] 1.941	[7] 0.703	[7] 0.703	[7] 0.745	[7] 0.745	[7] 0.703	[7] 0.745	[7] 0.745
G_t	[31] 0.457	[31] 0.457	[31] 0.457	[19] 0.745	[19] 0.745							
ν_t	0.308	0.308	0.308	[19] 0.305	[19] 0.305	[7] 0.33	[7] 0.33	[7] 0.33	[7] 0.33	[7] 0.33	[7] 0.33	[7] 0.33
C_t	4.44	4.44	4.44	5.73	5.73	[7] 6.12	[7] 6.12	[7] 6.25	[7] 6.25	[7] 6.12	[7] 6.25	[7] 6.25
ϵ_t	[32] 0.46	[32] 0.46	[32] 0.46	[30] 0.15	[30] 0.15	[7] 0.20	[7] 0.20	[7] 0.18	[7] 0.18	[7] 0.20	[7] 0.18	[7] 0.18
k_4	-0.120	-0.120	-0.120	-0.061	-0.061	-0.348	-0.348	-0.336	-0.336	-0.348	-0.336	-0.336
k_4 + log p	-2.655	-2.383	-2.016	-2.656	-2.355	-2.665	-2.665	-2.007	-1.717	-2.665	-2.007	-1.717
Sensor Structure	Pressure Can	Pressure Can	Pressure Can	Pressure Can	Pressure Can	Capacitor Sandwich	Capacitor Sandwich	Capacitor Sandwich	Capacitor Sandwich	Capacitor Sandwich	Capacitor Sandwich	Capacitor Sandwich

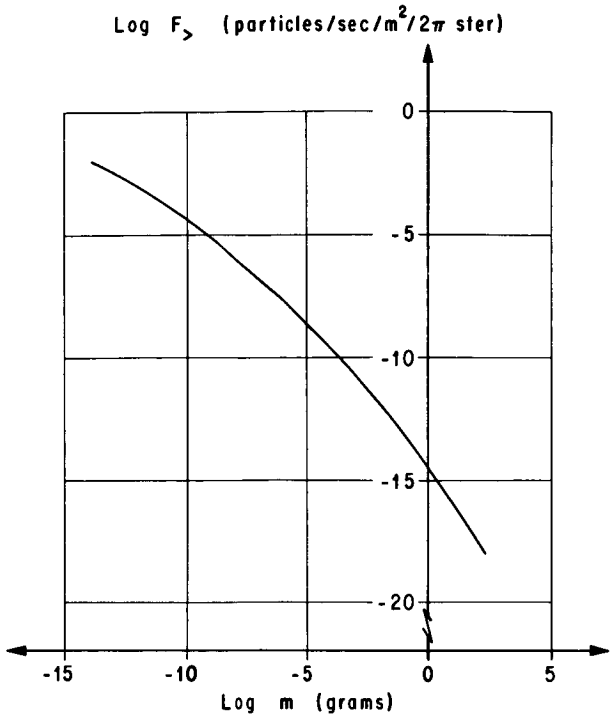

FIGURE 4. METEOROID MASS CUMULATIVE TERRESTRIAL MEAN INFLUX

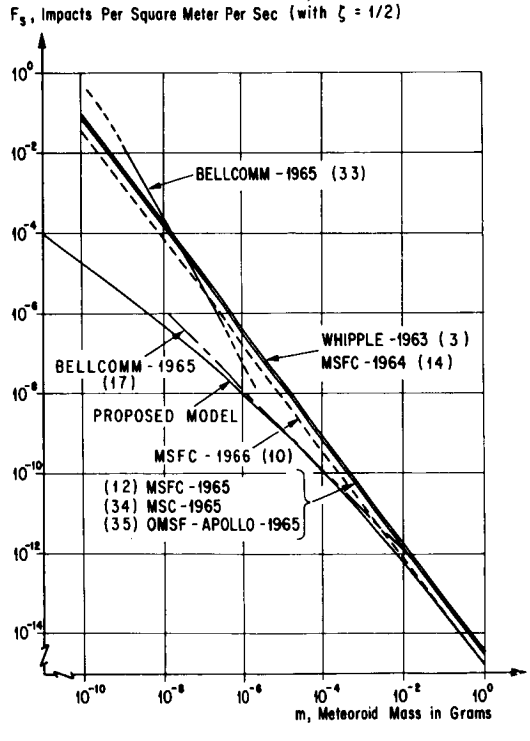

FIGURE 5. MEAN IMPACT FLUX OF METEOROIDS WITH MASS ≥ M FOR A RANDOMLY ORIENTED VEHICLE IN A NEAR EARTH ORBIT

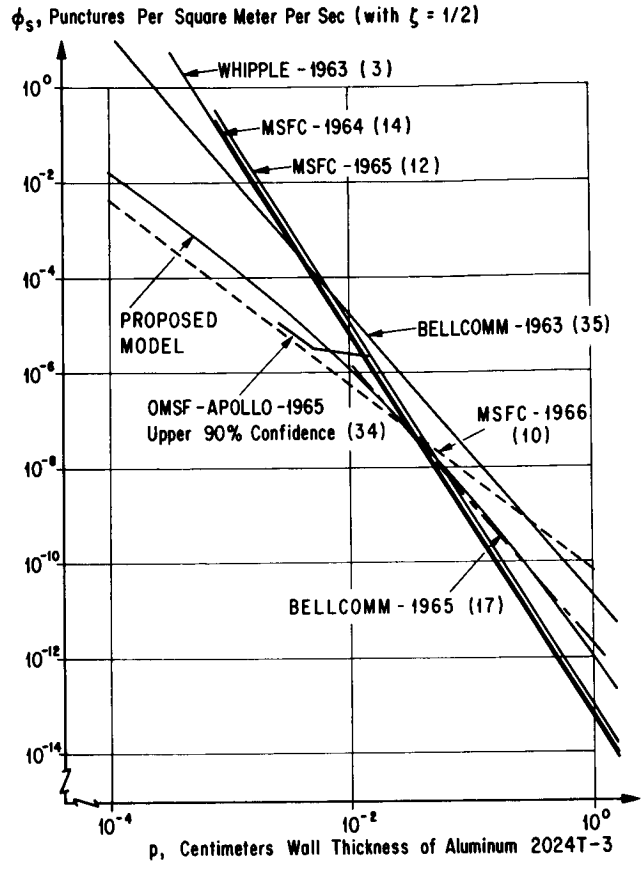

FIGURE 6. MEAN PUNCTURE FLUX FOR A RANDOMLY ORIENTED VEHICLE IN A NEAR EARTH ORBIT

II. EQUIVALENT PUNCTURABILITY

By Equation (11), if sheets of different materials must have the same meteoroid puncturability, then their target parameters must have the same value; i.e., $(10^{k_4} p)$ is invariant. For example, sheets of 2024-T3 aluminum must be 1.65 times as thick as for annealed Berylco 25 beryllium copper and 1.89 times as for $\frac{1}{2}$ hard AISI 302 stainless steel. But the necessary weight of aluminum is still less in either case, and soft aluminum (1100-H14) is nearly as effective as 2024T-3.

III. INTERPLANETARY SPACE

Most of the puncture hazard in cislunar space, and in interplanetary space near or between the orbits of Earth and Mercury, is due to particles of cometary rather than asteroidal origin. This follows from McCoy's [36] preference for Beard's [37] estimate that the flux of cometary particles should be proportional to $D^{-3/2}$, where D is the heliocentric distance in astronomical units, and from Parkinson's [38] model for the distribution of asteroidal particles with respect to mass m and distance D. For the flux of vehicle-puncturing asteroidal particles, Parkinson [38] preferred the extrapolation of Hawkins' [39] model for large stones, giving $10^{-15.93}\ m^{-1}$ particles per square meter per second for the terrestrial influx. By this formula the flux of photographic meteor particles larger than 10^{-1} gram is nearly two orders of magnitude below the corresponding value from Figure 4. This result agrees with the observation of Whipple and Hawkins [40] and of Jacchia and Whipple [41] about the relatively great predominance of cometary particles in samples of photographic meteors. Then

$$F_{>} \sim D^{-3/2}. \tag{27}$$

The 27 kilometers per second median lunar impact velocity, for the distribution illustrated in Figure 2, is only slightly less than the heliocentric circular orbital velocity for the particular heliocentric distance. Anyway, it would seem appropriate to assume that, at any other heliocentric distance D, nominal closing velocity is proportional to $D^{-1/2}$; i.e.,

$$v = 27\ D^{-1/2}. \tag{28}$$

Then, by Equations (4) and (8), the thickness p of a target sheet nominally puncturable by a meteoroid of particular mass is proportional to $D^{-1/3}$; i.e.,

$$p \sim D^{-1/3}. \tag{29}$$

Also, by Equations (4) and (8), $p^3 \sim mv^2$; i.e., together with the result in Equation (28), it follows that the particle mass $\bar{m}$ nominally sufficient to puncture a particular target is

$$\bar{m} \sim D. \tag{30}$$

Therefore, puncture flux ϕ is changed not only by the factor $D^{-3/2}$ due to the change in the mass-cumulative flux $F_{<}$ (according to the model by McCoy [36] and Beard [37]) but also by the factor $D^{\partial(\log F_{<})/\partial \log m}$ $\simeq D^{-1}$. These two factors combine to give

$$\phi \sim D^{-5/2}. \tag{31}$$

Figures 3 and 4, with respective ordinates $\log \phi$ and $\log F_{>}$, presuppose that D = 1 astronomical unit. Then, by Equations (31) and (27), it is necessary to subtract 2.5 log D and 1.5 log D from the ordinates of Figures 3 and 4, respectively, for applicability to other heliocentric distances D.

At heliocentric distances very much beyond the orbit of the Earth, the meteoroid hazard should be calculated separately for cometary and asteroidal populations of particles. The results for the cometary particles, adjusted with respect to D as already described in this section, are applicable in interplanetary space near or between the orbits of Mercury and Jupiter, except that for close orbits around Jupiter it is necessary to account for the significant effects of the gravitational field of the planet.

Because of the relative sparsity of the asteroidal meteoroids in the terrestrial influx, pertinent information about this population is less substantial. The nominal closing velocity will be assumed to be the same as is given as a junction of D in Equation (28). It seems appropriate for the vehicle-puncturing asteroidal particles to follow Parkinson's [38] extrapolation of Hawkins' [39] model for the terrestrial cumulative influx of stones, $10^{-15.93}\ m^{-1}$ particles per square meter per second. Parkinson [38] preferred the following flux enhancement factors for these particles with respect to heliocentric distance: 1.0, 2×10^3, 3×10^4, and 20 for the orbits of Earth, Mars, asteroids (at 2.5 AU point of max.), and Jupiter, respectively. The Jovian and terrestrial gravitationally enhanced flux factors, for these asteroidal particles, were given by Parkinson [38] as 170 and 2.1, respectively. Öpik [42] gives the average density of meteoritic stone as $\rho = 3.4$. It is expected that a somewhat less dispersion of density for these particles may be just about equally compensated by a somewhat greater dispersion of closing velocity, so that the dispersion of the mass just sufficient to puncture a given target sheet may be essentially the same as for the cometary particles. Then the value of the puncture flux enhancement factor given in Equation (9) should be valid for both populations.

IV. CONCLUSIONS

When a meteoroid impact target of interest is the puncturable equivalent of a sheet p centimeters

thick of a material with specific gravity ρ_t and sonic velocity C_t kilometers per second, it has a material constant k_4, a target parameter $k_4 + \log p$, and is just puncturable under average impact circumstances by a meteoroid with mass $\bar{m}$ at heliocentric distance D astronimical units; i.e.,

$$k_4 = (2/3) \log (\rho_t C_t) - 1.162 \qquad (12)$$

$$\bar{m} = 10^{3k_4 - 0.678} p^3 D. \qquad (11\text{-}30)$$

In cislunar space, except for Earth or moon reduction of the solid angle of exposure to a celestial hemisphere, the mean flux of primary meteoroids is nearly independent of distance beyond low orbital altitude and is reduced by only about 25 percent out to the boundary of the earth's gravitational dominance.

For a surface with 2Π steradian exposure, the flux $F_>$ of particles with mass exceeding $\bar{m}$ in Equation (11) is 0.63 order of magnitude below the puncture flux ϕ, because of the statistical variation of the particle material density, velocity, and angle of impact; i.e.,

$$F_> = 10^{-0.63} \phi. \qquad (26)$$

The mean puncture flux ϕ per second per square meter per 2Π steradian exposure is related to the target parameter $k_4 + \log p$ by

$$\log \phi = -12.95 - 4.02(k_4 + \log p) - 0.424(k_4 + \log p)^2$$
$$-0.025(k_4 + \log p)^3 - 2.5 \log D. \qquad (25\text{-}31)$$

The result for Equations (25) and (26) are illustrated graphically in Figure 3 and 4 for a unit value of D. All the values for mass-cumulative flux $F_>$ and puncture flux ϕ by the curves in these two figures are thought to be accurate to within a factor 2 probable error (normal distribution), and constitutes the primary-meteoroid flux and puncture models proposed for use in design and operations planning in MSFC programs for Earth-orbit, cislunar and interplanetary space near or between the orbits of Earth and Mercury.*

In interplanetary space much beyond the orbit of the Earth, it is appropriate to consider that the puncture hazard is due separately to the cometary and asteroidal populations of particles. The results for the cometary particles, adjusted with respect to D as already described in this and the preceding sections, are applicable in interplanetary space near or between the orbits of Mercury and Jupiter, except that for close orbits around Jupiter it is necessary to account for the significant effects of the gravitational field of the planet. The best available description of the asteroidal particle environment is given in the preceding section.

REFERENCES

1. Dalton, C. C.: Cislunar Meteoroid Impact and Puncture Models With Predicted Pegasus Satellite Punctures. NASA TM X-53187, 1965.

2. Dalton, C. C.: Statistical Analysis of Photographic Meteor Data, Part IV: Opik's Luminous Efficiency and Supplemented Hawkins-Upton Weighting. NASA TM X-(Being prepared for publication about September, 1966).

3. Whipple, F. L.: "On Meteoroids and Penetration," The Journal of the Astronautical Sciences, Vol. X, No. 3, pp. 92-94, Fall 1963.

4. U. S. Standard Atmosphere, 1962. National Aeronautics and Space Administration, United States Air Force, United States Weather Bureau, December 1962, Government Printing Office, Washington, D. C.

5. Mizner, R. A., Champion, K. S. W., and Pond, H. L.: The ARDC Model Atmosphere, 1959. Air Force Cambridge Research Center, Technical Report 59-267, Air Force Surveys in Geophysics No. 115, August 1959.

6. Opik, E. J.: The Masses of Meteors. Memoires de la Societe Royale des Sciences de Liege, 4th Series, No. 15, pp. 125-146, 1955.

7. Reismann, H., Donahue, J. D., and Burkitt, W. C.: Multivariable Analysis of the Mechanics of Penetration of High Speed Particles. Martin-Marietta Corporation, Interim Technical Progress Report, NASA CR-04-5, NASA Hq. Contract No. NAS7-219, 10 June 1964.

* Example. The flux values computed from Equations (25) and (26) are statistically nominal for the mean flux. To obtain the 99.86 percent one-sided confidence value for the mean flux (3 standard deviations from the nominal value), multiply by $3(2/0.6745) \simeq 9$.

8. Andriankin, I., and Stepanov, Yu. S.: Impact Penetration Depth of Meteoric Particles. Artificial Earth Satellites, Vol. 15, pp. 45-53, January 1964.

9. Herrmann, W., and Jones, A. H.: Survey of Hypervelocity Impact Information. Aeroelastic and Structures Research Laboratory, Massachusetts Institute of Technology, Report No. 99-1, September 1961.

10. Dalton, C. C.: Meteoroid Flux and Puncture Models. Working Paper #R-AERO-Y-77-66, Marshall Space Flight Center, January 26, 1966.

11. Dalton, C. C.: Theoretical Relationships for Meteoroid Puncture Experiments. NASA TND-3244, 1966.

12. Smith, R. E.: Space Environment Criteria Guidelines for Use in Space Vehicle Development, 1965 Revision. NASA TM X-53273, 1965.

13. Dalton, C. C.: Estimation of Tolerance Limits for Meteoroid Hazard to Space Vehicles... . NASA TN D-1996, 1964.

14. Dalton, C. C.: A Meteoroid Flux and Puncture Model for Near-Earth and Cislunar Space. Aero-Astrondynamics Research and Development Research Review No. 1, NASA TM X-53189, pp. 96-99, 1 October 1964.

15. Bjork, R. L.: Meteoroids versus Space Vehicles. ARS Journal, Vol. 31, No. 6, pp. 803-807, June 1961.

16. Summers, J. A.: NASA TN D-94, October 1959.

17. Dohnanyi, J. S.: The Meteoroid Environment of the Apollo Program. TR-65-211-5, August 30, 1965, Task 11, Contract NASw-417, Bellcomm, Inc., Washington, D. C.

18. Burbank, P. B., Cour-Palais, B. G., and McAllum, W. E.: A Meteoroid Environment for Near-Earth, Cislunar, and Near-Lunar Operations. NASA TN D-2747, April 1965.

19. Baumeister, T., Ed.: Mechanical Engineers' Handbook. McGraw-Hill Book Co., Inc., 1958.

20. D'Ans, J., and Lax, E.: "Taschenbuch für Chemiker Und Physiker," Springer-Verlag, Berlin, 1943.

21. The International Dictionary of Applied Mathematics. D. Van Nostrand Co., Inc., New York, 1960.

22. Hastings, E. C., Jr.: The Explorer XVI Micrometeoroid Satellite Description and Preliminary Results ... . NASA TM X-810, February 1963.

23. O'Neal, R. L.: The Explorer XXIII Micrometeoroid Satellite Description and Preliminary Results for the Period November 6, 1964 through February 15, 1965. NASA TM X-1123, August 1965.

24. Haussler, J. B., and Benson, R. H.: Saturn SA-9/Pegasus A Postflight Trajectory. NASA TM X-53251, 30 April 1965.

25. Haussler, J. B., and Benson, R. H.: Saturn SA-8/Pegasus B Postflight Trajectory. NASA TM X-53309, 2 August 1965.

26. Haussler, J. B., and Benson, R. H.: Saturn SA-10/Pegasus C Postflight Trajectory. NASA TM X-53340, 30 September 1965.

27. Hastings, E. C., Jr.: The Explorer XVI Micrometeoroid Satellite Supplement III... . NASA TM X-949, March 1964.

28. Stuhlinger, E.: Meteoroid Measurements with Project Pegasus. December 2 Reprint of Presentation at the Northeast Electronics Research and Engineering Meeting, Boston, November 4, 1965.

29. Naumann, R. J.: Pegasus Satellite Measurements of Meteoroid Penetration (Feb. 16-July 20, 1965). NASA TM X-1192, December 1965.

30. Aerospace Structural Metals Handbook. Vol. I: Ferrous Alloys. Second ed. March 1965, Project No. 7381, Task No. 738103, Contract No. AF33(615)-1184, Air Force Materials Laboratory, Research and Technology Division, Air Force Systems Command, Wright Patterson Air Force Base, Ohio.

31. Berylco 25s. Alloy Digest. Engineering Alloys Digest, Inc., Upper Montclair, New Jersey, November 1952.

32. Wikle, K. G., and Alspach, L. D.: Beryllium-Copper Alloys. Machine Design, pp. 154-171. 16 July 1964.

33. Dohnanyi, J. S.: The Micrometeoroid Environment of Project Apollo, Report No. TR-65-211-2, Task 11, Contract NASw-417, Bellcomm, Inc., Washington, D. C., 25 February 1965.

34. Natural Environment and Physical Standards for the Apollo Program. Report No. M-DE 8020.008 B, SE 015-001-1, NASA-OMSF, Washington, D. C., April 1965.

35. Orrok, G. T.: The Meteoroid Environment of Project Apollo. Bellcomm, Inc., Washington, D. C., 31 January 1963.

36. McCoy, T: MSFC Contract NAS 8-2550, Northrop, presented June 14, 1962.

37. Beard, D. B.: Interplanetary Dust Distribution. Astrophysical Journal, Vol. 129, No. 2, pp. 496-506, March 1959.

38. Parkinson, J.: MSFC Contract NAS 8-11285, Aerojet-General, presented May 26, 1965.

39. Hawkins, G. S.: Impacts on the Earth and Moon. Nature Magazine, Vol. 197, No. 4869, pp. 781, February 23, 1963.

40. Whipple, F. L., and Hawkins, G. S.: Meteors. Handbuch der Physik, Vol. 52, pp. 517-564, Springer-Verlag, Berlin, 1959.

41. Jacchia, L. G. and Whipple, F. L.: Precision Orbits of 413 Photographic Meteors. Smithsonian Contributions to Astrophysics, Vol. 4, No. 4, Smithsonian Institution, Washington, D. C., 1961.

42. Öpik, E. J.: Physics of Meteor Flight in the Atmosphere. Interscience Tracts on Physics and Astronomy No. 6, the Interscience Pub., Inc., New York, 1958.

ON RADIATION PRESSURE AND ITS EFFECTS ON SATELLITE MOTION

By

W. H. Heybey

SUMMARY

The pressure of light falling on a plane surface is bound up with the time-averaged stress prevailing in the moving electromagnetic field. A pressure expression for elemental surfaces inclined to parallel light is derived with the stipulation that the photoelectric effect is absent. Other losses (through transmission and absorption) are briefly discussed. Finite surfaces are supposed to be given in analytic terms; a method is described for finding the light force acting on them, and its point of attack. The motion of a satellite, otherwise undisturbed, under the impact of light is investigated in general. An application to an orbiting cylinder illustrates the methods.

I. EXPERIMENTAL AND THEORETICAL BASIS

As a natural phenomenon the mechanical force accompanying the incidence of light is observed and measured with the use of a torsional balance (See [1], pp. 556-557). It is found to be very small; however, over sufficiently long periods of time, it may produce unwanted disturbances in the motion of satellites subject to rigid attitude requirements as, for example, those of an orbiting telescope whose line of vision should remain fixed within 0.1 of an arc of a second or less in current estimates.

Theoretical expressions for the radiation pressure are derived in many treatises on optics or theoretical physics. In one way or another, the argument is mostly from the standpoint of the electromagnetic theory. One notable exception is that of Drude [2], pages 488-491, where the proof is based on the general energy principle and thus avoids the conceptual difficulty inherent in field-body interaction. Since the demonstration has to rely on light energy converted into heat energy by an ideally black body, it cannot very well be adapted to reflecting surfaces and will not be used in what follows.

Most of the textbooks readily accessible to the author restrict the case to light striking the surface at a right angle which is an exceptional incidence. None of them presents a direct and cogent derivation for surfaces slanted to light direction. It will be carried out here in order to support the easy generalization usually adopted, which is open to discussion if closely looked at. Reservations to be made will appear at several places, as will the need to average.

One may start with the complete set of Maxwell's equations (including boundary conditions) written down for a nonconducting medium:

$$\left.\begin{aligned} \frac{1}{c}\frac{\partial \underline{D}}{\partial t} &= \nabla \times \underline{H} \\ \frac{1}{c}\frac{\partial \underline{B}}{\partial t} &= -\nabla \times \underline{E} \\ \nabla \cdot \underline{D} &= 4\pi\rho \\ \nabla \cdot \underline{B} &= 0 . \end{aligned}\right\} \qquad (1)$$

If the medium is isotropic and homogeneous, as we will and can assume here, the vectors $\underline{D}$ and $\underline{B}$ are related to the electric ($\underline{E}$) and magnetic ($\underline{H}$) field strengths by the equalities

$$\underline{D} = \epsilon \underline{E}, \quad \underline{B} = \mu \underline{H} \qquad (2)$$

where the dielectricity coefficient and the permeability are constants.

Sunlight falling on a metallic surface will liberate electrons from it, especially in empty space where the ultraviolet part of the radiation is strong. The surface charge (density ρ) thus created will interfere with the electromagnetic field, and some of the light energy will be lost in photoelectric work. For both reasons the surface density will be disregarded ($\rho = 0$), so that $\nabla \cdot \underline{E}$ is considered as zero everywhere.

With these limitations equation (1) can be rearranged to give

$$\frac{\epsilon\mu}{c^2}\frac{\partial^2 \underline{E}}{\partial t^2} = \Delta \underline{E} \qquad (3)$$

and thus assumes the form of the wave equation. In a vacuum ($\epsilon = \mu = 1$) the propagation velocity of the wave is given by the constant c which will be

regarded as known. After a solution is established to equation (3), the associated wave motion of the magnetic vector $\underline{H}$ follows from the second Maxwellian equation where $\underline{B} = \mu \underline{H}$.

If a rectangular Cartesian system is used (unit vectors on the x,y,z-axes: i, j, k), a particular solution of equation (3) can be set down as

$$\underline{E} = A_E \cos 2\pi\left(\frac{t}{T} - \frac{z}{\lambda}\right) i \equiv E_1 i. \qquad (4)$$

It satisfies the boundary condition ($\nabla \cdot \underline{E} = 0$, here $\partial E_1/\partial x = 0$) and represents a plane wave with the z-axis as its normal. In an isotropic medium this normal is in the direction of the energy transmission; i.e., it gives the ray direction. The wave length, λ, and period, T, are linked to the ray propagation velocity by the relation

$$\frac{\lambda}{T} = \frac{c}{\sqrt{\epsilon \mu}} .$$

One of the quantities λ and T' can be chosen arbitrarily.

The second Maxwellian equation can now be integrated to give

$$\underline{H} = A_E \sqrt{\frac{\epsilon}{\mu}} \cos 2\pi\left(\frac{t}{T} - \frac{z}{\lambda}\right) j \equiv H_2 j. \qquad (5)$$

The wave form and motion are that of the $\underline{E}$-wave; but the amplitude

$$A_H = \sqrt{\frac{\epsilon}{\mu}}\, A_E$$

is equal to the electric amplitude A_E only if $\epsilon = \mu$, in particular, if the electromagnetic wave moves in a vacuum.

With this solution the electric and magnetic field vectors are in the x- and y-directions, respectively, and the ray direction is normal to both.

Plane wave motion can be said to prevail if a vehicle travels far enough from the sun to be subject to virtually parallel radiation. This assumption will be adopted as a further limitation. The force acting on a surface element, dS, can then be obtained with the use of the integrals (4) and (5). It can be computed from the electromagnetic stress in the medium or, rather, in the ether underlying it in Faraday's and Maxwell's view.

If, in general,

$$\underline{E} = iE_1 + jE_2 + kE_3,$$

the nine components of the electric stress tensor are known to be

$$\left.\begin{aligned} X_x &= \frac{\epsilon}{8\pi}\left(-E_1^2 + E_2^2 + E_3^2\right) \\ Y_y &= \frac{\epsilon}{8\pi}\left(E_1^2 - E_2^2 + E_3^2\right) \\ Z_z &= \frac{\epsilon}{8\pi}\left(E_1^2 + E_2^2 - E_3^2\right) \\ Y_z &= Z_y = -\frac{\epsilon}{4\pi} E_2 E_3 \\ Z_x &= X_z = -\frac{\epsilon}{4\pi} E_3 E_1 \\ X_y &= Y_x = -\frac{\epsilon}{4\pi} E_1 E_2 \end{aligned}\right\} . \qquad (6)$$

In the case of the plane wave (4), all the shear components are zero ($E_2 = E_3 = 0$), while the normal components add up to the stress vector

$$\underline{P}_E = \frac{\epsilon}{8\pi} E_1^2 (-i + j + k) .$$

Expressions (6) also define the magnetic stress tensor, when the E_i are replaced by the corresponding quantities H_i. The evaluation in terms of the wave (5) for which $H_3 = H_1 = 0$ yields

$$\underline{P}_H = \frac{\mu}{8\pi} H_2^2 (i - j + k) .$$

Both the field stresses $\underline{P}_E$ and $\underline{P}_H$ are periodic functions of time. The radiation pressure to be computed from them becomes comparable to the constant found experimentally by taking the average over a period. Since

$$\frac{1}{T}\int_0^T \cos 2\pi\left(\frac{t}{T} - \frac{z}{\lambda}\right) dt = \frac{1}{2} ,$$

$$(E_1^2)_{av} = \frac{1}{2} A_E^2 , \quad (H_2^2)_{av} = \frac{1}{2}\frac{\epsilon}{\mu} A_E^2 .$$

Thus, the two stress vectors combine to a common average

$$\underline{P} = (\underline{P}_E)_{av} + (\underline{P}_H)_{av} = \frac{\epsilon}{8\pi} A_E^2 k . \qquad (7)$$

This expression holds for any values of ϵ and μ.

Since the energy density at a given point in the (time-dependent) electromagnetic field of the waves (4) and (5) may be written as

$$\frac{\epsilon E_1^2 + \mu H_2^2}{8\pi} ,$$

its average value is found as $\frac{\epsilon}{8\pi} A_E^2$ and gives the magnitude of the average stress vector. For short, we may put

$$\frac{\epsilon A_E^2}{8\pi} = p_o \qquad (8)$$

and

$$\underline{P} = p_o k. \qquad (9)$$

The quantity A^2_E is proportional to the light intensity. In polychromatic sunlight it depends on the wave length and should be regarded, in formula (8), as an average taken over the spectrum.

Expression (9) shows that the stress in the particular electromagnetic field chosen is parallel to the light rays. The quantity p_o has the dimension of a pressure ($\frac{\text{energy}}{\text{volume}} = \frac{\text{force}}{\text{area}}$), and will shortly be taken as a mechanical pressure. Strictly speaking, it cannot be fully understood in what way a stress existing in the ether (i.e., the void) could give rise to a ponderomotive force; observation only can suggest that it does so*.

Consider a light beam of cross-sectional area dS_o (Fig. 1). At any point (A or A') in it, the opposite stresses $\underline{P}$ and $-\underline{P}$ are active. Let the light at A be intercepted by a cross-sectional material surface. An open face of the stressed ether is then created, one of the stresses is freed, and the force

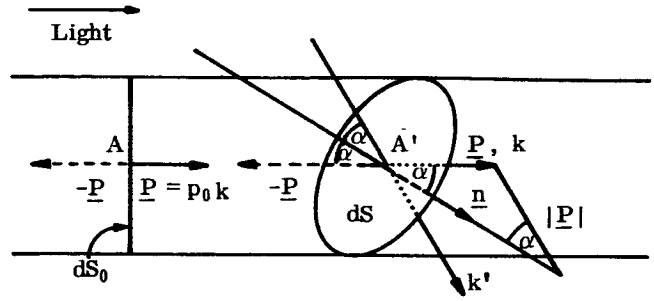

FIGURE 1. STATICS OF THE LIGHT FORCE ACTING ON PLANE ELEMENTAL SURFACES

$$\underline{F} = p_o \, dS_o \, k$$

is attacking the surface. Since it is normal to it, p_o can be interpreted as the pressure on the surface exerted by the force $\underline{F}$.

Regarding sunlight, the radiation pressure p_o at the outer fringes of the atmosphere has been determined as

$$p_o = \frac{1.374 \times 10^6}{c} \quad \frac{\text{dyne}}{\text{cm}^2} . \qquad (10)$$

This figure depends on the distance of the Earth from the sun and is slightly different at perihel and aphel. The significant coefficient varies between 1.351 and 1.397 (See [4], p. 4). For satellites moving in near-Earth orbits, one will often take the average value used in formula (10). The constant c ($\approx 3.10^{10}$) is the measure of the vacuum light speed in cm/sec.

The radiation force on the whole Earth (assumed as a perfectly absorbing body) equals the weight of 5.7×10^7 kg while the sun's attracting force corresponds to $3.6 \simeq 10^{21}$ kg [5]. The insignificance of the radiation force is apparent. On the other hand, in the interior of fixed stars where the light intensity is immense, radiation may outweigh gravitation (Eddington).

The force $\underline{F}$, as an outcome of the stressed state of the ether, is characteristic for it and cannot change either magnitude or direction if the beam is terminated by any arbitrary cut-off surface dS (at A', Fig. 1).* The force on dS may be given the form

$$\underline{F} = pdSk \qquad (11)$$

---

* M. Planck [3] after commenting on this point goes on to say that a similar difficulty exists in trying to visualize energy flow through a vacuum.

* If light behaved like a Newtonian fluid, the normal component only of $\underline{F}$ would act on dS.

where p is the pressure on dS. It follows that

$$p = p_o \frac{dS_o}{dS} .$$

For any two plane surfaces lying in parallel projection, the product of the area with the cosine of the angle the surface normal makes with the projecting direction is constant. Thus, $dS_o = dS \cos \alpha$ and

$$p = p_o \cos \alpha . \qquad (12)$$

It appears that if the surface is illuminated under the angle of incidence, α, the pressure on it is the fraction $p_o \cos \alpha$ of the basic pressure p_o.

If perfect reflection is assumed (ideally smooth surface, no transmission, no transformation of energy), the outgoing light will have the same intensity as the incoming light (p_o remains unaltered). With plane waves the reflection angle is equal to the angle of incidence, so that the force, $\underline{F}^{(r)}$, caused by reflection will point in the direction marked k' in Figure 1. The total force combining incidence and reflection,

$$\underline{F}_{total} = \underline{F}^{(i)} + \underline{F}^{(r)} = p_o \cos \alpha \, dS \, (k + k'),$$

is in direction of the vector

$$\underline{t} = k + k' .$$

Since k and k' are of equal length, $\underline{t}$ is normal to the surface (pointing toward the interior). The magnitude $|\underline{t}|$ is found from the trigonometric sine-theorem:

$$|\underline{t}| = \frac{\sin (\pi - 2\alpha)}{\sin \alpha} = 2 \cos \alpha .$$

Thus, with $\underline{t} = |\underline{t}| \underline{n}$,

$$\underline{F}_t = 2 p_o \cos^2 \alpha \, dS \, \underline{n}. \qquad (13)$$

The basic pressure p_o is multiplied by $2 \cos^2 \alpha$.*

---

* The factor $\cos^2 \alpha$ connected with oblique incidence is mentioned in [6] (p. 616), where reflection is taken into account for normal incidence, too, so that p_o goes into $2p_o$. $\cos^2 \alpha$ is given for incident light alone in [1], p. 557. Ditchburn considers the normal component of the light force only.

Physical reality seldom offers even quasi-ideal circumstances. On striking a surface, light will partly be transformed into different energy species, partly be reflected, specularly or diffusely. The full value of p_o will rarely prevail even at first incidence (as soon as there is measurable transparency). The dependency of transmission and absorption on wave length and angle of incidence is studied in [4], where applications to a plane surface and to convex surfaces symmetric to incidence are also given (even to surfaces containing zones of different material). The purpose of the present paper does not permit limitation to preferred light directions; however, in view of the complexity of the corrections otherwise necessary, it seems advisable first to consider perfectly absorbing or perfectly reflecting surfaces only. Pertinent corrections to the pressure p_o can afterwards be incorporated into the expressions; the integration over the surface then will have to be stepwise as a rule. When scattering was to be considered, a more involved mathematical approach would have to be employed to account for the multitude of minute reflecting surface parts whose distribution, if taken at random, would make the process largely independent of incidence (aside from shadow profile changes).

II. THE FORCES EXERTED BY PARALLEL LIGHT ON A FINITE SURFACE

The light should radiate through an isotropic homogeneous medium (not necessarily through vacuum; expression (9) has been obtained with arbitrary values of ϵ and μ). Photoelectric effects must be disregarded. The surface is allowed to contain perfectly absorbing and perfectly reflecting portions which may be shaped and distributed at will.

For an easy description of optically different surface zones, it is advisable to replace the ordinarily Cartesian surface equation by a parametric representation of the surface points:

$$\begin{aligned} x &= x(\sigma, \tau) \\ y &= y(\sigma, \tau) \qquad (14) \\ z &= z(\sigma, \tau) . \end{aligned}$$

Each of the variables σ and τ will move within a certain "natural" interval for the system (14) to define either the whole surface or any of its parts in the

Cartesian system. In the (σ, τ)-plane the surface will usually appear as a rectangle; its parts may be odd-shaped areas, in which case the limits of one natural interval will vary when the other variable moves in its own interval.

The local interior surface normal, a basic requisite, can be introduced through the unit vector

$$\underline{n} = in_1 + jn_2 + kn_3$$

in its direction. The components n_i follow from the system (14) through the relations

$$n_1 = \pm \frac{1}{N} \begin{vmatrix} y_\sigma & z_\sigma \\ y_\tau & z_\tau \end{vmatrix}, \quad n_2 = \pm \frac{1}{N} \begin{vmatrix} z_\sigma & x_\sigma \\ z_\tau & x_\tau \end{vmatrix},$$

$$n_3 = \pm \frac{1}{N} \begin{vmatrix} x_\sigma & y_\sigma \\ x_\tau & y_\tau \end{vmatrix} \qquad (15)$$

where the subscripts denote partial derivation with respect to the pertaining variable, and

$$N = \left| \sqrt{\begin{vmatrix} y_\sigma & z_\sigma \\ y_\tau & z_\tau \end{vmatrix}^2 + \begin{vmatrix} y_\sigma & x_\sigma \\ z_\tau & x_\tau \end{vmatrix}^2 + \begin{vmatrix} x_\sigma & y_\sigma \\ x_\tau & y_\tau \end{vmatrix}^2} \right| . \qquad (16)$$

Once the surface is known, it is an easy matter to decide on the sign pertinent to the interior normal. This vector and the unit vector

$$\underline{s} = is_1 + js_2 + ks_3$$

in light direction combine to define the angle of incidence, α, by their interior product:

$$\underline{n} \cdot \underline{s} = \cos \alpha . \qquad (17)$$

The elemental surface dS, a second requisite, is proportional to N:

$$dS = N \, d\sigma \, d\tau . \qquad (18)$$

The differentials $d\sigma$ and $d\tau$ should have the same sign here, so that both variables must be taken increasing (or decreasing) at the later integrations.

By expressions (11), (12), (17), and (18) the second order force differential acting on a perfectly absorbing elemental surface may be written as

$$d^2\underline{F}_a = p_o (\underline{n} \cdot \underline{s}) \, N \, d\sigma \, d\tau \, \underline{s} . \qquad (19)$$

(The light direction is now $\underline{s}$ rather than k).

With perfect reflection, equality (13) applies to give

$$d^2\underline{F}_t = 2p_o (\underline{n} \cdot \underline{s})^2 \, N \, d\sigma \, d\tau \, \underline{n} . \qquad (20)$$

While the vector $\underline{s}$ can be taken here as fixed relative to the surface, $\underline{n}$ and N depend on σ and τ. (On occasion, N may be found constant; $\underline{n}$ is so for the plane only.)

With a fully illuminated surface, the integrations extend over the natural intervals of σ and τ. Shadow zones will narrow them down. Such zones fall into two categories: tangential and cast.

Tangential incidence means that $\alpha = 90°$. Relation (17) tells that the tangential shadow boundary, s_t, is given by the equation

$$\underline{n} \cdot \underline{s} = 0. \qquad (21)$$

The cast shadow cylinder will be rooted on a line on the surface, either a sharp rim or a tangential shadow boundary (as, e.g., of an airplane fuselage casting a shadow on the wings). Let the line be given in the parametric form

$$x_c = f(\zeta), \quad y_c = g(\zeta), \quad z_c = h(\zeta) . \qquad (22)$$

The relevant generating lines of the shadow cylinder,

$$\frac{x - x_c}{s_1} = \frac{y - y_c}{s_2} = \frac{z - z_c}{s_3} , \qquad (23)$$

start at the line segment (or segments) grazed by rays. They may intersect with other portions of the body forming a cast shadow boundary, s_c, also to be traced on the (σ,τ)-diagram; it leads to further restriction of the integration interval, unless it lies wholly within the tangential shadow zone.

With bodies of complex description, the determination and use of proper integration limits may require painstaking detail work. Often the integrations will have to be numerical.

To know the force alone is insufficient information. Its point of attack (centroid) is also needed. To find it, one determines the arm of the force connecting a point, C, on the line of attack with a point of reference that may be chosen arbitrarily and will here be taken as the origin O.

Let $\underline{r}$ denote the vector leading from the origin to an elemental surface. The force attacking there has the second order moment

$$d^2\underline{M}^* = \underline{r} \times d^2\underline{F},$$

where $\underline{F}$ stands for either $\underline{F}_a$ or $\underline{F}_t$. The moment of the integrated force is equal to the integrated moment:

$$\underline{r}^* \times \underline{F} = \int_\sigma \int_\tau [\underline{r} \times d^2\underline{F}] \qquad (24)$$

where

$$\underline{r}^* = ix^* + jy^* + kz^* \qquad (25)$$

is the arm of the force $\underline{F}$ and as such defines $C(x^*, y^*, z^*)$. The integration limits above apply again. Equation (24) for the vector $\underline{r}^*$ leaves one of its components indeterminate, since a force can be moved along its line of attack without altering its moment. One may place the centroid at a convenient location on this line by introducing a suitable relationship

$$f(x^*, y^*, z^*) = 0. \qquad (26)$$

III. REACTION OF A BODY TO THE IMPACT OF LIGHT

For a limited time, an undisturbed satellite in Earth orbit will move at practically constant velocity along practically rectilinear path. A (ξ, η, ζ)-system through its mass center, G, will be equivalent to the original space-fixed system by the Galileo principle. Let us assume that at $t = 0$, the vehicle is at rest in (ξ, η, ζ).

The surface equation (14) has been set up in a body-fixed (x,y,z)-system ; the differentials (19) and (20) of the light force $\underline{F}$ must be integrated in it. The light direction $\underline{s}$ is constant in (ξ, η, ζ), or can safely be taken so. In (x,y,z), however, it is different with different attitudes of the body. Moreover, the shadow boundaries, and therefore the integration limits, will often be different. Each attitude requires a separate force computation.

Let the mass center G have the directed distance

$$\hat{\underline{r}} = \hat{x}i + \hat{y}j + \hat{z}k$$

from the origin O of the (x,y,z)-system. If the torque

$$\underline{M} = (\underline{r}^* - \hat{\underline{r}}) \times \underline{F} = M_x i + M_y j + M_z k \qquad (27)$$

of the force $\underline{F}$ is not permanently zero, the vehicle will begin turning about shifting axes through G, so that $\underline{F}$ will be varying. This motion can best be described when the axes of the principal moments of inertia intersecting at G are introduced as coordinate axes. If vector components in this second body-fixed system, Σ, are identified by the indices α, β, γ, the torque (27) and the vector $\underline{\omega}$ of the angular velocity which it causes to develop are related by the Eulerian equations

$$\left.\begin{aligned} M_\alpha &= T_a \frac{d}{dt}\omega_\alpha - \omega_\beta \omega_\gamma (T_b - T_c) \\ M_\beta &= T_b \frac{d}{dt}\omega_\beta - \omega_\gamma \omega_\alpha (T_c - T_a) \\ M_\gamma &= T_c \frac{d}{dt}\omega_\gamma - \omega_\alpha \omega_\beta (T_a - T_b) \end{aligned}\right\} \qquad (28)$$

where T_a, T_b, and T_c are the principal moments of inertia. The torque components, M_α, M_β, M_γ, follow from M_x, M_y and M_z by the transformation equations connecting the two body-fixed systems.

The integration of the set (28) can be carried out independently of the translatory motion of the mass center, yet it remains laborious nonetheless. (1) Finding the angular velocity $\underline{\omega}$ prevailing at the end of a step is not enough. A second set of equations relating the $\underline{\omega}$-components to the first order time-derivatives of the Eulerian angles must be solved to obtain the instantaneous values of these angles and thus the body's attitude in (ξ,η,ζ) at the beginning of the next step. Then one has (2) to determine $\underline{s}(x,y,z)$, (3) to use $\underline{s}$ for finding the shadow boundaries and integration limits, (4) to carry out the force quadrature, (5) to establish the instantaneous centroid $(\underline{r}^*)$, (6) to compute the vector $\underline{M}$, and (7) to compute its components in the system Σ. After this, one is ready to proceed by Δt in the step calculation as it was set up.

Since control will not permit major deviations from an original attitude, the working out of this scheme does not seem to be warranted. It will suffice to consider an initial period in which the system Σ barely is shifting and which might be quite long since p_o is extremely small. The vectors $\underline{F}$ and $\underline{M}$ will then essentially retain the values they had at $t = 0$. The subtractive terms in the set (28), as small of second order, can be neglected; the solution follows as

$$\underline{\omega} = \left(\frac{M_\alpha}{T_a} i' + \frac{M_\beta}{T_b} j' + \frac{M_\gamma}{T_c} k'\right) t, \qquad (29)$$

where i', j', k' are unit vectors on the axes of the principal moments of inertia. This expression defines the direction of the initial axis of the rotation about G and shows that $\underline{\omega}$ increases linearly with time during the initial period.

Untouched by the rotation process as such, the mass center G will move relative to the (ξ,η,ζ)-system. Newton's translation equation

$$|\underline{F}| = m\frac{d^2s}{dt^2}$$

(m: body mass; s: distance covered in force direction) cannot be solved, however, without regress to the rotatory equations which are to provide the discrete values of $\underline{F}$ needed for the necessarily stepwise integration. With $\underline{F}$ = const. in the initial period the translational velocity, like the rotational, is a linear function of time.

IV. PRESSURE FORCES ON A RIGHT CIRCULAR CYLINDER

The cylinder, as an approximation to an orbiting telescope, may be considered a fitting body to illustrate the computational methods. It is assumed that its surface material is either totally absorbing or totally reflecting and that the lens end always points away from the sun. If the top of the cylinder (Fig. 2) is fitted with the optical objective, the light will have to arrive from below ($s_3 > 0$).

The curved part of the cylinder surface in Figure 2 is described by the system

$$\begin{aligned} x &= R\cos\tau \\ y &= R\sin\tau \\ z &= \frac{1}{2}L\sigma \end{aligned} \qquad (30)$$

where the natural ranges of the variables are

$$-1 \leqq \sigma \leqq +1$$

$$0 \leqq \tau \leqq 2\pi \quad .$$

From expressions (15) and (16)

$$\underline{n} = -i\cos\tau - j\sin\tau \qquad (31)$$

$$N = LR = \text{const.}$$

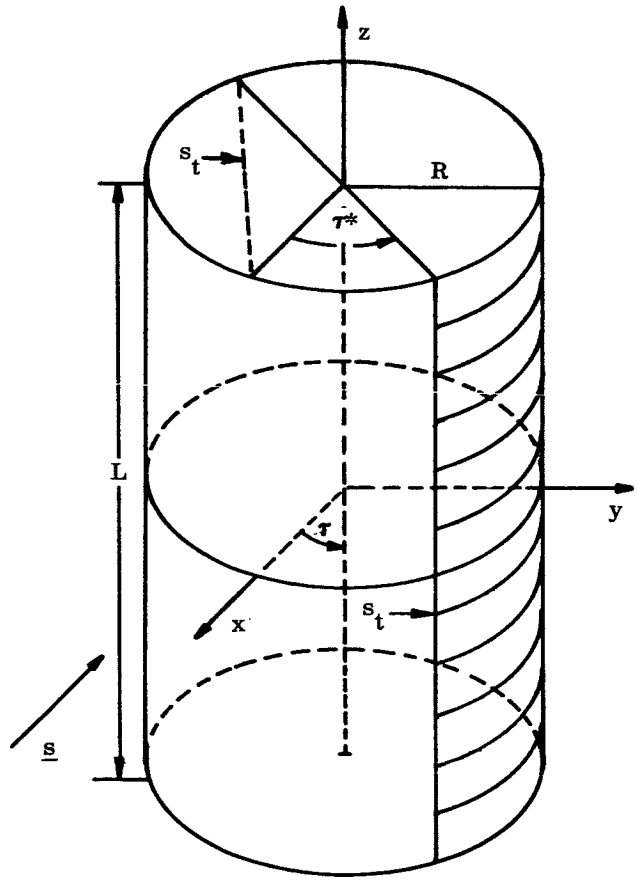

FIGURE 2. THE ILLUMINATED CYLINDER

Condition (21) then gives the tangential shadow boundary s_t at

$$\tan\tau_t = -\frac{s_1}{s_2} \quad . \qquad (32)$$

If the first of the solutions is $\tau_t = \tau^*$, the second will be $\tau_t = \tau^* - \pi$. Thus, the integration intervals are

$$\tau^* - \pi \leqq \tau \leqq \tau^*, \quad -1 \leqq \sigma \leqq 1 \text{ (unaffected)}.$$

There is evidently no shadow cast by either top or bottom rim on the otherwise illuminated surface half. The (double) line s_t is the only shadow boundary.

With perfectly absorbing surface material, the differential (19), on integrating over the proper intervals, gives

$$\underline{F}_{a,c} = 2p_o LR\sqrt{1 - s_3^2}\,\underline{s} \equiv C_a\,\underline{s},$$

where relation (32) has been used to convert trigonometric functions of τ^* into expressions involving s_1

and s_2. The index c indicates integration over the curved part of the surface. The force on the blunt end is

$$\underline{F}_{a,b} = p_o \pi R^2 s_3 \underline{s} \equiv B_a \underline{s} .$$

This result can be obtained with ease from $d^2\underline{F}_{a,b} = p_o (k \cdot \underline{s})\, dS$, the interior normal being $\underline{n} = k$.

The elemental forces $d^2\underline{F}_{a,c}$ have the arms

$$\underline{r} = ix + iy + kz$$

relative to the origin 0, where x, y, z are the coordinates (30). By expressions (19) and (31) the integrated moment becomes

$$\underline{M}^*_c = -p_o LR \int_{\sigma=-1}^{+1} \int_{\tau^*-\pi}^{\tau^*} \begin{vmatrix} i & j & k \\ R\cos\tau & R\sin\tau & \frac{1}{2}L\sigma \\ s_1 & s_2 & s_3 \end{vmatrix} (s_1\cos\tau + s_2\sin\tau)\, d\sigma\, d\tau$$

$$= -\frac{\pi}{2} p_o LR^2 s_3 (s_2 i - s_1 j).$$

The blunt end force $\underline{F}_{a,b}$ obviously attacks at the base circle's center ($\underline{r} = -\frac{1}{2} Lk$); its moment is

$$\underline{M}^*_b = \frac{L}{2} p_o \pi R^2 s_3 \begin{vmatrix} i & j & k \\ 0 & 0 & -1 \\ s_2 & s_2 & s_3 \end{vmatrix}$$

$$= \frac{\pi}{2} p_o LR^2 s_3 (s_2 i - s_1 j).$$

Since the forces have the combined moment zero, the arm of their resultant is $\underline{r}^* = 0$.* The centroid is at the origin ($C \equiv O$), i.e., at the geometric midpoint of the cylinder, which, with a homogeneous mass distribution, is the mass center as well. A solid (right circular) cylinder will experience no torque under parallel radiation if its surface is perfectly black.

If the surface is perfectly reflecting, integration of the differential (20) leads to

$$\underline{F}_{t,c} = \frac{8}{3} p_o LR \sqrt{1 - s_3^2}\, (is_1 + js_2) \equiv C_t (is_1 + js_2),$$

while the blunt end force becomes

$$\underline{F}_{t,b} = 2 p_o \pi R^2 k .$$

The line of attack of $\underline{F}_{t,c}$ is normal to the cylinder axis and will pass through O for symmetry reasons.* That of $\underline{F}_{t,b}$ is the cylinder axis itself. Thus, the centroid of the combined force again can be made to coincide with O; as above, the torque is zero with a homogeneous cylinder. The force direction, however, is no longer that of the incident light.

Suppose now that the cylinder is subdivided into compartments of rotational symmetry with respect to its axis, each filled with a homogeneous material different from that in the adjacent compartments. The T_c-axis will then be the z-axis. Since $T_b = T_a$ here, the remaining two principal axes can be taken as parallel to the x- and y-axes. The primed unit vectors are identical with i, j, k in these circumstances. Hence, the components of any vector have the same magnitude in the two body-fixed systems, so that the indices α, β, γ and x, y, z are interchangeable. The mass center, G, will be located on the z-axis at some distance, $z = z_o$, from the origin (and centroid; $O \equiv C$). Thus, $\underline{r} = z_o k$, while $\underline{r}^* = 0$. Expression (27) for the acting torque becomes

$$\underline{M} = -z_o [k \times \underline{F}] = z_o (iF_y - jF_x) = iM_\alpha + jM_\beta + 0.$$

The angular velocity (29) takes the form

$$\underline{\omega} = \frac{z_o}{T_a} (iF_y - jF_x) ,$$

which result holds for the initial period only as will be recalled. The symbol F is used either for F_a or for F_t. The x- and y-components of both these forces are proportional to s_1 and s_2. Thus, we may write

$$\underline{\omega} = \frac{z_o}{T_a} A (is_2 - js_1) = \frac{z_o}{T_a} A[\underline{s} \times k],$$

where A stands for $C_a + B_a$ or C_t, respectively. The initial axis of rotation is shown to be the normal through the mass center to the plane containing light direction and cylinder axis. From this position and attitude, it will slowly wander out in subsequent stages following the complex pattern set by the Eulerian equations.

* The use of equation (24) is not needed here.

* This can also be concluded from equation (24) where the right side can be shown to vanish.

The magnitude of the angular velocity, at any small t, is zero if $s_3 = 1$ ($\underline{s} = k$; light directly from below); otherwise it is the ratio

$$\frac{C_t}{C_a + B_a} = \frac{4}{3} \frac{L\sqrt{1 - s_3^2}}{L\sqrt{1 - s_3^2} + \frac{\pi}{2} R s_3},$$

which is largest (4/3) for $s_3 = 0$. Incidence normal to the cylinder axis causes somewhat faster initial rotation with a perfectly reflecting than with a perfectly absorbing surface. The ratio, however, decreases as s_3 increases, and soon the absorbing cylinder will exhibit the faster rotation. This trend reflects the fact that the component s_3, totally lost in curved-surface reflection, but effective in absorption, increases at the expense of s_1 and s_2 ($s_1^2 + s_2^2 = 1 - s_3^2$).

V. CONCLUSION

The force, its point of attack, and the initial motion under its impact can be determined, in basically the same way, for all surfaces whose parts are given in analytic terms, although the task is bound to grow wearisome with intricate shadow contours or multiple reflections in concave recesses.

A refinement would consider the losses in partially transparent and absorbing materials as far as experimental or theoretical data are available. In such cases, the total force element has to be written as

$$d^2\underline{F}_t = d^2\underline{F}^{(i)} + d^2\underline{F}^{(r)} = (p'_o k + p''_o k') \cos\alpha \, dS,$$

where both p'_o and p''_o are smaller than p_o. The compact expression (13) is no longer obtainable then. In [4], the absolute value

$$\Pi = |p'_o k + p''_o k'| = \sqrt{p'^2_o + p''^2_o + 2p'_o p''_o \cos 2\alpha}$$

is used to define a "light force coefficient" (C_F) by putting

$$\Pi = C_F p_o .$$

This coefficient moves between $C_F = 0$ (ideal transmission) and $C_F = 2$ (ideal reflection at $\alpha = 0°$). It represents one way of introducing a correction to the basic pressure p_o. Since p'_o and p''_o depend on α = arc cos ($\underline{n} \cdot \underline{s}$), the force quadrature is rather laborious even with simple surface and favorable incidence [4].

Other, and more fundamental, difficulties arise with light incident on rough, scattering materials or on metallic surfaces emitting electrons when struck. In both cases, the theoretical derivation of the force differential must be re-examined and will have to proceed on lines deviating in places from those followed so far.

VI. REFERENCES

1. Ditchburn, R. W.: Light. Interscience Publishers, New York.
2. Drude, P.: The Theory of Optics. Dover Publications, New York, 1959.
3. Planck, M.: Theorie der Elektrizitaet und des Magnetismus. S. Hirzel. Leipzig, 1928.
4. Holl, H. B.: The Effect of Radiation Force on Satellites of Convex Shape. NASA TN D-604, May 1961.
5. Schaefer, Cl.: Einfuehrung in die Theoretische Physik. Vol III.
6. Joos, G., and Freeman, I. M.: Theoretical Physics. Third ed., Blackie & Son, London-Glasgow.

VII. STRUCTURAL DYNAMICS

A DYNAMIC APPROACH OF FUEL SLOSHING PROBLEMS IN A SPACE VEHICLE

By

Frank C. Liu

SUMMARY

A dynamic approach to determination of the natural frequency of fuel sloshing in a space vehicle in flight is developed. This method enables us to couple directly the motion of the space vehicle resulting from fuel sloshing to the motion of the fuel. Hence, it yields a more realistic representation of the dynamic system than that given by the existing approach which links the motion of the vehicle and its fuel sloshing by means of a mechanical analogue or feedback.

I. INTRODUCTION

The force used to maneuver a space vehicle in flight is usually an impulse. To determine how the space vehicle responds to an impulse force, it is important to know precisely the natural frequency of the whole system as well as the dynamic coupling of the motion of the vehicle and the motion of the fuel in its container or containers. The existing approaches to this problem are as follows:

1. Mechanical Analogy. First, we analyze the motion of the fuel in the container, which rests on a fixed support, and determine the natural frequency of the sloshing. Then, the fuel tank system is converted to a mass-spring system by means of a mechanical analog to constitute a dynamic component of the space vehicle.

2. Feedback Approach. We impose a motion to the fuel tank and analyze the response of the fuel. Then, we determine the force created by the fuel sloshing and feedback to the vehicle to determine the response of the vehicle.

It is easy to see that neither of the two methods couples the space vehicle and the fuel sloshing directly.

II. THE DYNAMIC APPROACH

This new approach of solving sloshing problems of a space vehicle treats the vehicle and its fuel as one unit. First, let us show two examples to illustrate how the frequency of a simple pendulum is affected when it is attached to a free-moving support. We will have some idea about how the natural sloshing frequency of the fuel tank is affected by its free moving support.

Example 1. Let us attach the simple pendulum with mass m and length L to a mass M which is free to move horizontally in the plane of oscillation, as shown in Figure 1.

The natural frequency of the system can be determined easily by using Lagrange's method.

$$\omega = \sqrt{\left(1 + \frac{m}{M}\right)(g/L)} \qquad \text{rad./sec}$$

This shows that the frequency is increased by a factor $\sqrt{1 + m/M}$.

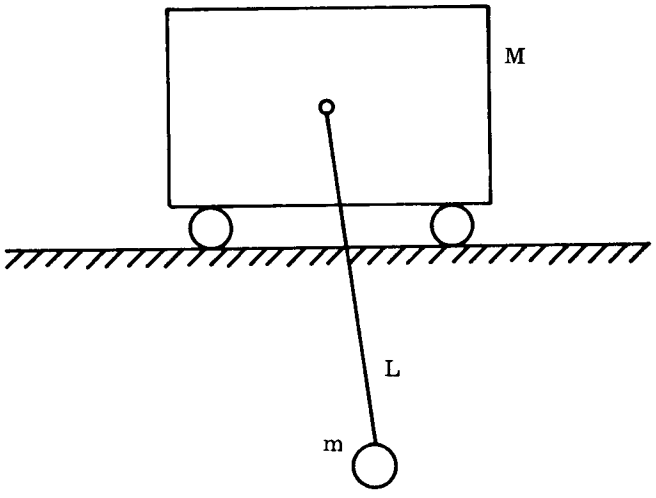

FIGURE 1. DIAGRAM OF EXAMPLE 1.

Example 2. To increase the freedom of the support further, let us make the support also free to rotate about its static center of gravity, as shown in Figure 2. Notice that a mass m is put at the opposite side of the axis of rotation to give a static balance of

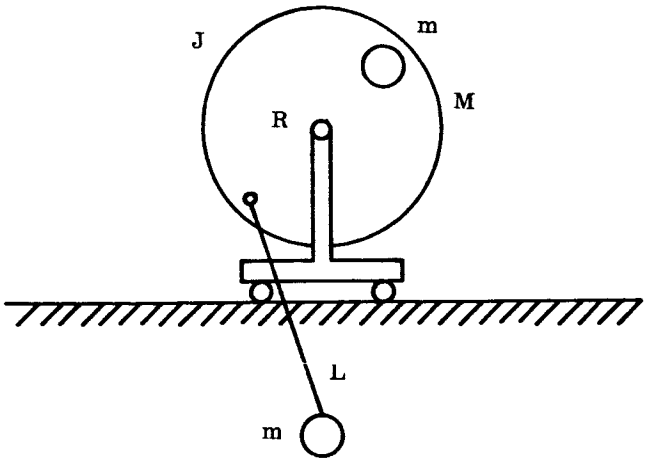

FIGURE 2. DIAGRAM OF EXAMPLE 2.

the system. Here M denotes the total mass of the support (stand, disc, and counter balance mass m), J is the moment of inertia of the disc with the balance mass m included, and R is the distance from the point where the pendulum is attached to the center of rotation. Now, the frequency of the system becomes

$$\omega = \sqrt{\left(1 + \frac{m}{M} + \frac{mR^2}{J}\right)(g/L)} \quad . \quad \text{rad./sec}$$

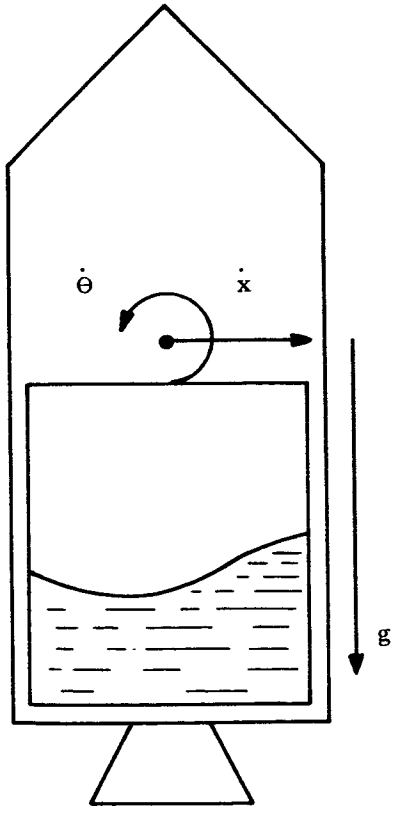

FIGURE 3. SPACE VEHICLE HAVING PARTIALLY-FILLED FUEL TANK.

Let us return to the space vehicle which has a partially filled fuel tank as shown in Figure 3. Because of its axial symmetry, only the motions $\dot{x}$ and $\dot{\Theta}$ are to be considered. During space flight the surface wave of the fuel becomes the only restoring force for the free vibration of the system. Usually the mass of the fuel forms a major portion of the total mass of a space vehicle. Thus, we may expect that the frequency of the vehicle is considerably higher than the frequency of sloshing in a fixed tank.

III. GENERAL PRINCIPLE

In an attempt to determine the velocity potential function of the fluid which is assumed incompressible and inviscous in a rigid, free moving cylindrical tank we found that under the linearized boundary conditions the coefficients of the potential function are directly related to $\dot{x}$ and $\dot{\theta}$. For small oscillations we may assume that $x = X_1 \sin\omega t$ and $\theta = X_2 \sin\omega t$ and use a one-term approximation for the potential function. Formulating the kinetic energy of the dry vehicle in terms of $\dot{x}$ and $\dot{\theta}$, and the kinetic and potential energies of the fluid in terms of the potential function results in the Lagrangian function of the system in the form

$$I = \tfrac{1}{2} X^T W X$$

where X is a column matrix with two elements X_1 and X_2, T denotes matrix transposition, and W is a 2 x 2 matrix. The elements of W are polynomials of ω, the natural frequency of the whole system. By Hamilton's Principle, I is an extremum when the determinant of W is equal to zero. Consequently, we can solve for ω numerically.

IV. CONCLUSION

This method has added advantage when it is used for a system which has more than one fuel tank. The dynamic coupling of all the tanks and the vehicle becomes a simple matter.

Digital computer programs for a vehicle with cylindrical tanks have been completed. The frequency of a vehicle of the Saturn class with one tank sloshing may be 5% higher than the fixed tank frequency. Work on the digital computer program for tanks with arbitrary shape is in progress. A technical report on this work will be available shortly.

WIND PENETRATION EFFECTS ON FLIGHT SIMULATIONS

By

James G. Papadopoulos

SUMMARY

Present six-degrees-of-freedom wind monitor Saturn Simulation programs assume an instantaneous constant wind velocity over the entire vehicle length. Contrary to this popular but simplified assumption, the study presented here indicates that wind penetration effects are not only desirable but necessary for any serious analysis of vehicle response to a wind profile.

Wind penetration effects are evaluated in the frequency domain by developing a solution for theoretical transfer functions. Numerical calculations are made for a Saturn SA-9 vehicle. Analytical transfer functions for angle-of-attack and average engine gimbal deflection are compared to a spectral analysis of actual flight test data.

LIST OF SYMBOLS

Symbol	Definition
a_0	Attitude control gain
a_1	Angular rate control gain, sec
A_L	Longitudinal acceleration, m/sec^2
A_m	Generalized net aerodynamic force at the m bending mode, Newtons
A_{mwp}	Generalized aerodynamic force due to wind penetration for the m bending mode, Newtons
$A_{m\mu}$	Generalized force term, Newtons
B_0	In-phase component of aerodynamic force due to a sinusoidal unit wind, Newton-sec/meter
B_1	Out-of-phase component of aerodynamic force due to a sinusoidal unit wind, Newton-sec/meter
C_0	In-phase component of aerodynamic moment due to a sinusoidal unit wind, Newton-sec
C_1	Out-of-phase component of aerodynamic moment due to a sinusoidal unit wind, Newton-sec
C_2	Unit gimbal deflection restoring moment divided by vehicle's mass moment of inertia, $1/sec^2$
C_{lx}	Aerodynamic lift gradient distribution
D_0	In-phase component of generalized aerodynamic force due to a sinusoidal unit wind, Newton-sec/meter
D_1	Out-of-phase component of generalized aerodynamic force due to a sinusoidal unit wind, Newton-sec/meter
D_T	Aerodynamic damping, 1/sec
F	Vehicle thrust, Newtons
F_{AERO}	Net aerodynamic force acting on the vehicle, Newtons
F_{AWP}	Aerodynamic force due to wind penetration, Newtons
$g_{B\mu}$	Viscous damping of the μ bending mode
g_2	Control accelerometer gain, $rad\text{-}sec^2/m$
G_A	Gimbal actuator transfer function
G_φ	Attitude control filter transfer function
$G_{\dot{\varphi}}$	Attitude rate control filter transfer function
G_γ	Control accelerometer transfer function

LIST OF SYMBOLS (Cont'd)

Symbol	Definition
G_μ	Aerodynamic force term, Newtons
$\bar{G}_\mu$	Aerodynamic moment term, Newton-meter
H_μ	Aerodynamic force term, Newtons
$\bar{H}_\mu$	Aerodynamic moment term, Newton-meter
i	Complex notation for $\sqrt{-1}$
I	Mass moment of Vehicle about center of gravity, Kg-m^2
I_E	Mass moment of inertia of gimbal engine about its center of gravity, Kg-m^2
J_0	Aerodynamic force term, Newton/rad
J_1	Aerodynamic moment term, Newton-meters/rad
J_2	Aerodynamic moment term, Newton-meter
$K_{m\mu}$	m generalized bending force term due to the μ bending mode, Newton/meter
L_E	Distance between gimbal point and engine center of gravity, meters
L	Vehicle length, meters
L( )	La Place operator
M	Vehicle mass, kg
M_{AERO}	Net aerodynamic moment acting at the vehicle's center of gravity, Newton-meter
M_{AWP}	Aerodynamic moment at the vehicle c.g. due to wind penetration, Newton-meter
M_E	Mass of gimbal engine, kg
$M_{B\mu}$	Generalized mass of the μ bending mode, kg
M_{Si}	Slosh mass of ith propellant, kg

LIST OF SYMBOLS (Cont'd)

Symbol	Definition
q	Dynamic pressure, Newtons/m^2
R	The real part of a complex number
s	Complex notation for $i\omega$, rad/sec
S	Reference surface area, $meters^2$
V	Vehicle velocity, m/sec
V_{WX}	Wind velocity along vehicle, m/sec
V_W	Amplitude of wind penetration, m/sec
x	Displacement along vehicle, meters
x_{CG}	Longitudinal center of gravity, meters
x_φ	Longitudinal location of attitude sensor
$\bar{x}_E$	Longitudinal location of gimbal engine center of gravity, meters
$\bar{x}_{Si}$	Longitudinal location of the ith slosh mass, meters
$y_{\mu x}$	Normalized μ bending mode displacement along the vehicle
$Y_{\mu E}$	Normalized μ bending mode displacement at the gimbal station
$y_{\mu\alpha}$	Normalized μ bending mode displacement at the angle-of-attack sensor
$y_{\mu\ddot{\gamma}}$	Normalized μ bending mode displacement at the accelerometer sensor
$y_{\mu\varphi}$	Normalized μ bending mode displacement at the attitude sensor
$y_{\mu\dot{\varphi}}$	Normalized μ bending mode displacement at the angular rate sensor
$y'_{\mu x}$	Normalized μ bending mode slope along the vehicle, 1/meter
$Y'_{\mu E}$	Normalized μ bending mode slope at the gimbal station, 1/meter
$y'_{\mu\alpha}$	Normalized μ bending mode slope at the angle-of-attack sensor, 1/meter
$y'_{\mu\ddot{\gamma}}$	Normalized μ bending mode slope at the accelerometer sensor, 1/meter

LIST OF SYMBOLS (Cont'd)

Symbol	Definition
$y'_{\mu\varphi}$	Normalized μ bending mode slope at the attitude sensor, 1/meter
$y'_{\mu\dot{\varphi}}$	Normalized μ bending mode slope at the angular rate sensor, 1/meter
y_{Si}	Normalized μ bending mode displacement at the ith slosh mass
y'_{Si}	Normalized μ bending mode slope at the ith slosh mass, 1/meter
$\dot{y}$	Lateral rigid body velocity at its center of gravity, meter/sec
$\ddot{y}$	Lateral rigid body acceleration at its center of gravity, meter/sec^2
α_i	Indicated angle-of-attack, radians
α_x	Local angle-of-attack, radian
β_E	Engine gimbal deflection, radians
β_c	Engine gimbal command, radians
$\ddot{\gamma}$	Acceleration of the control accelerometer, m/sec^2
η_μ	Generalized bending coordinate of the μ bending mode, meters
ξ_1	Lateral displacement of outer fuel slosh mass, meters
ξ_2	Lateral displacement of outer LOX slosh mass, meters
ξ_3	Lateral displacement of center LOX slosh mass, meters
ξ_4	Lateral displacement of upper LOX slosh mass, meters
ξ_5	Lateral displacement of LH_2 slosh mass, meters
φ	Angle between undeformed missile axis and space fixed reference, radians
φ_i	Indicated vehicle attitude, radians

LIST OF SYMBOLS (Concluded)

Symbol	Definition
$\dot{\varphi}$	Angular rate of undeformed missile axis rad/sec
$\dot{\varphi}_i$	Indicated angular rate at the rate gyro location, rad/sec
ψ	Phase angle of wind penetration with respect to the vehicle, radians
$\omega_{B\mu}$	Frequency of the μ bending mode, rad/sec

I. INTRODUCTION

As a vehicle flies through a wind profile, resultant local wind components along the vehicle create changes in local angle of attack. This effect is referred to as wind penetration. This report will determine the relative importance of wind penetration effects in flight simulation programs by developing an analytical method of evaluating theoretical transfer functions.

The expression for the local angle of attack, α_x, of a flexible vehicle with a local wind component, V_{WX}, at a particular vehicle station, x, is

$$\alpha_x = \varphi - \frac{1}{V}\left[\dot{y} - V_{WX} - (x_{CG} - x)\,\dot{\varphi} + \sum_{\mu=1}^{n} \eta_\mu y_{\mu x}\right] - \sum_{\mu=1}^{n} \eta_\mu y'_{\mu x} \qquad (1)$$

The net aerodynamic force acting on the vehicle is obtained by summing the product of the local lift gradient, dynamic pressure, reference area and local angle of attack.

$$F_{AERO} = q\,S \int_o^L C_{lx}\,\alpha_x\,dx$$

$$= q\,S\left[\varphi - \frac{\dot{y}}{V}\right]\int_o^L C_{lx}\,dx + \frac{qS}{V}\int_o^L C_{lx}\,V_{WX}\,dx$$

$$+ \frac{qS}{V}\,\dot{\varphi}\int_o^L C_{lx}\,(x_{CG} - x)\,dx - \frac{qS}{V}\sum_{\mu=1}^{n}\dot{\eta}_\mu \int_o^L C_{lx}\,y_{\mu x}\,dx$$

$$- q\,S\sum_{\mu=1}^{n}\eta_\mu \int_o^L C_{lx}\,y'_{\mu x}\,dx \qquad (2)$$

The net aerodynamic moment acting at the vehicle's center of gravity is

$$M_{AERO} = qS\left[\varphi - \frac{\dot{y}}{V}\right]\int_o^L C_{lx}(x_{CG} - x)\,dx +$$

$$+ \frac{qS}{V}\int_o^L C_{lx} V_{WX}(x_{CG} - x)\,dx$$

$$+ \frac{qS}{V}\dot{\varphi}\int_o^L C_{lx}(x_{CG} - x)^2\,dx$$

$$- \frac{qS}{V}\sum_{\mu=1}^{n}\dot{\eta}_\mu\int_o^L C_{lx} y_{\mu x}(x_{CG} - x)\,dx$$

$$- qS\sum_{\mu=1}^{n}\eta_\mu\int_o^L C_{lx} y'_{\mu x}(x_{CG} - x)\,dx. \qquad (3)$$

The generalized aerodynamic bending force for the (μ=m) bending mode is

$$A_m = qS\left[\dot{\varphi} - \frac{\dot{y}}{V}\right]\int_o^L C_{lx} y_{mx}\,dx$$

$$+ \frac{qS}{V}\int_o^L C_{lx} V_{WX} y_{mx}\,dx$$

$$+ \frac{qS}{V}\dot{\varphi}\int_o^L C_{lx}(x_{CG} - x)\, y_{mx}\,dx$$

$$- \frac{qS}{V}\sum_{\mu=1}^{n}\dot{\eta}_\mu\int_o^L C_{lx} y_{\mu x} Y_{mx}\,dx$$

$$- qS\sum_{\mu=1}^{n}\eta_\mu\int_o^L C_{lx} y'_{\mu x} y_{mx}\,dx. \qquad (4)$$

These relationships utilizing local wind distribution to define local angle of attack, aerodynamic forces, aerodynamic moments and generalized bending forces (equations 1 - 4) will be the means of inserting the wind penetration effects into the development of the theoretical transfer functions.

II. THEORETICAL TRANSFER FUNCTION ANALYSIS OF WIND PENETRATIONS

Theoretical transfer functions are analyzed as sinusoidal amplitude and phase response of flight mechanic parameters with respect to a given sinusoidal input. In this study, a sinusoidal wind profile is used as the forcing excitation. Transfer functions between any two flight mechanic parameters can be obtained from transfer functions of a common base by dividing amplitudes and differencing phase angles. A numerical evaluation of transfer functions was made for the SA-9 vehicle.

The SA-9 control system employed a fully active ST-124 platform which generated the attitude error signals, a body-fixed control accelerometer located in the Instrument Unit which provided partial load relief, and a three-axis control rate gyro package for angular rate control also located in the Instrument Unit. Angle-of-attack components were measured by a mode F 16 Q-ball angle-of-attack transducer mounted on the top of the Launch Escape System. The engine gimbal deflections were recorded from the individual actuator positions.

The mathematical technique of computing transfer functions is to determine the La Place Transform of the equations of motion and to evaluate the variables as a function of frequency. A total of fourteen equations (5-18) were used to represent the vehicle's dynamics and control in the yaw plane.

rotation equation

$$\ddot{\varphi} + D_T \dot{\varphi} - \frac{A_L \varphi}{I}\left[4\sum_{j=1}^{2} M_{Sj}\bar{x}_{Sj} + \sum_{j=3}^{5} M_{Sj}\bar{x}_{Sj}\right] + \frac{M_{AERO}}{I} + C_2\beta + \frac{F\eta}{I}(y_E - \bar{x}_E y'_E)$$

$$- \frac{\ddot{\beta}_E}{I}\left[M_E \ell_E \bar{x}_E + I_E\right] + \frac{4}{I}\sum_{j=1}^{2} M_{Sj}(\bar{x}_{Sj}\ddot{\xi}_j + A_L \xi_j) + \frac{1}{I}\sum_{j=3}^{5} M_{Sj}(\bar{x}_{Sj}\ddot{\xi}_j + A_L \xi_j) = 0 \qquad (5)$$

translation equation

$$\ddot{y} - A_L \varphi - \frac{F_{AERO}}{M} - \frac{F}{2M}\beta_E - \frac{M_E L_E \ddot{\beta}_E}{M} + \sum_{\mu}\frac{F y'_{\mu E}}{M}\eta_\mu - \frac{4}{M}\sum_{j=1}^{2} M_{Sj}\ddot{\xi}_j - \frac{1}{M}\sum_{j=3}^{5} M_{Sj}\ddot{\xi}_j = 0 \qquad (6)$$

angle-of-attack sensor equation

$$-\varphi + \alpha + \frac{1}{V}\left[\dot{y} - V_{W\alpha} - (x_{CG} - x_\alpha)\dot{\varphi} + \dot{\eta}\, y_{\mu\alpha}\right] + \eta\, y'_{\mu\alpha} = 0 \qquad (7)$$

control equation

$$\beta_c - g_2 G_{\ddot{\gamma}}\ddot{\gamma} - a_o G_\varphi \varphi - a_1 G_{\dot{\varphi}}\dot{\varphi} = 0 \qquad (8)$$

engine actuator equation

$$\beta_E - G_A \beta_c = 0 \qquad (9)$$

control accelerometer equation

$$(x_\varphi \ddot{\varphi} + A_L \varphi) - \ddot{Z} + \ddot{\gamma} - \sum_{\mu}(y_{\mu\ddot{\gamma}}\ddot{\eta}_\mu + A_L y'_{\mu\ddot{\gamma}}\ddot{\eta}_\mu) = 0 \qquad (10)$$

attitude sensor equation

$$\varphi_i - \varphi + \sum y'_{\mu\varphi}\eta_\mu = 0 \qquad (11)$$

attitude rate sensor equation

$$\dot{\varphi}_i - \dot{\varphi} + \sum_{\mu} y'_{\mu}\dot{\varphi}\dot{\eta}_\mu = 0 \qquad (12)$$

generalized bending equation (mth mode)

$$\frac{F Y_E}{2 M_{Bm}}\beta_E + (\ddot{\eta}_m + \omega_{Bm} g_{Bm}\dot{\eta}_m + \omega_{Bm}^2 \eta_m) + \frac{A_m}{M_{Bm}} - \frac{4}{M_{Bm}}\sum_{j=1}^{4}(M_{Sj} y_{Sj}\ddot{\xi}_j + A_L y'_{Sj}\xi_j)$$

$$- \frac{1}{M_{Bm}}\sum_{j=3}^{5}(M_{Sj} y_{Sj}\ddot{\xi}_j + A_L y'_{Sj}\xi_j) - \frac{1}{M_{Bm}}(M_E \ell_E y_{mE} + I_E y'_{mE})\ddot{\beta}_E = 0 \qquad (13)$$

slosh equations

$$-\bar{x}_{S1}\ddot{\varphi} + A_L \varphi + \ddot{Z} + y_{S1}\ddot{\eta} - A_L y'_{S1}\eta + (\ddot{\xi}_1 + \omega_{S1} g_{S1}\dot{\xi}_1 + \omega_{S1}\xi_1) = 0 \qquad (14)$$

$$-\bar{x}_{S2}\ddot{\varphi} + A_L \varphi + \ddot{Z} + y_{S2}\ddot{\eta} - A_L y'_{S2}\eta + (\ddot{\xi}_2 + \omega_{S2} g_{S2}\dot{\xi}_2 + \omega_{S2}\xi_2) = 0 \qquad (15)$$

$$-\bar{x}_{S3}\ddot{\varphi} + A_L\varphi + \ddot{Z} + y_{S3}\ddot{\eta} - A_L y'_{S3}\eta + (\ddot{\xi}_3 + \omega_{S3} g_{S3}\dot{\xi}_3 + \omega_{S3}\xi_3) = 0 \quad (16)$$

$$-\bar{x}_{S4}\ddot{\varphi} + A_L\varphi + \ddot{Z} + y_{S4}\ddot{\eta} - A_L y'_{S4}\eta + (\ddot{\xi}_4 + \omega_{S4} g_{S4}\dot{\xi}_4 + \omega_{S4}\xi_4) = 0 \quad (17)$$

$$-\bar{x}_{S4}\ddot{\varphi} + A_L\varphi + \ddot{Z} + y_{S5}\ddot{\eta} - A_L y'_{S5}\eta + (\ddot{\xi}_5 + \omega_{S5} g_{S5}\dot{\xi}_5 + \omega_{S5}\xi_5) = 0 \quad (18)$$

The vehicle was assumed elastic and was represented by the first bending mode. The resulting response should be fairly accurate up to approximately 3.0 cps which is the upper limit of the Flight Test Values. The cluster of propellant tanks in the S-I stage was assumed to have the same bending deflections as the center LOX tank. This is a good assumption for the first two bending modes, particularly since the bending deflections of all the S-I propellants are nearly identical and small with respect to the upper stage deflections. These cluster effects on transfer functions would be significant at frequencies greater than 5.0 cps. Quasi-steady aerodynamics, which states that the force along the vehicle depends only on the instantaneous local angle of attack, was assumed. The amplitude and phase of each control filter (accelerometer, attitude error, and angular rate) were continuously evaluated at the wind excitation frequency.

The La Place transform for most of the equations can easily be written. However, the transform of terms involving the integral of the wind penetration distribution over the vehicle require special analysis. These terms occur in the expression for the aerodynamic force, the aerodynamic moment, and the aerodynamic component of generalized force. Consider, for example, the wind penetration term F_{AWP}, in the aerodynamic force equation:

$$F_{AWP} = \frac{qS}{V}\int_0^L C_{lx}\, V_{Wx}\, dx . \quad (2)$$

At any given vehicle flight condition, this term is dependent in frequency, amplitude and phase with the exciting wind oscillations.

The transform of the wind penetration integral was numerically evaluated for particular flight time conditions. A common vehicle reference, station 0, was established to define the sinusoidal wind distribution over the vehicle (Figure 1).

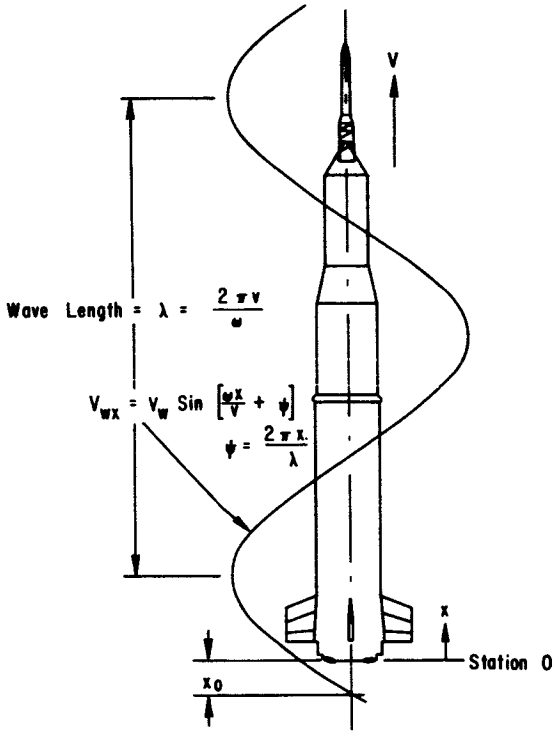

FIGURE 1. REFERENCE WIND PENETRATION

$$F_{AWP} = \left(\frac{qS}{V}\right)\int_0^L C_l\, V_{Wx}\, dx$$

$$= \left(\frac{qS}{V}\right) V_W \int_0^L C_l \sin\left(\frac{\omega x}{V} + \psi\right) dx$$

$$= \left(\frac{qS}{V}\, V_W\right)\left[\cos\psi \int_0^L C_l \sin\left(\frac{\omega x}{V}\right) dx + \sin\psi \int_0^L C_l \cos\left(\frac{\omega x}{V}\right) dx\right]. \quad (19)$$

Equation 19 indicates that the aerodynamic force due to wind penetration varies sinusoidally with the phase angle ψ. In-phase and out-of-phase components for La Place Transform are referenced as ψ equals 0° and 90°, respectively. Thus, at a particular frequency if

$$B_0 = \frac{qS}{V} \int_o^L C_l \sin\left(\frac{\omega x}{V}\right) dx \quad (20)$$

$$B_1 = \frac{qS}{V} \int_o^L \left[C_l \sin\left(\frac{\omega x}{V} + \frac{\pi}{2}\right)\right] dx \quad (21)$$

then

$$L(F_{AWP}) = (B_0 + B_1 i)\, L(V_W). \quad (22)$$

In a similar manner, the wind penetration component of the aerodynamic moment, equation (3), can be expressed as

$$M_{AWP} = \frac{qS}{V} \int_o^L C_l\, V_{WX}\, (x_{CG} - x)\, dx$$

$$= \frac{qS}{V} V_W \int_o^L \left[C_l \sin\left(\frac{\omega x}{V} + \psi\right)\right] (x_{CG} - x)\, dx \quad (23)$$

letting

$$C_0 = \frac{qS}{V} \int_o^L C_l \sin\left(\frac{\omega x}{V}\right)(x_{CG} - x)\, dx \quad (24)$$

$$C_1 = \frac{qS}{V} \int_o^L \left[C_l \sin\left(\frac{\omega x}{V} + \frac{\pi}{2}\right)\right] (x_{CG} - x)\, dx \quad (25)$$

then

$$L(M_{AWP}) = (C_0 + C_1 i)\, L(V_W). \quad (26)$$

Also, the wind penetration component of the generalized aerodynamic bending force for the mth bending mode equation (4) is

$$A_{mwp} = \frac{qS}{V} \int_o^L C_l\, V_{WX}\, Y_{mx}\, dx$$

$$= \frac{qS}{V} V_W \int_o^L \left[C_l \sin\left(\frac{\omega x}{V} + \psi\right)\right] y_{mx}\, dx. \quad (27)$$

Letting

$$D_0 = \frac{qS}{V} \int_o^L C_l \sin\left(\frac{\omega x}{V}\right) y_{mx}\, dx \quad (28)$$

$$D_1 = \frac{qS}{V} \int_o^L C_l \sin\left(\frac{\omega x}{V} + \frac{\pi}{2}\right) y_{mx}\, dx, \quad (29)$$

then

$$L(A_{mwp}) = (D_0 + D_1 i)\, L(V_W). \quad (30)$$

The transform coefficients B_0, B_1, C_0, C_1, D_0 and D_1 can be expressed as polynomials in ω for any particular flight time condition by performing least square solutions of results from specific values of ω.

$$B_0 = \sum_{k=0}^{n} B_{0k}\, \omega^k$$

$$B_1 = \sum_{k=0}^{n} B_{1k}\, \omega^k$$

$$C_0 = \sum_{k=0}^{n} C_{0k}\, \omega^k$$

$$C_1 = \sum_{k=0}^{n} C_{1k}\, \omega^k$$

$$D_0 = \sum_{k=0}^{n} D_{0k}\, \omega^k$$

$$D_1 = \sum_{k=0}^{n} D_{1k}\, \omega^k. \quad (31)$$

For ease of presentation, definite integrals are represented by the following set of constants:

$$J_0 = qS \int_o^L C_{lx}\, dx$$

$$J_1 = qS \int_o^L C_{lx}\, (x_{CG} - x)\, dx$$

$$J_2 = qS \int_o^L C_{lx}\, (x_{CG} - x)^2 dx$$

$$G_\mu = qS \int_o^L C_{lx}\, y_\mu\, dx$$

$$\bar{G}_\mu = qS \int_o^L C_{lx}\, y_\mu\, (x_{CG} - x)\, dx$$

$$H_\mu = qS \int_o^L C_{lx}\, y'_\mu\, dx$$

$$\bar{H}_\mu = qS \int_o^L C_{lx}\, y'_\mu\, (x_{CG} - x)\, dx$$

$$A_{m\mu} = qS \int_o^L C_{lx}\, y_\mu\, y_m \, dx$$

$$K_{m\mu} = qS \int_o^L C_{lx}\, y'_\mu\, y_m \, dx \,. \qquad (32)$$

The La Place Transform of the yaw flight mechanic equations (5-18) can now be expressed as the following set of simultaneous linear equations in the S domain:

$$\left[S^2 + D_T S + \frac{J_2 S}{I V} + \frac{J_1}{I} - \frac{A}{I}\left(4\sum_{j=1}^{2} M_{Sj}\bar{x}_{Sj} + \sum_{j=3}^{5} M_{Sj}\bar{x}_{Sj}\right)\right] L(\varphi) - \frac{J_1}{IV} L(\dot{y}) + \frac{1}{I}(C_0 + C_1 i)\, L(V_W)$$

$$- \frac{1}{I}\sum_{\mu}\left(\frac{S\bar{G}_\mu}{V} + \bar{H}_\mu\right) L(\eta_\mu) + C_2\, L(\beta_E) + \frac{F}{I}(y_E - x_E y'_E)\, L(\eta) - \frac{1}{I}\left[M_E L_E \bar{x}_E + I_E\right] S^2 L(\beta_E)$$

$$+ \frac{4}{I}\sum_{j=1}^{2} M_{Sj}(\bar{x}_{Sj} S^2 + A)\, L(\xi_j) + \frac{1}{I}\sum_{j=3}^{5} M_{Sj}(\bar{x}_{Sj} S^2 + A)\, L(\xi_j) = 0 \qquad (33)$$

$$S\, L(\dot{Z}) - (A_L + \frac{J_0}{M})\, L(\varphi) + \frac{J_0}{MV} L(\dot{y}) - \frac{1}{M}(B_0 + B_1 i)\, L(V_W) + \frac{1}{M}\sum_{\mu}\left(\frac{G_\mu S}{V} + H_\mu + F y'_E\right) L(\eta_\mu)$$

$$- \frac{1}{M}(\frac{F}{2} + M_E L_E S^2)\, L(\beta_E) - \frac{4}{M}\sum_{j=1}^{2} M_{Sj} S^2 L(\xi_j) - \frac{1}{M}\sum_{j=3}^{5} M_{Sj} S^2 L(\xi_j) = 0 \qquad (34)$$

$$-\left[1 + \frac{(x_{CG} - x_\alpha)}{V} S\right] L(\varphi) + L(\alpha_i) + \frac{1}{V} L(\dot{y}) - \frac{1}{V}(P_0 + P_1 i)\, L(V_W) + (\frac{y_\alpha S}{V} + y'_\alpha)\, L(\eta) = 0 \qquad (35)$$

$$L(\beta_c) - g_2 G_{\ddot{\gamma}}(S)\, L(\ddot{\gamma}) - a_0 G_\varphi(S)\, L(\varphi_i) - a_1 G_{\dot{\varphi}}(S)\, L(\dot{\varphi}_i) = 0 \qquad (36)$$

$$L(\beta_E) - G_A(S)\, L(\beta_c) = 0 \qquad (37)$$

$$(x_\varphi S^2 + A)\, L(\varphi) - S\, L(\dot{Z}) + L(\ddot{\gamma}) - (y_{\ddot{\gamma}} S^2 + A y'_{\ddot{\gamma}})\, L(\eta) = 0 \qquad (38)$$

$$L(\varphi_i) - L(\varphi) + y'_\varphi\, L(\eta) = 0 \qquad (39)$$

$$L(\dot{\varphi}_i) - S\, L(\varphi) + S y'_\varphi\, L(\eta) = 0 \qquad (40)$$

$$\frac{1}{M_m}\left(\frac{F y_E}{2} - M_E L_E y_E S^2 - I_E y'_E S^2\right) L(\beta_E) + \frac{G_m}{M_m} L(\varphi) + \frac{\bar{G}_m}{VM_m} L(\dot{\varphi}) - \frac{G_m}{VM_m} L(\dot{y}) + \frac{(D_0 + D_1 i)}{M_m} L(V_W)$$

$$+ \left(S^2 + \omega_m g_m S - \sum_{\mu} \frac{A_{m\mu} S}{VM_m} + \omega^2_m - \sum_{\mu} \frac{K_{m\mu}}{M_m}\right) L(\eta_m) - \frac{4}{M_m}\sum_{j=1}^{4} (M_{Sj} y_{Sj} S^2 + A y'_{Sj})\, L(\xi_j)$$

$$- \frac{1}{M_m}\sum_{j=3}^{5} (M_{Sj} y_{Sj} S^2 + A y'_{Sj})\, L(\xi_1) = 0 \qquad (41)$$

$$(S^2 + \omega_{S1} g_{S1} S + \omega^2_{S1})\, L(\xi_1) - (\bar{x}_{S1} S^2 - A) L(\varphi) + S\, L(\dot{Z}) + \sum_{\mu} (y_{S1} S^2 - A y'_{S1})\, L(\eta_\mu) = 0 \qquad (42)$$

$$(S^2 + \omega_{S2}\, g_{S2}\, S + \omega^2_{S2})\ L(\xi_2) - (\bar{x}_{S2}\, S^2 - A)\ L(\varphi) + S\, L(\dot{Z}) + \sum_{\mu} (y_{S2}\, S^2 - A\, y'_{S2})\ L(\eta_\mu) = 0 \qquad (43)$$

$$(S^2 + \omega_{S3}\, g_{S3}\, S + \omega^2_{S3})\ L(\xi_3) - (\bar{x}_{S3}\, S^2 - A)\ L(\varphi) + S\, L(\dot{Z}) + \sum (y_{S3}\, S^2 - A\, y'_{S3})\ L(\eta_\mu) = 0 \qquad (44)$$

$$(S^2 + \omega_{S4}\, g_{S4}\, S + \omega^2_{S4})\ L(\xi_4) - (\bar{x}_{S4}\, S^2 - A)\ L(\varphi) + S\, L(\dot{Z}) + \sum_{\mu} (y_{S4}\, S^2 - A\, y'_{S4})\ L(\eta_\mu) = 0 \qquad (45)$$

$$(S^2 + \omega_{S5}\, g_{S5}\, S + \omega^2_{S5})\ L(\xi_5) - (\bar{x}_{S5}\, S^2 - A)\ L(\varphi) + S\, L(\dot{Z}) + \sum_{\mu} (y_{S5}\, S^2 - A\, y'_{S5})\ L(\eta_\mu) = 0 \qquad (46)$$

These equations rewritten in matrix notation are

$$\left[\ \text{Matrix "A"}\ \right] L \left\{ \begin{matrix} \varphi \\ \varphi_i \\ \phi_i \\ \ddot{\gamma} \\ \alpha_i \\ \dot{Z} \\ \beta_E \\ \beta_c \\ \eta \\ \xi_1 \\ \xi_2 \\ \xi_3 \\ \xi_4 \\ \xi_5 \end{matrix} \right\} = \left\{ \begin{matrix} \text{Column} \\ \text{"B"} \end{matrix} \right\} L(V_W). \qquad (47)$$

Although both matrix "A" and column "B" are complex coefficients of the transform elements, the solution of these simultaneous linear equations is generally well known. One approach would be to expand the determinants as an S polynomial according to Cramer's rule. For example,

$$L(\varphi) = [\text{function of S}]\ L(V_W)$$

or

$$\frac{L(\varphi)}{L(V_W)} = \text{function of S}. \qquad (48)$$

If this were evaluated at a particular frequency, the transfer function would result in a complex number,

$$\frac{L(\varphi)}{L(V_W)} = R + Ii. \qquad (49)$$

The transfer function is more conveniently expressed as a harmonic relationship at any particular frequency with amplitude ratio and phase angle.

$$\text{Amplitude ratio} = \sqrt{R^2 + I^2} \qquad (50)$$

$$\text{Phase angle} = \tan^{-1}\left(\frac{I}{R}\right). \qquad (51)$$

III. ANALYTICAL RESULTS AND COMPARISONS WITH RECORDED FLIGHT TEST DATA

The Flight Mechanic Transfer Functions including the wind penetration effects as indicated by the equations were evaluated for the SA-9 80-second flight condition. The resulting analytical transfer functions for gimbal engine deflection and angle of attack are shown as solid lines on Figures 2 and 3 respectively. For comparison, corresponding transfer functions were evaluated for a wind distribution instantaneously constant over the entire vehicle - that is, no wind penetration. These transfer functions are indicated as dashed lines in Figures 2 and 3. For this particular condition, the wind penetration effects are more pronounced in the gimbal engine transfer function than that of the angle of attack. In fact, the wind penetration effects for the gimbal engine deflection are five times greater in amplitude at 1.7 cps than corresponding analytical value without wind penetration effect.

Further inspection of the gimbal engine deflection and angle-of-attack transfer functions (Figures 2 and 3) indicates that the wind penetration effects are strongly coupled to the first bending mode (peak at 2.3 cps). A transfer function plot of the first bending mode generalized coordinate, η_1, shows this to be true (Fig. 4). The wind penetration effect increases the amplitude of the first bending generalized coordinate transfer function by a factor of 2.6 at 2.3 cps

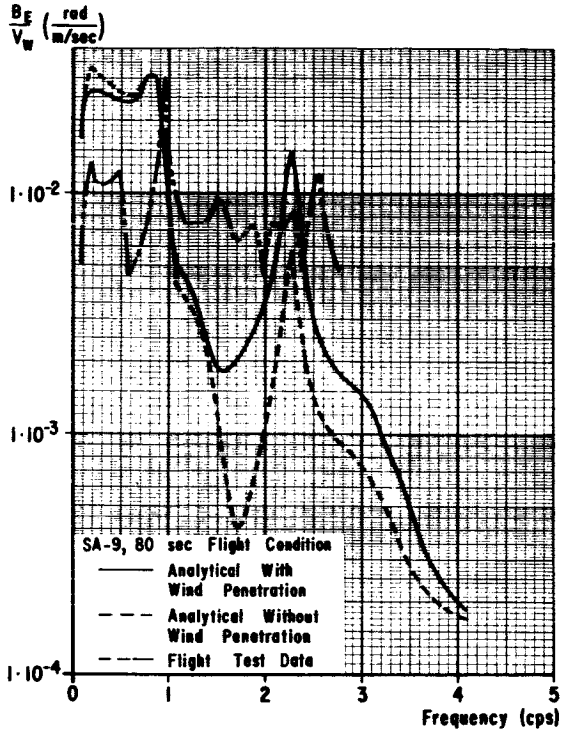

FIGURE 2. GIMBAL ENGINE DEFLECTION TO WIND EXCITATION TRANSFER FUNCTION

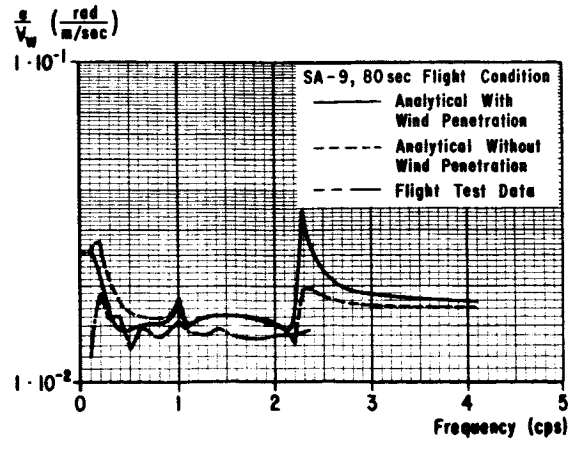

FIGURE 3. ANGLE-OF-ATTACK TO WIND EXCITATION TRANSFER FUNCTION

and 6.6 at 4.0 cps. This, in effect, states that neglecting wind penetration effects results in underestimating the bending mode coupling by a considerable margin.

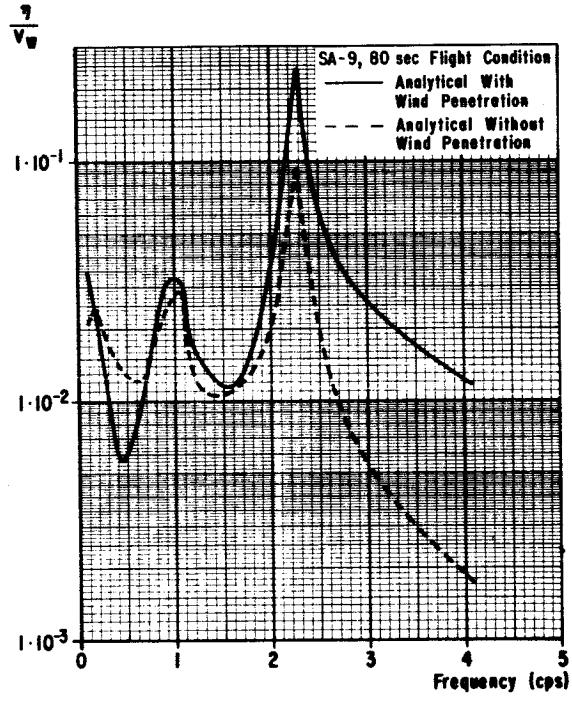

FIGURE 4. WIND PENETRATION EFFECTS ON GENERALIZED BENDING MODE TRANSFER FUNCTION

A spectral analysis of recorded SA-9 flight test data was made hopefully to corroborate the wind penetration effects. The corresponding amplitude transfer functions are shown plotted on Figures 2 and 3. Even with the uncertain amount of noise content associated with flight telemetry data, the results are surprisingly close. The comparison of engine gimbal deflection indicates the flight test results to be much closer to the analytical values which include the wind penetration effects. The angle-of-attack transfer function comparison indicates the flight test amplitudes to be within 15 percent of analytical values and in general closer to those computed using wind penetration effects. With a ten-samples-per-second rate, flight test transfer functions were limited to low frequencies.

IV. CONCLUSIONS

The effect of wind penetration was seen to be significant at frequencies greater than 1.5 cps for the SA-9, 80-second flight condition. These wind penetration effects are aerodynamically introduced in the equations of motion by analyzing the local angle-of-attack distributions. Some insight as to the relative importance of these effects during a particular trajectory can be made by investigating the difference between an average angle of attack and one obtained for an instantaneous constant wind distribution over the entire vehicle length. This resolves into an analysis of the vehicle's length with respect to the penetrating wind wave length. As the vehicle increases velocity, a given exciting wind frequency will require a larger wave length. This larger wave length will reduce the variation in local angle of attack.

The relationship between angle-of-attack error profiles as a function of wind penetration frequency and vehicle flight time is shown on Figure 5 for the Saturn 201 vehicle. Although these percentile curves were obtained by an open loop analysis, they are reasonably accurate. These curves are to be interpreted in the following manner: For example, neglect of wind penetration of a wind excitation at 1.7 cps occurring at 80-second flight time will result in a 50 percent error in angle of attack.

Wind penetration effects can and should be included in the flight simulation analysis of a wind profile. Such an analysis would compute vehicle angle of attack, not at a single point, but at many stations along the vehicle and numerically integrate for the overall aerodynamic effect.

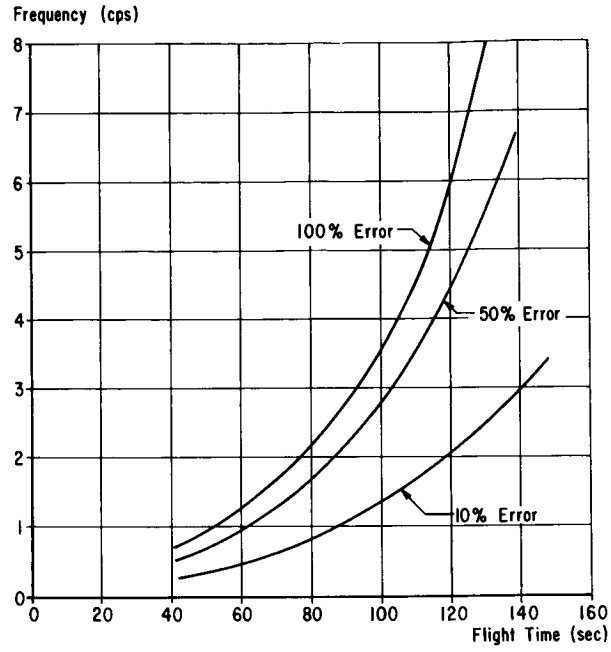

FIGURE 5. ANGLE-OF-ATTACK ERROR PROFILES RESULTING FROM NEGLECTING WIND PENETRATION FOR SATURN 201 FLIGHT

ACKNOWLEDGEMENTS

Mrs. Sylvia Bryant, R-COMP-RDC, evaluated the La Place Transform of the wind distribution integrals and also performed the spectral analysis of the flight test data on the CDC 3200.

Mr. Doug Denalt, G. E., computed the transfer functions from the complex linear equations on the IBM 7094.

VIII. PUBLICATIONS AND PRESENTATIONS

A. PUBLICATIONS

TECHNICAL MEMORANDUM X-53249

April 23, 1965

NEAR-OPTIMUM GUIDANCE - AN ANALYSIS OF FUEL PENALTY

By

Lyle R. Dickey

George C. Marshall Space Flight Center
Huntsville, Alabama

ABSTRACT

An explicit solution of the linearized equations of motion is used to obtain the deviations in end conditions, Δr and $\Delta\theta$, and the additional burning time, Δt, expressed as integrals of functions of thrust angle deviations, $\Delta\chi$. Under the constraint that $\Delta r = \Delta\theta = 0$, the calculus of variations is applied to minimize Δt. The resulting Euler-Lagrange equation evaluated at $\Delta\chi = 0$ gives a simple relationship which is used to show that Δt is a second order function of $\Delta\chi$. This function is evaluated numerically for the second stage of an early SA-6 design. Results show that, if the mission is accomplished, the thrust angle may differ by as much as 2 degrees throughout the second stage with a propellant penalty of only 34 pounds. It follows that the capability of meeting the mission is the prime requisite of a guidance function and optimality is then only a second order consideration.

TECHNICAL MEMORANDUM X-53290

July 9, 1965

FPS-16 RADAR/JIMSPHERE WIND DATA MEASURED AT THE EASTERN TEST RANGE

By

James R. Scoggins and Michael Susko

George C. Marshall Space Flight Center
Huntsville, Alabama

ABSTRACT

This report presents wind measurements at Eastern Test Range employing the FPS-16 Radar/Jimsphere method. One hundred and twelve wind velocity profiles are presented. These measurements were made from November 1964 to May 1965. These data are not intended as a recommended statistical sample for structural and control system design criteria. They are presented to document this limited group of detailed wind profiles, and to provide a source for these data for use by other research organizations. The wind data presented herein supersedes the wind data presented in MTP-AERO-62-86.

TECHNICAL MEMORANDUM X-53292

July 12, 1965

PROGRESS REPORT NO. 7 ON STUDIES IN THE FIELDS OF SPACE FLIGHT AND GUIDANCE THEORY

Sponsored by Aero-Astrodynamics Laboratory of Marshall Space Flight Center

ABSTRACT

The progress reports of NASA-sponsored studies in the areas of space flight and guidance theory are presented. The studies are carried on by several universities and industrial companies. This progress report covers the period from July 23, 1964, to April 1, 1965. The contracts are technically supervised by personnel of the Astrodynamics and Guidance Theory Division, Aero-Astrodynamics Laboratory, Marshall Space Flight Center.

TECHNICAL MEMORANDUM X-53293

July 13, 1965

SA-10 FLIGHT MECHANICAL SUMMARY

George C. Marshall Space Flight Center
Huntsville, Alabama

ABSTRACT

This report presents the Flight Mechanical Summary for Saturn I vehicle SA-10 to be launched from Pad 37B, Eastern Test Range, on a flight azimuth of 95.2 degrees East-of-North. A successful flight will insert the spent S-IV stage and payload consisting of an Apollo boilerplate (BP-9) and a Meteoroid Technology Satellite (Pegasus C) into a 535-km circular orbit. Included is a discussion of the operational predicted trajectory with its orbital mission objectives and constraints, guidance, sequencing, and insertion parameters. The three-sigma envelope of thrust, flow rate, liftoff mass, and wind speed variations is given, along with impact data, in the Range Safety part of this report. A study of wind disturbances, three-sigma C_1 and C_2 variations, and $\pm$ 10 percent control gain deviations shows the vehicle to be structurally capable of withstanding the expected winds during the launch period. Pertinent tracking and telemetry ground coverage data are presented for powered and orbital flight phases.

TECHNICAL MEMORANDUM X-53298

July 21, 1965

A PRACTICAL APPROACH TO THE OPTIMIZATION OF THE SATURN V SPACE VEHICLE CONTROL SYSTEM UNDER AERODYNAMIC LOADS

By

Robert S. Ryan and Dieter Teuber

George C. Marshall Space Flight Center
Huntsville, Alabama

ABSTRACT

The equations for the bending moment of a launch vehicle are written including the effects of bending and sloshing dynamics. By making certain simplifying assumptions, the bending moment equation is transformed to be a function of rigid vehicle angle of attack, engine deflection, bending mode acceleration and sloshing mode acceleration. This form is particularly advantageous for use in optimization techniques by the control engineer. The response of a Saturn V class vehicle was solved and the control system optimized to bending moments using data covering a period of six years, amounting to 4,384 measured wind profiles, and the GPS high speed repetitive analog computer. A comparison between the bending moment response envelope of the measured winds and the bending moment response of the MSFC synthetic wind profile is made.

TECHNICAL MEMORANDUM X-53303

July 26, 1965

HOPI-DART AND CAJUN-DART ROCKET WIND MEASURING SYSTEMS

By

Robert E. Turner and Luke P. Gilchrist*

George C. Marshall Space Flight Center
Huntsville, Alabama

ABSTRACT

Three Hopi-Dart rockets were fired in February 1964, and during February 1965 through June 1965 seventeen Cajun-Dart rockets were fired to obtain wind flow data. These wind flow data are obtained by radar tracking of Mylar chaff expelled from these rocket systems. An altitude profile of the measured winds and a description of the two-stage rocket-delivery systems are given.

In February 1964 the observed winds were westerly. In 1965 the observed winds were westerly during February and March, changing to easterly in late March and continuing through May, and reversing to northwesterly in June. These data are presented graphically.

TECHNICAL MEMORANDUM X-53319

August 16, 1965

CONIC SOLUTIONS TO THE INTERPLANETARY TRANSFER PROBLEM WITH CONSTANT OR MINIMUM INJECTION ENERGY

By

Lamar E. Bullock

George C. Marshall Space Flight Center
Huntsville, Alabama

---

* Luke P. Gilchrist is associated with the Lockheed Corporation working under Contract No. NAS 8-20082.

ABSTRACT

This report describes a method for calculating minimum and constant injection energy, C_3, values for conic interplanetary trajectories. The planets are assumed to move on mutually inclined elliptical orbits about the sun. Lambert's theorem is used to solve the time-constraint on the two-point boundary value problem, and an iterative procedure, with arrival date as the isolation parameter, is used to determine the desired C_3.

Typical results are presented for Earth-to-Jupiter trajectories in the 1970-71 launch period. The comparisons made with previously used methods indicate the procedures described in the report produce results of comparable accuracy, with a savings in computation time.

TECHNICAL MEMORANDUM X-53325

September 2, 1965

STATISTICAL ANALYSIS OF PHOTOGRAPHIC METEOR DATA - PART 1 - OPIK'S LUMINOUS EFFICIENCY AND SUPPLEMENTED WHIPPLE WEIGHTING

By

Charles C. Dalton

George C. Marshall Space Flight Center
Huntsville, Alabama

ABSTRACT

After adjustment of the estimate for the mass of a zero-absolute-visual-magnitude meteor, formulas for meteoroid mass are derived from E. J. Opik's (1958) physical theory for dustball meteors. Masses are calculated for G. S. Hawkins and R. B. Southworth's (1958) random sample of 285 sporadic photographic meteors. Weighting functions are derived for the statistical minimization of the effects of several sources of bias. Means, standard deviations, and ordinary, multiple, and partial correlations are shown for a 5-variate statistical analysis. Weighted cumulative distributions for parameters are plotted for two gradations with respect to mass. Data-point distributions are plotted which establish cumulative flux as functions of mass, momentum, kinetic energy, etc., which show the effects of the earth's motion on the distributions and correlation of parameters.

The results support revisions in the author's (Jan. 1965) interpretation of Explorer XVI data and predicted puncture rates for the Pegasus meteoroid measurement satellites. The apparent discrepancy between the logarithmically linear relations between cumulative flux and mass, as inferred from photographic meteors by G. S. Hawkins and E. K. L. Upton (1958) and from zodical light and solar F-corona data by D. B. Beard (1963), is shown to be accountable by E. J. Opik's (1951) probability that a particular meteoroid will encounter the earth in one revolution of the particle.

TECHNICAL MEMORANDUM X-53326

September 3, 1965

SUMMARY OF BASE THERMAL ENVIRONMENT MEASUREMENTS ON THE SATURN I BLOCK I FLIGHT VEHICLES

By

Ira P. Jones, Jr.

George C. Marshall Space Flight Center
Huntsville, Alabama

ABSTRACT

Base thermal environment measurements were made on all of the Saturn I Block I vehicles (SA-1 through SA-4). Total and radiation calorimeter measurements were made in the base region along with base gas temperatures and pressures. Details of the instrumentation and problems encountered in the data evaluation are discussed, and the data are compared from flight to flight on the basis of altitude. Some representative correlations of total and radiation heating, gas temperatures, and base pressures with small scale model tests are included. Flight heat transfer coefficients are calculated and compared with the model results.

TECHNICAL MEMORANDUM X-53327

September 7, 1965

DERIVATION OF PARAMETRIC VALUES FOR A GREENHOUSE MODEL OF THE CYTHEREAN ATMOSPHERE

By

Robert B. Owen

George C. Marshall Space Flight Center
Huntsville, Alabama

ABSTRACT

Presented is a self-consistent model atmosphere for the planet Venus, with emphasis on parameters of general use in developing vehicle design criteria. Kern and Schilling's program [1] for generation of atmospheric parameter values is coupled with the most recent estimates of surface conditions in order to derive the atmospheric environment at different altitudes. A range of initial values is used to produce a parametric band most representative of actual conditions. Because of the extreme pressures and temperatures involved, it is felt that design for such an environment presents an engineering problem of the first magnitude.

TECHNICAL MEMORANDUM X-53328

September 9, 1965

TERRESTRIAL ENVIRONMENT (CLIMATIC) CRITERIA GUIDELINES FOR USE IN SPACE VEHICLE DEVELOPMENT, 1965 REVISION

By

Glenn E. Daniels
James R. Scoggins
and
Orvel E. Smith

George C. Marshall Space Flight Center
Huntsville, Alabama

ABSTRACT

This document provides guidelines on probable climatic extremes and probabilities-of-occurrence of terrestrial environment data specifically applicable for NASA space vehicles and associated equipment development. The geographic areas encompassed are the Eastern Test Range (Cape Kennedy, Florida); Huntsville, Alabama; New Orleans, Louisiana; the Western Test Range (Point Arguello, California); Sacramento, California; Wallops Test Range (Wallops Island, Virginia); White Sands Missile Range, New Mexico; and intermediate transportation areas. In addition, a section has been included to provide information on the general distribution of natural environment extremes in the United States (excluding Alaska and Hawaii) that may be useful to specify design criteria in transportation of space vehicle components from subcontractors. This document omits climatic extremes for worldwide operational conditions. This is consistent with the existing philosophy regarding the employment of large space vehicles, since launching and test areas are relatively restricted due to the availability of facilities and real estate.

This document presents the latest available information on probable climatic extremes, and superseded information presented in TM X-53023. The information in this document is recommended for employment in the development of space vehicles and associated equipment, unless otherwise stated in contract work specifications.

TECHNICAL MEMORANDUM X-53344

October 7, 1965

GROUND LEVEL ACOUSTICAL FOCI IN A THREE-LAYERED ATMOSPHERE

By

Willi H. Heybey

George C. Marshall Space Flight Center
Huntsville, Alabama

ABSTRACT

An infinitesimally slender bundle of sound rays emitted by a point source can, under certain meteorological conditions, be returned to the horizontal plane on which the source sits, and at the same time, may be narrowed down to enclose an area actually equal to zero. In such cases the common point of arrival is called an acoustical focus. The intensity of returned energy there attains a very high degree capable of damaging effects.

For determining such points the atmosphere is usually divided up into layers in each of which the change of the sound speed with height is considered constant. Three layers often suffice to approximate the many layers arising from observation.

The report studies focus formation engendered by the third layer in collaboration with the two lower

layers. A focus may appear in variegated circumstances. For each case a computational scheme is given which may be followed by slide rule or assigned to machines if higher accuracy or a systematic survey is desired.

TECHNICAL MEMORANDUM X-53351

October 21, 1965

AN ENVIRONMENTAL MODEL FOR VAN ALLEN BELT PROTONS

By

William T. Roberts

George C. Marshall Space Flight Center
Huntsville, Alabama

ABSTRACT

The majority of the manned and unmanned missions in space for at least the next ten years will be composed mainly of earth orbiting satellites and space stations. Although there are many environmental aspects of space which must be explored and elaborated upon before the successful launching of such missions, few are so critical as the radiation environment which will be encountered.

The radiation environment for earth orbiting vehicles will consist primarily of (1) Van Allen particles, (2) solar flare particles, and (3) galactic cosmic particles. Of these three, the Van Allen belt particles present the greatest hazard.

This report summarizes the knowledge of the energy spectrum and distribution of the Van Allen proton belt as it is known today. A computer program has been developed for calculating Van Allen particles incident upon vehicles in earth orbits. Based upon the 1963 FLUX program of McIlwain, we find that a vehicle in a highly elliptic orbit may encounter as many as 1.1×10^8 protons/cm^2/orbit with 40 Mev $\leq$ F $\leq$ 110 Mev. In the magnetic equatorial plane, the flux of protons with E $\geq$ .5 Mev may be as high as 2.2×10^7 protons/cm^2/sec.

TECHNICAL MEMORANDUM X-53354

November 1, 1965

LAUNCH WINDOWS FOR TWO TYPES OF ORBITS SYNCHRONOUS WITH THE LUNAR PERIOD

By

E. H. Bauer and L. D. Mullins

George C. Marshall Space Flight Center
Huntsville, Alabama

ABSTRACT

This report presents launch windows for two types of orbits designed to be synchronous with the lunar orbital period. One class of conic, the 1/8-class orbit, maintains a period one-eighth that of the lunar period and an apogee of approximately one-half the lunar distance. The second type, 1/2-class orbit, consists of a conic with one-half the lunar period and apogee radius approximately equal to the lunar distance, an Arenstorf Orbit. Launch windows are presented which reflect the assumptions and constraints applicable to the specific geometry of each class and to the S-IB/S-IVB/Centaur vehicle. The time period considered for the 1/2-class orbit is December 1967 through June 1968 where only discrete launch opportunities are found. The window for the 1/8-class is less constrained and is shown for each day of any year.

TECHNICAL MEMORANDUM X-53360

November 18, 1965

STATISTICAL ANALYSIS OF PHOTOGRAPHIC METEOR DATA, PART II: VERNIANI'S LUMINOUS EFFICIENCY AND SUPPLEMENTED WHIPPLE WEIGHTING

By

Charles C. Dalton

George C. Marshall Space Flight Center
Huntsville, Alabama

ABSTRACT

This report is Part II in a series of four reports on the statistical analysis of the Hawkins and Southworth random sample of 285 sporadic photographic

meteors. The four parts of the analysis comprise the combinations from two alternative formulations for meteoroid mass and two alternative formulations for data weighting. Parts I and II have the same weighting as a function of air-entry velocity and other parameters. But the surprisingly large disparity between the results with Öpik's luminous efficiency suggests the possibility of considerable bias from weighting inversely with the 1.5-power of velocity.

TECHNICAL MEMORANDUM X-53363

December 3, 1965

MEASUREMENTS OF WINDS BY CHEMICAL RELEASES IN THE UPPER ATMOSPHERE

By

Hugh Wilson Morgan

George C. Marshall Space Flight Center
Huntsville, Alabama

ABSTRACT

Upper atmospheric winds are of importance to the designers of space vehicles as well as to geophysicists. For this reason a number of organizations have begun to study winds above 80 kilometers by releasing into the upper atmosphere chemicals which luminesce either by the action of sunlight or by a reaction with naturally occurring molecules. Seventy-seven of these releases were studied in an effort to determine a statistical model for wind velocities between 80 and 200 kilometers at mid-latitude sites.

TECHNICAL MEMORANDUM X-53365

December 3, 1965

BOUNDARY VALUE PROBLEMS ASSOCIATED WITH OPTIMIZATION THEORY

By

Hugo L. Ingram

George C. Marshall Space Flight Center
Huntsville, Alabama

ABSTRACT

Optimization theory is applied to the physics of trajectory problems to yield a boundary value formulation. Three practical numerical methods for obtaining solutions to boundary value problems are discussed, and a detailed explanation of the application of the most efficient method to a sample problem is included. Numerical methods are needed because the application of optimization theory to trajectory problems generally results in nonlinear differential equations connecting the boundary conditions that are not all specified at the same value of the independent variable. The methods discussed are adaptable to the solution of boundary value problems other than the ones associated with trajectory problems or optimization theory.

TECHNICAL MEMORANDUM X-53367

December 10, 1965

ELASTIC STABILITY OF A SLENDER BAR WITH FREE-FREE ENDS UNDER DYNAMIC LOADS

By

Frank C. Liu

George C. Marshall Space Flight Center
Huntsville, Alabama

ABSTRACT

Problems of elastic stability of a space rocket under dynamic, nonconservative loads are presented. The spacecraft is treated as a slender, uniform cylindrical bar with free-free ends. Analysis of the frequency of the transverse vibration coupled with the longitudinal vibration under the action of time-varying thrust force based on Galerkin's method leads to Mathieu's equation. The elastic stability boundaries of the frequency ratio, longitudinal to transverse, versus the thrust are obtained. The dynamic buckling thrust of a uniform bar with various boundary conditions is presented. The aerodynamic force induced from the oscillation of the rocket in supersonic speed on the critical thrust is investigated. A numerical illustration is given to show the relationship of the critical thrust versus flight speed at various flight altitudes.

TECHNICAL MEMORANDUM X-53368

December 13, 1965

NUMERICAL PROCEDURES FOR ROLL STABILITY STUDIES

By

Philip J. Hays

George C. Marshall Space Flight Center
Huntsville, Alabama

ABSTRACT

This report illustrates the numerical procedure used by the Aero-Astrodynamics Laboratory in performing roll stability analyses for Saturn type space vehicles. Vehicle control in the roll channel is provided by a position gyro and a rate gyro. The dynamics of the rate gyro are included as a separate equation in the equations of motion. The modes of oscillation in this system are (1) torsion, (2) roll, (3) roll sloshing, (4) rate gyro roll, and (5) swivel engine. Two methods are available for solving the system's eigenvalues: the matrix iteration method and the characteristic equation approach. In both cases the system is solved for the normalized eigenvectors, which provide additional information about the system.

The frequency response of the system, at the control thrust vector point, can be found for a sinusoidal forcing function at various sensor locations.

The equations of motion are derived in the appendix.

TECHNICAL MEMORANDUM X-53372

December 21, 1965

ESTIMATION IN THE NEGATIVE BINOMIAL DISTRIBUTION

By

A. Clifford Cohen, Jr.*

George C. Marshall Space Flight Center
Huntsville, Alabama

ABSTRACT

Practical simplified procedures are developed in this paper for calculating estimates of parameters of the negative binomial distribution with probability function

$$f(x) = \frac{\Gamma(x+k)}{x!\,\Gamma(k)} p^k (1-p)^x; \quad x = 0, 1, 2\ldots$$

where $0 < p < 1$ and $k > 0$. Moment estimators, maximum likelihood estimators, and estimators based on moments and frequencies in selected classes are given both for the complete and for the truncated (with missing zero class) distribution. To facilitate calculation of the various estimators given, a table of the function $-p \ln p/(1-p)$ with entries to six decimals at intervals of 0.001 for the argument p, is included. Illustrative examples are also included.

TECHNICAL MEMORANDUM X-53362

Nov. 30, 1965

LINEAR FEEDBACK GUIDANCE

By

Lyle R. Dickey

George C. Marshall Space Flight Center
Huntsville, Alabama

ABSTRACT

The Problem of determining the coefficients for a linear feedback guidance system with polynomial is investigated. The solution to the linearized equations of motion is employed to determine the first partial derivatives of the optimum thrust angle deviations with respect to position and velocity coordinates. The partial derivatives are approximated by quadratic time functions, which in turn are the first approximation to a time-variable set of gains. This system is then analyzed, and two of the weighting functions are linearized with respect to perturbations in the polynomial coefficients. Changes in these coefficients are determined to minimize the weighted sum of squares of these expressions over several time points. The resulting changes were made, and a satisfactory reduction in magnitude of these weighting functions resulted. This, coupled with a linear feedback of thrust acceleration and a small time function derived to cancel the effect of initial conditions, produced the final guidance function which performed exception-

---

* Professor of Mathematics, University of Georgia, Athens, Georgia. The research reported in this paper was performed under NASA Contract NAS8-11175 with the Aerospace Environment Office, Aero-Astrodynamics Laboratory, Marshall Space Flight Center, Huntsville, Alabama. Mr. O. E. Smith is the NASA contract monitor.

ally well on a 100 n.m. orbital mission of an early SA-6 second stage vehicle. Of particular interest is a demonstration of the effectiveness of the numerical methods used which are generally applicable to a wide variety of guidance and control feedback problems.

NASA TN D-3117

November, 1965

MONTE CARLO APPROACH TO TOUCHDOWN DYNAMICS FOR SOFT LUNAR LANDING

By

Robert E. Lavender

ABSTRACT

Results of analytical touchdown dynamics investigations are presented which were conducted to obtain estimates of the probability of stable landing for configurations with various landing gear diameters. Both three-legged and four-legged vehicles are considered in the analysis. Dynamic scaling considerations are taken into account so that the results are applicable to a wide range of vehicle size and mass. A Monte Carlo approach is taken in the determination of initial landing conditions.

Results indicate that, for a given probability of stable landing, a three-legged vehicle requires a landing gear diameter only slightly larger than the diameter required for a four-legged vehicle. Therefore, the three-legged vehicle's landing gear should weigh less.

B. PRESENTATIONS

AN ANALYTICAL REDUCTION OF THE OPTIMAL TRAJECTORY PROBLEM

By

Rowland E. Burns

ABSTRACT

The problem of optimal thrust programming of a single stage rocket powered vehicle to achieve maximum payoff at specified end conditions is treated. The vehicle is assumed to operate in vacuo in an inverse square gravitational field. For the case of the so-called singular arc, the Lagrange multipliers are determined, and the mass flow rate to maintain a singular arc condition is derived.

M. S. Thesis, Mathematics, August 1965
University of Alabama

STUDIES OF SATURN BOOSTER RECOVERY

By

Jesco von Puttkamer

Aero-Astrodynamics Laboratory
NASA-George C. Marshall Space Flight Center
Huntsville, Alabama

ABSTRACT

The paper deals with the discussion of booster recovery studies, as performed at MSFC, and their results.

First, the rationale of booster recovery studies, the historic background of the subject, and the basic principles of booster recovery are presented in a cursory manner. Then, the most recent thinking in the area of booster recovery is illustrated by summarizing the results of recent studies of SATURN-V first stage (S-IC) recovery at Marshall. The requirements and design criteria of suitable recovery systems are outlined by treating the subject step by step according to actual events encountered during the recovery sequence.

By necessity, many of the points discussed are engineering considerations, directly related to "routine" booster stage hardware.

Presented at the University of Minnesota's course "Final Phase, AERODYNAMIC DECELERATION," University of Minnesota, July 6-16, 1965, Minneapolis, Minnesota.

ON TOUCHDOWN DYNAMICS ANALYSIS FOR LUNAR LANDING

By

Robert E. Lavender
Scientific Assistant to Director
Aero-Astrodynamics Laboratory

George C. Marshall Space Flight Center
Huntsville, Alabama

ABSTRACT

Analytical methods which may be used for obtaining touchdown dynamics results vary from a simple rigid body-impulsive force procedure which accounts for only a few parameters to elaborate three-dimensional numerical procedures which attempt to account for practically all of the parameters affecting the motion. Landing stability boundaries obtained from six methods are compared to each other as well as with results from experimental drop tests. The results show considerable variation between the various methods. A review of each method (parameters are considered in each) and comparison of the analytical results lead to the conclusion that the most detailed procedure considered gives results which most closely correspond to the results which would be obtained by a full scale vehicle landing on the moon. This conclusion is reached even though another method gives the best correlation with scale model experimental drop tests. It is further concluded that dynamically scaled models must be constructed with great care in order to obtain the proper representation of the full scale vehicle. Results are given for both two-dimensional symmetric landings as well as three-dimensional landings.

AIAA Symposium on Structural Dynamics and Aeroelasticity
MIT, Cambridge, Massachusetts
August 30-September 1, 1965

LIQUID-FREE SURFACE INSTABILITY RESULTING FROM RANDOM VERTICAL ACCELERATION

By

L. L. Fontenot
General Dynamics/Convair
Huntsville, Alabama

G. F. McDonough
Aero-Astrodynamics Laboratory, MSFC

D. O. Lomen
General Dynamics/Convair
San Diego, California

ABSTRACT

In this paper the stability of the plane-free surface of a heavy liquid enclosed in a vertical cylinder undergoing random vertical accelerations is investigated. The cylinder studied has an arbitrary cross section and a flat bottom and stability is investigated in a mean square sense. The liquid is assumed frictionless, homogeneous and incompressible, and viscous and capillary forces between liquid and container are considered negligible. Fundamental hydrodynamic equations are used as the basis of the mathematical description of the fluid behavior.

Random inputs in the form of white noise are applied and the correlation functions between principal modes of oscillation are determined (considering the ensemble average) and, from the solution of the resulting integral equations stability of the surface is established by use of the Routh-Hurwitz criterion. This shows that the system is always unstable for white noise inputs if damping is not present or is sufficiently small.

Presented at the Sixth International Symposium on Space Technology and Science, Tokyo, November 29-December 4, 1965.

DYNAMIC STABILITY OF THIN ELASTIC PLATES UNDER THE ACTION OF NON-DETERMINISTIC LOADS

By

D. O. Lomen
General Dynamics/Convair
San Diego, California

L. L. Fontenot
General Dynamics/Convair
Huntsville, Alabama

G. F. McDonough
Aero-Astrodynamics Lab, MSFC
Huntsville, Alabama

ABSTRACT

This paper treats the problem of a simply supported rectangular plate under the action of random compressive forces applied at the edges. The theory of linear stochastic systems is applied to the problem for an input of pure white noise. This theory predicts the occurrence of lateral instability of the plate in a mean square sense for any amount of white noise in the case of very low damping.

Preliminary numerical results have been obtained by analog simulation for the case of zero damping (other than that inherent in the elements of the computer). A first attempt at correlating the average time rate of change of amplitude with a frequency parameter, there appears to be a definite straight-line trend in the data plot (log-log scale) although considerable scatter exists in the data.

Presented at the Sixth International Symposium on Space Technology and Science, Tokyo, November 29-December 4, 1961.

STABILITY PROBLEMS IN THE CONTROL OF SATURN LAUNCH VEHICLES

By

G. F. McDonough
Aero-Astrodynamics Laboratory
Marshall Space Flight Center
Huntsville, Alabama

ABSTRACT

The control system for attitude control of a launch vehicle during powered flight is designed to insure that the engine thrust vector is so oriented that attitude commands do not result in vehicle rotation instabilities. Stability problems arise because the vehicle is elastic rather than rigid, contains propellants which are free to oscillate, and is at most times aerodynamically unstable.

Elastic body bending modes arise from engine gimbal forces and aerodynamic forces. Control sensors must differentiate such modes from rigid body modes to prevent the occurrence of closed-loop oscillations. Methods of stabilization include phase stabilization (achieved by sensor location, shaping control networks, adaptive control techniques, or sensor signal blending), gain stabilization (by attenuation), or by change in configuration to eliminate instability of aerodynamic forces.

Propellant oscillations can couple through the control system to produce closed-loop oscillations. This instability can be reduced or eliminated through choice of tank location, shaping of control system networks, or by mechanical means such as baffles.

Engine compliance modes can couple with the vehicle modes; these can be eliminated through actuator and thrust structure design.

Control mode effects can be eliminated by proper choice of control frequency or by providing high damping in the control mode.

The difficulty in handling these problems for the Saturn V vehicle lies in the close grouping of frequencies for the various modes; stabilization of one mode by present techniques generally worsens the effect of one or more other modes. For this reason, solutions of vehicle stability problems are compromises.

Several criteria are available for examining vehicle stability; however, these require linear equations with constant coefficients. To provide these coefficients time-slice investigations are used. Vehicle characteristics must be determined; this requires extensive testing as well as theoretical analysis and analog investigations. Where unknowns cannot be eliminated, latitude must be provided in the control system design.

Presented at the "Internation Conference on Dynamic Stability of Structures" at Northwestern University, October 1965. Sponsored by Northwestern University and the Air Force Office of Scientific Research.

DYNAMIC TESTING OF SATURN LAUNCH VEHICLES

By

George F. McDonough

ABSTRACT

Dynamic testing of full-scale launch vehicles is an important part of the Saturn program at Marshall Space Flight Center. Results of these tests are used to verify existing dynamic analyses as well as to provide a basis for the development of new theories where these are needed. In addition, necessary information is obtained from these tests which either cannot be obtained elsewhere or, if there are other sources, these entail additional expense or time to achieve the same result.

The Saturn V vehicle will serve as a suitable example of the application of dynamic testing. When this vehicle was first conceived, there was no existing knowledge of the dynamic behavior of clustered vehicles. Dynamic tests of scale models were conducted and theories of the behavior were developed; however, neither of these approaches was to prove

adequate in defining the required vehicle characteristics either for structural design or for control system design to insure stability during flight. Primarily through the application of the results of carefully controlled full-scale dynamic testing at MSFC, together with necessarily limited flight test results on Saturn I, the dynamic characteristics of clustered vehicles are reasonably well understood today. As a consequence, the amount of dynamic testing that has been performed on the second-generation Saturn IB is extremely limited. There remain certain vehicle characteristics which cannot as yet be determined theoretically with sufficient accuracy; chief among these are structural damping and local damping effects, which are particularly important in the definition of sensor response for the flight control system. In addition, much of the necessary knowledge on the complex elastic connections of the clustered vehicles must be obtained through testing, and can best be gained through dynamic testing.

In the Saturn V program, once again we are faced with extremely important unknowns. As in the past, the ground rules under which we operate emphasize that we do not have the luxury of development flights; in short, there can be no flight failures if the program is to meet its schedules. The only means by which we can reasonably insure the required reliability is through a well conceived and carefully executed ground test program which includes dynamic testing of a flight configuration vehicle. Among the more urgent problems for the Saturn V vehicle are the longitudinal vibration problem and local effects, which become even more important as the vehicle becomes more flexible and as nonlinear behavior exerts a greater influence. Also, damping and three-dimensional effects are increasingly important. A well-balanced program of theoretical effort to define these effects is underway at MSFC, as well as throughout NASA and the aerospace industry; however, these efforts will not provide the critical information without verification by dynamic testing. Furthermore, the state-of-the-art of dynamic testing has had to be improved before the required results could be obtained. Several improvements have been made, a few examples of which are (1) an improved support system to eliminate damping in the support system to allow better measurement of structural damping, (2) use of scale model tests to aid in full-scale test planning and to enable earlier checks of theory to be made, and (3) improved instrumentation systems and data handling systems to allow a maximum amount of accurate data to be obtained in the shortest possible time to offset severely restricted test schedules.

Presented at the Sixth International Symposium on Space Technology and Science, Tokyo, November 29-December 4, 1965.